An Experimental Investigation of Liquid Droplets Impinging Vertically on a Deep Liquid Pool

He Zhao

NTNU

Trondheim, October 2009

Abstract

Interactions between droplets and liquid films are found widely in our daily life, and many interesting phenomena can be observed. Scientists study the phenomena not only because they are fascinating but also apply the knowledge to many fields such as industry, biology, oceanography, astronomy etc.

The knowledge can be used to improve the efficiency and to develop design tools for heat exchangers in the industrial LNG processes. The experimental investigation of micro-scale level droplet-film interactions is critical in order to improve the understanding in this field. The main focus of the study is to experimentally investigate the vertical impact between droplets and a deep liquid film of the same fluid. The investigation aims at improving the understanding of different phenomena in the drop-pool impacts.

A literature review showed that there was insufficient information on micron-level droplets (diameter below 1 mm) impacting with a deep pool, and thus the present work aimed at giving this part of information. An experimental setup was designed and constructed in order to carry out the experiments in a controllable manner. The setup had a special function which reduced the impinging frequency of a droplet stream, and thus the impact can be studied with a reasonable isolation from the impacts of the neighboring droplets. Besides, other components designed and used in the experiment, such as the droplet generator, light sources, safety issues etc., are described in detail in the this work. The experimental setup enables the generation of droplets with the diameter range approximately 0.1 mm–0.7 mm and the velocity range approximately 0.1 m/s–10 m/s. The uncertainty analysis showed that the relative uncertainty for diameter and velocity measurements are generally below 5%, and the relative uncertainties for the dimensionless numbers (Re, Oh, We, Fr and Ca) are generally below 10%.

Four different phenomena, coalescence, bouncing, partial coalescence and jetting were generated and observed by using different fluids including distilled water, technical ethanol, n-pentane, methanol and 1-propanol. Ob-

servations of different phenomena are presented and described thoroughly. Results are presented with the uncertainties which are evaluated specifically for this work.

Data analysis was carried out to characterize the thresholds between different phenomena, two regression methods, the least squares and the least points, were used to find the curve-fitted threshold models. The thresholds between coalescence and jetting for five fluids are characterized using an exponential model using We and Oh and a linear model using Fr and Ca, and both models give very good characterizations with few uncertain points within the diameter and velocity ranges in the present study. The literature jetting-threshold data (Rodriguez & Mesler 1985) with much larger diameter (up to 3 mm) and lower velocity (≈ 1 m/s) was compared with the models, and the comparison showed that the exponential model applies better in the millimetric range than the linear model. For predicting the thresholds for fluids other than the five experimental fluids, calculation methods for the parameters in both models are suggested.

Two thresholds between coalescence and bouncing are characterized by using the critical Weber number, at which a phenomenon transits to the other. The thresholds of bouncing-coalescence are characterized for distilled water, technical ethanol and 1-propanol, and the thresholds of coalescence-bouncing were characterized for distilled water and technical ethanol. For assessing the energy loss during bouncing, the restitution coefficient was analyzed, and the stable levels of the restitution coefficients were between 0.2-0.3 which agreed well with the literature.

Based on the observations, characterizations of thresholds and analysis of the restitution coefficients, the effects from the physical properties of the fluids were analyzed. The effects of viscosity was found very dominant. Due to the dissipation of the turbulence, viscosity reduces the perturbations for the crown formation and breaking, giving higher critical Weber number for the bouncing-coalescence threshold and higher restitution coefficient. Surface tension inhibits the formation of the crown and giving higher restitution coefficient due to better elasticity.

Acknowledgment

This project has been carried out at the Norwegian University of Science and Technology (NTNU), Department of Energy and Process Engineering. This work forms a part of the Remote Gas project at SINTEF Energy Research, performed under the strategic Norwegian research program Petromaks. The financial support is from the following partners: StatoilHydro, UOP, Bayerngas Norge, Aker Solutions, DNV, and the Research Council of Norway (168223/S30).

First of all, I owe my deepest gratitude to my supervisor Professor Jostein Pettersen for giving me the opportunity to realize this work and for all the instructive guidance. My grateful acknowledgment goes to my co-supervisor Dr. Svend T. Munkejord, for his illuminating advices and unstinted help in the duration of this work.

I am very grateful to Dr. Mario Ditaranto and Dr. Amy Brunsvold for their useful suggestions and discussions on the experimental methods. Furthermore, I wish to express my sincere thanks to Dr. Carlos A. Dorao and Dr. Maria Fernandino for their inputs in both setup construction and data analysis. Many thanks goes to Ms. Gunhild A. Gjøvåg for the administrative support which helped me smoothly initiate the project.

I would like to give my great appreciations to Mr. Håvard Rekstad for helping me in designing the experimental setup, Mr. Erling Mikkelsen and Mr. Martin Bustadmo for the contributions in constructing and modifying the experimental setup as well as the laboratory room. In addition, I would like to thank the laboratory personnel in the Department of Energy and Process Engineering. Your experience and skills made the experiment successful.

Thanks to the students from École Nationale Supérieure de Mécanique et d'Aérotechnique (ENSMA, France): Alexis Sevault for his collaboration on the experiment with water and for the nice drawing he made for the setup and Xavier Chata for his collaboration on the experiment with 1-propanol.

My special thanks goes to my friends for making my life enjoyable in Trondheim. Last but not least, I would like to thank my wife Xiaoju for her patience and understanding.

Contents

List of Figures

List of Tables

Nomenclature

α	slope in the linear model
$\bar{\Omega}$	Averaged degree of discrepancy
$\bar{\Pi}$	Averaged property of a fluid
β	Intercept in the linear model
Ca	Capillary number
ϵ	Restitution coefficient
Fr	Froude number
$\hat{\alpha}$	Exponent in the exponential model
$\hat{\beta}$	Threshold value in the exponential model
$\hat{\gamma}$	reference diameter in the exponential model
μ	Liquid viscosity
μ_g	Gas viscosity
Oh	Ohnesorge number
Ω	Degree of discrepancy
ω_{Ca}	Uncertainty of Capillary number
ω_{Fr}	Uncertainty of Froude number
ω_μ	Uncertainty in viscosity
ω_{Oh}	Uncertainty of Ohnesorge number
ω_{Re}	Uncertainty of Reynolds number
ω_ρ	Uncertainty in density

ω_σ Uncertainty in surface tension

ω_{am} Uncertainty from the camera tilted angle measurement

$\omega_{\text{diam\_seg}}$ Uncertainty from the diameter segmentation

$\omega_{\text{disp\_seg}}$ Uncertainty from the displacement segmentation

ω_{gm} Uncertainty from the measurement of the standard measurement

ω_{g} Uncertainty from the manufacture of the standard measurement (gauge)

ω_{os} Uncertainty from the Droplet oscillation

$\omega_{\text{rand}-\text{n}}$ Random uncertainty from individual source number "n"

$\omega_{\text{sys}-\text{n}}$ Systematic uncertainty from individual source number "n"

ω_{tj} Uncertainty from the threshold judgment

ω_{t} Uncertainty from camera frame rate

ω_{We} Uncertainty of Weber number

ω_D Uncertainty of diameter

ω_V Uncertainty of velocity

Π Property of a fluid

Π_{MR1} Property of the mixed refrigerants for liquefaction

Π_{MR2} Property of the mixed refrigerants for subcooling

Re   Reynolds number

ρ Liquid density

ρ_g Gas density

σ Surface tension

St   Stokes number

We   Weber number

A_α Density exponents for calculating the slope in the linear model

A_β Density exponents for calculating the intercept in the linear model

$A_{\hat{\gamma}}$ Density exponents for calculating the reference diameter in the exponential model

B_{α} Viscosity exponents for calculating the slope in the linear model

B_{β} Viscosity exponents for calculating the intercept in the linear model

$B_{\hat{\gamma}}$ Viscosity exponents for calculating the reference diameter in the exponential model

B_x Systematic standard uncertainty

C_{α} Surface tension exponents for calculating the slope in the linear model

C_{β} Surface tension exponents for calculating the intercept in the linear model

$C_{\hat{\gamma}}$ Surface tension exponents for calculating the reference diameter in the exponential model

C_{BC} The value of the critical Weber number for B-C threshold

C_{CB} The value of the critical Weber number for C-B threshold

D Droplet diameter

D_c^* Dimensionless crown diameter

D_m Diameter measurement

$D_{\text{efficient}}$ Equivalent diameter

D_c Crown diameter

f Scaling factor for camera images

H_f^* Dimensionless film thickness

H_f Film thickness

K General threshold value

K_c Threshold value by Cossali et al. (1997)

K_{hs} Threshold value by Hsiao et al. (1988)

K_h Threshold value by Huang & Zhang (2008)

K_m Threshold value by Mundo et al. (1995)

K_s Threshold value by Stow & Hadfield (1981)

K_v Threshold value by Vander Wal et al. (2006b)

L Displacement of droplet

L_m Measurement of displacement

P_x Random uncertainty

t Time interval between two neighboring images

U Uncertainty model

V Droplet impinging velocity

V' Bouncing velocity

x exponent

Chapter 1

Background and Motivation

1.1 Applications of Droplet Impacts

Droplets and their associated phenomena have been investigated since 1876 when Worthington (1876) studied the "finger pattern" and central jet formation as droplets splashed on a plate. A very common example is the impact of rain drops onto a pond, where many different phenomena can be observed. A raindrop may be spherical in the air, and after impinging with the pond, a highly symmetric "crown" followed by a central jet may form, or the droplet may simply merge into the pond with ripples expanding on the liquid surface. Under certain conditions, floating and bouncing of the droplet can occur on the water surface.

An understanding of drop impacts is needed due to the applications in various fields. In gas-liquid separation equipment, the overall flows consists of numberless micro-scale level interactions such as droplet-droplet and droplet-film, and the large number of the complex phenomena can change the behaviors of the equipment to make the efficiencies deviate from the ideal conditions. The design of gas-liquid separation units can benefit from the understanding of the droplet impacts (e.g. Austrheim 2006, Johnsen 2007, Dorao et al. 2009). For scrubbers, the design must enhance the coalescence of droplets, and for a better capturing ability, the droplets impacting on the mesh geometries should preferably deposit or coalesce into the liquid film instead of splashing or bouncing. In heat exchangers, the most efficient heat transfer happens where the refrigerant and walls are in contact, while the detachment of droplets from the bulk liquid reduces the performances of the heat exchangers as the detached droplets are suspended in the vapor phase and contribute little to the heat transfer. However, coalescence and deposition of the droplets will increase the heat transfer. The understanding of the phenomena can assist in designing the equipment in which more reasonable geometries can give favorable flows for the process and thus enhance the operating efficiency.

Spray cooling requires the droplets to deposit and spread on the surface of the target to reach a better heat transfer. The spray forming and coating process requires high accuracy of the droplet impacts in order to produce a homogeneous layer for promoting the cooling efficiency (e.g. Aziz & Chandra 2000, Pasandideh-Fard et al. 2001) and the uniform coverage. Due to the involvement of phase-change, these processes may be more complicated than a pure physical interaction process.

1.2 Motivation

A key motivation for the present work has been to increase the understanding and modeling capabilities for shell side refrigerant flow in spiral wound heat exchangers (SWHE) used for liquefaction of natural gas. This type of heat exchanger is commonly used in all base-load LNG processes (Hetland & Gochitashvili 2004), and a good fundamental understanding of fluid flow and heat transfer is essential for design and operation of LNG plants (Lex et al. 2007).

The SWHE is a vertical "tower" where the tube bundle is spun layer by layer in a spiral pattern onto a mandrel, Figure 1.1(a). The fluid(s) to be cooled or liquefied flow inside the tubes from bottom to top, while the refrigerant flows downwards on the shell side while it vaporizes and absorbs heat. Flow distribution and heat transfer on the shell side is decisive for the performance of the unit. Flow conditions on the shell side are complex, with gravity-dominated flow near the top of the exchanger, and shear-controlled flow near the bottom due to increasing vapor velocity. The liquid-phase
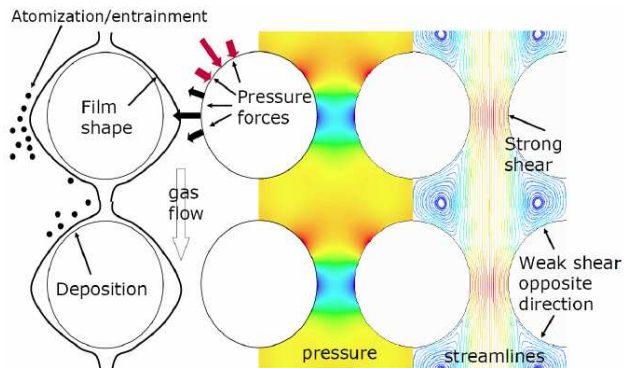
(a) SWHE (Linde).   (b) Phenomena in SWHE on shell side (StatoilHydro).

Figure 1.1: Spiral wound heat exchanger and the micro-level phenomena on shell side.

refrigerant flows across the tubes and as a film along the inclined tubes while it vaporizes. In order to model the shell side flow and heat transfer, entrainment and deposition mechanisms need to be accounted for, since the quantity of liquid droplets entrained in the vapor phase influences the local heat transfer and the liquid flow distribution (Yung et al. 1980). Detailed modeling of local phenomena inside the exchanger thus relies on knowledge of the interaction mechanisms between liquid film and droplets, including prediction capabilities for regimes of coalescence/deposition, bouncing and splashing mechanisms. These types of mechanisms are the focus of the present work, which contains extensive experimental data using several fluids to improve the validity of models over a range of fluid properties. Figure 1.1(b) illustrates local phenomena on the shell side, with vapour and entrained droplets flowing across a tube bank with liquid film.

Other than heat exchangers, the phenomena of droplet impacts are of common interests to scrubber design, spray cooling etc.

1.3 Focus of the Work

The targets, on which droplets impinge, can be different such as dry surface, film covered surface or droplets, and the impinging angles can be varied. This investigation concerns the vertical impacts of micron-level droplets (diameter below 1 mm) onto a deep liquid pool of the same fluid due to insufficient understanding in this area. The deep liquid pool was defined as one with a depth much larger than 10 times the droplet diameter (Vander Wal et al. 2006a). In this study, the depth of the pool is maintained at 45 mm, and the droplet diameter ranges from around 0.1 mm to 0.7 mm. The velocity range is from 0.1 m/s up to around 10 m/s, and under these conditions the impact process is not affected by the bottom of the pool. The investigation focuses on three distinct phenomena:

- Jetting.

- Coalescence.

- Bouncing.

More specific description of the phenomena can be found in Chapter 2 and Chapter 5.

The research results available in the area of droplet impacts are characterized by the following:

- Experimental fluids in one investigation were not many (less than 3 in many cases), and it thus makes the study of the effects from different fluids difficult.

- There is insufficient information on micron-level droplet impacts, especially for the droplet-pool interactions with a high level of impact energy such as jetting and splashing.

- Droplet isolation is a common problem in the experiment of droplet impacts because the impacts are disturbed by the neighboring or preceding droplets, and the disturbances introduce factors which can change the impact processes and outcomes. Isolating the phenomena is very important for the experiment accuracy, while one exception is that non-isolated impacts can be important for study the spray impacts where surface fluctuations, film velocities and crown-crown interactions needs to be considered.

- The phenomenon of bouncing has only been investigated with a stream of droplets with oblique impinging angles (Rein 1993), and there are not enough studies on vertical-impact bouncing which is more difficult to generate because of the low impact energy.

- There are not many studies on droplets impacting with a deep liquid pool.

In order to provide some of the non-covered information described above, the present work focuses on droplet impacting with a deep liquid pool. The experiments focused on a wide diameter range in micron-level from approximately 0.1 to 0.7 mm and a relatively wide velocity range from approximately 0.1 to 10 m/s. A method for generating a stream of droplets with decreased impact frequencies for obtaining non-disturbed phenomena is presented. The specific objectives and contributions of the investigation are to:

- Design and construct a robust experimental setup to study different impact phenomena which are generated in a highly isolated manner so that there is no or little disturbance from the neighboring impacts, and the facility is also flexible to be modified for other experiments such as droplets impacting on a tilted flowing film with different impinging angles.

- Carry out experiments with the focus on droplets impacting vertically on a deep liquid film with different fluids.

- Generate the phenomena with velocity and diameter ranges as wide as possible.

- Apply suitable routines to process the images to obtain the fundamental parameters such as diameter, impact velocity, angle.

- Analyze the uncertainties for the fundamental parameters and the dimensionless parameters.

- Analyze the thresholds between different phenomena, compare the thresholds with the literature data and investigate the effects of the physical properties.

1.4 Structure of the Thesis

The thesis starts with the theoretical background in Chapter 2, which includes the definitions of the regimes of different phenomena, the dimensionless parameters and a literature review. The empirical models used in the literature for characterizing different regimes is summarized and discussed in this part.

The following section, Chapter 3, focuses on the experimental setup and methodology. The overview of the experimental setup is described at the beginning of this chapter, and the important components are described in detail in the following section. The last section of this chapter is devoted to the investigation of the physical properties of the experimental fluids. The physical properties obtained from a variety of sources are summarized and compared, and the devices and methods used in this work for measuring the properties are described.

The routines for image processing and the methods for uncertainty analysis are described in Chapter 4. The image processing includes the analyzing methods of a software,"ImageJ", and the post-processing procedures for obtaining the critical parameters by using a MATLAB script. There are uncertainties closely related to the experimental methods and the image processing methods, and these uncertainties are discussed and described in the following section of this chapter.

The observations and results (the fundamental parameters: diameter, velocity and impinging angle) from the experiments are described in Chapter 5. The observations are classified according to different regimes, and based on the regimes, the results from different fluids are presented.

The data analysis and discussion of the results can be found in Chapter 6. Based on different judgment rules, two regression methods for finding the most suitable threshold are described in the beginning of this chapter. For characterizing the thresholds between different regimes, the dimensionless parameters or the combinations of them are used. The threshold of coalescence-jetting is characterized with two threshold models using combinations of dimensionless parameters, and comparisons with the literature data is given. Calculation ways are proposed for predicting the

coalescence-jetting threshold for an uncharacterized fluid. Thresholds of coalescence-bouncing and bouncing-coalescence are characterized with the Weber number. Based on the observations and the characterizations for the experimental fluids the effects of physical properties on the phenomena are discussed.

Chapter 7 gives the conclusions of the present work and recommends the further studies.

Chapter 2

Theory and Literature Review on Droplet-Film Impacts

2.1 Introduction

Fundamental information is provided in this chapter as the basis for this thesis. This chapter first provides the definitions of different regimes. Then, some of the most important dimensionless parameters and definitions, which are commonly-used in the literature, are introduced. A summary of the literature on droplets impacting with liquid-covered surface is also given. Finally, descriptions and discussion on different empirical models and characterization methods are given at the end of this chapter.

2.2 Different Regimes

Four main regimes are distinguished in the investigation, and according to the impact energy from low to high, they are:

1. Low-energy collision coalescence.

2. Bouncing.

3. High-energy collision coalescence.

4. Jetting.

2.2.1 Coalescence

Phenomenologically, there should not be considerable differences between the two types of coalescence (low-energy and high-energy). A schematic drawing of the sequential process of coalescence is shown in Figure 2.1. The characteristic steps are shown in Figure 2.1:
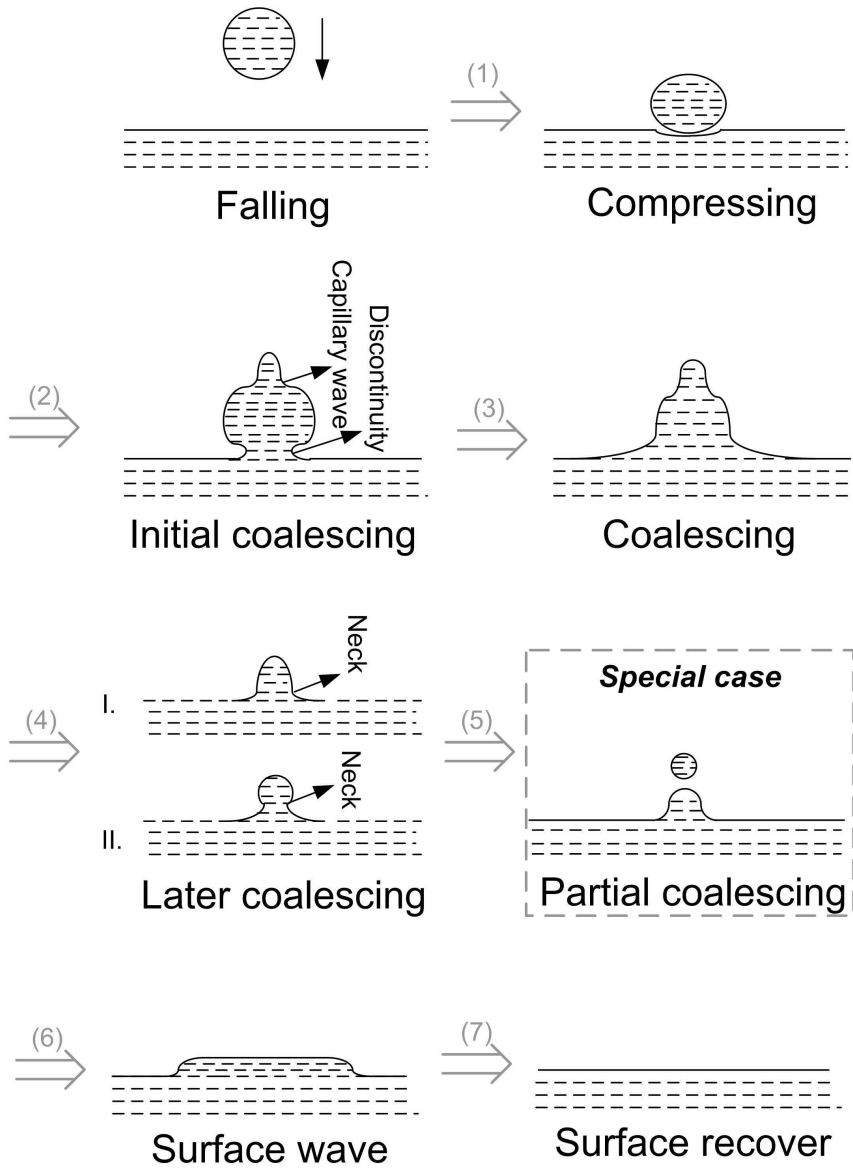
Figure 2.1: Schematic drawing of the sequential process of coalescence.

1. A droplet falls in the surrounding gas, towards a stagnant deep liquid pool.

2. When the droplet is approaching the interface of the pool, the droplet does not coalesce with the bulk due to the existence of a gas film. At this point, both the droplet and the pool surface deform slightly due to flow resistance from the inertia of the gas film. Jayaratne & Mason (1964), Zhbankova & Kolpakov (1990) and Bach et al. (2004) suggested that this intermediate gas film prevents impinging droplets from coalescing into the bulk liquid.

3. As the gas film breaks, the coalescence initiates. Due to the unbalanced surface tension forces (Thoroddsen 2000), a discontinuity forms at the interface where the droplet joins the liquid film. The discontinuity generates a capillary wave which forms a kind of tip on top of the droplet.

4. As the coalescence process goes, the discontinuity reduces.

5. In the later phase of coalescence, during the merging of the tip, a neck forms. The neck can either be non-obvious, such as type I in the figure, or obvious like type II. The type II, sometimes, leads to a special case which is the partial coalescence of the droplet. In partial coalescence, a small droplet forms due to the breaking of the neck, and this small droplet impacts with the liquid surface and is reflected upwards.

6. A surface wave is generated due to the disturbance of the droplet impact, and it expands until the energy is completely dissipated. The wave is very strong and obvious in high-energy collision coalescence, while it is minor in low-energy collision coalescence.

7. The surface recovers to calmness in the end.

2.2.2 Bouncing

As opposed to coalescence and splashing, in bouncing, the impinging droplet does not merge into the bulk liquid after the impact due to the presence of a thin gas film. The droplet is deformed at the gas-liquid interface and bounces off after a short contact time with the liquid film. A schematic drawing of the sequential process of bouncing is shown in Figure 2.2. The initial steps of bouncing are quite similar to those in coalescence. The characteristic steps are:

1. A droplet falls freely in the surrounding gas, and the pool is still.
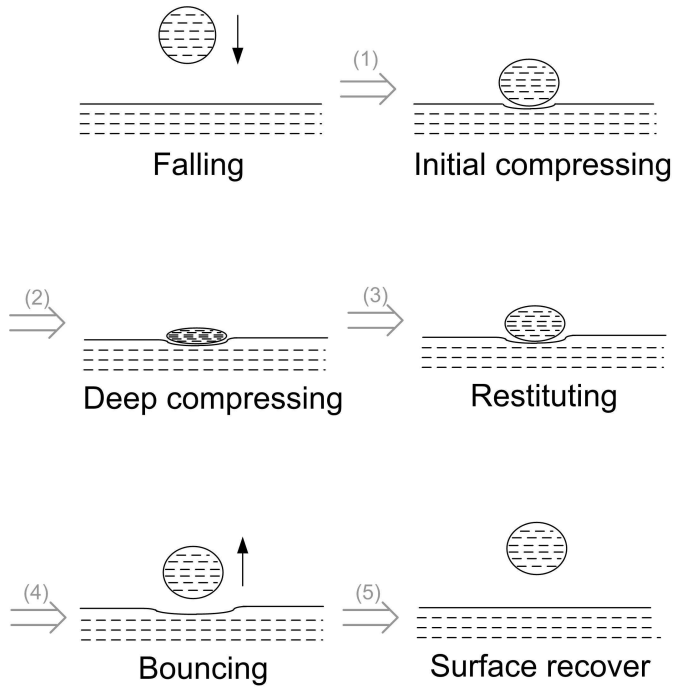
Figure 2.2: Schematic drawing of the sequential process of bouncing.

2. When the droplet approaches the surface of the pool, both the droplet and the surface are deformed slightly due to the flow resistance.

3. The droplet is further deformed into a more flat shape without breaking up the gas film.

4. After reaching the maximum deformation, which is characterized by the maximum ratio between the major axis to the minor axis, the droplet and the surface starts to restitute due to the surface tension. The restitution forces reflect the droplet upwards, and a minor wave starts to expand due to the disturbances from the impact.

5. As the droplet travels further upwards in the gas, the surface recovers to calmness in the end.

2.2.3 Jetting

Jetting occurs when a droplet impingement excites a strong wave at the surface of a pool, and a central jet forms after a while from the impact. The wave sometimes grows to a "crown", the rim of which may break into

splashing droplets. A schematic drawing of the sequential process of jetting is shown in Figure 2.3. The characteristic steps are:

1. A droplet falls freely in the surrounding gas, and the pool is still.

2. Due to the high impact energy, as soon as the droplet impacts on the surface, side splashing occurs due to the large velocity discontinuity on the horizontal direction.

3. A crater and a strong wave are formed due to the impact.

4. A special case is that as the crater and the wave grow, the wave is finally developed into a crown-like shape, and secondary droplets may be generated from the rim of the crown.
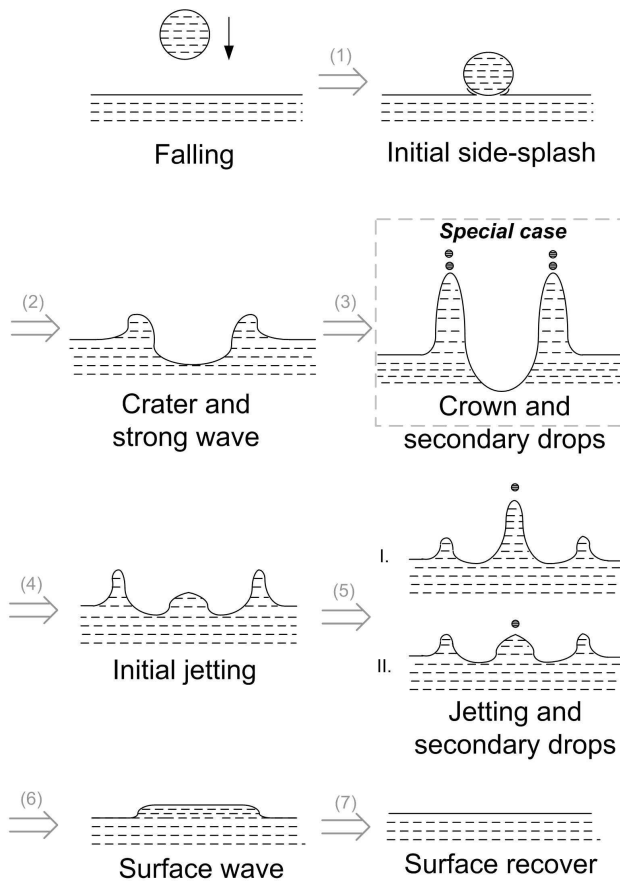
Figure 2.3: Schematic drawing of the sequential process of jetting.

5. As the strong wave sinks downwards to a certain extent, a central jet starts to form at the center of the crater.

6. When the wave retracts further, the obvious central jet is formed, and the appearance of the obvious central jet is set as the criterion for jetting in this investigation. Two types of jets are observed in the experiment. For type I, the primary central jet rises higher than the retracting wave, and it can be seen in the captured images. For type II, the primary central jet is approximately the same height as the strong wave, and sometimes it can barely be seen in the images. However, one or several secondary droplets are observed in the type II jetting, and so the appearance of the secondary droplets are also used for identifying the phenomenon of jetting.

7. With the retraction of the central jet, a wave expands on the surface, and the surface calms down in the end.

2.3 Dimensional Analysis

Droplet impact phenomena are very complex as many different variables and mechanisms are included in the impact processes. Rein (1993) listed many variables and mechanisms that can affect the impact processes, and they can be classified into three categories:

1. Properties of the fluids: Transport properties such as surface tension, viscosity, density etc.

2. Surface conditions: Smooth or rough, yielding or unyielding etc.

3. Kinematic parameters: Impact velocity, impact angle, droplet size, film movement etc.

The numerous variables and mechanisms make the processes difficult to characterize quantitatively by using one or a few of them. In order to reduce the complexity of the problem and to study the phenomena comprehensively by covering all or most of the dominant variables and mechanisms, dimensional analysis can be used. Dimensional analysis is commonly defined as "a process whereby physical equations are recognized into dimensionless variables" (Johnson 1998). According to the Buckingham Π-theorem (Buckingham 1914), an equation expressed by n variables with m fundamental dimensions, can be reduced to an equation expressed by $(n - m)$ dimensionless parameters, which can be considered as a complete set of dimensionless parameters for a phenomenon. Thus, by using the

dimensionless parameters, the degree of freedom in a model is reduced. This method is very important for developing and generalizing models for complex phenomena in fluid dynamics and heat transfer where many variables and mechanisms are involved. Therefore, it can be assumed that the droplet impingement processes are governed by a complete set of dimensionless parameters. Due to the fact that there are different hypotheses on the dominant variables and mechanisms in the droplet impingement processes, either different or incomplete sets of dimensionless parameters (Rein 1993) can be found in the droplet phenomena studies.

For droplets impinging on a deep liquid pool, based on our experimental conditions, a few assumptions can be made to reduce the variables presented in the above categories. The assumptions are:

- Densities, viscosities and surface tensions are the most relevant thermodynamic properties.

- Physical properties of the vapor phase are not dominant factors for high-energy collision phenomena (jetting and high-energy collision coalescence), but maybe influential to low-energy collision cases (bouncing and low-energy collision coalescence).

- The impact surface is a homogeneous flat liquid surface.

- The impact angle is vertical (90° between the impinging trajectory and the liquid surface).

- The pool is big and deep enough, so effects from the walls and bottom of the pool can be neglected.

- The surrounding gas and liquid surfaces are stagnant.

- Every single impact is an isolated phenomenon and is not affected by the neighboring droplets.

Based on these assumptions, the variables governing the impact processes are reduced to ρ, μ, σ which are the density, viscosity and surface tension for the liquid phase, respectively (ρ_g, μ_g for gas phase may be influential to low energy collision case), plus D and V, which are the diameter and the velocity of impinging droplets. Regardless of the gas properties, there are, thus, five variables with three fundamental dimensions which are mass (kg), length (m) and time (s). If 5 dominant variables and 3 fundamental units are assumed, according to the Π-theorem, two dimensionless parameters can form a complete set of the dimensionless parameters.

The relevant dimensionless parameters including these variables are summarized as follows.

1. Reynolds number (relating inertia and viscous force)

$$\mathrm{Re} = \frac{\rho D V}{\mu} \tag{2.1}$$

2. Ohnesorge number (relating viscosity and surface tension)

$$\mathrm{Oh} = \frac{\mu}{\sqrt{\rho \sigma D}} \tag{2.2}$$

3. Weber number (relating inertia and surface tension force)

$$\mathrm{We} = (\,\mathrm{Oh} \cdot \mathrm{Re})^2 = \frac{\rho D V^2}{\sigma} \tag{2.3}$$

4. Bond number (relating gravitational and surface tension force)

$$\mathrm{Bo} = \frac{\rho D^2 g}{\sigma} \tag{2.4}$$

5. Froude number (relating inertial and gravitational force)

$$\mathrm{Fr} = \frac{V}{\sqrt{gD}} \tag{2.5}$$

6. Capillary number (relating viscosity and surface tension)

$$\mathrm{Ca} = \frac{\mu V}{\sigma} \tag{2.6}$$

7. Stokes number (relating viscosity and gravitational force)

$$\mathrm{St} = \frac{\mu V}{\rho g D^2} \tag{2.7}$$

It can be seen that there can be many different combinations for complete sets of dimensionless parameters. For instance, complete sets of dimensionless parameters can be Re and We, We and Oh, Re and Ca etc.

Besides those traditional dimensionless parameters, in the impacts with a shallow liquid film, film-thickness is also considered influential to the impact processes, and the dimensionless film-thickness (H_f^*) (Cossali et al. 1997) is

$$H_f^* = \frac{H_f}{D}, \tag{2.8}$$

where H_f and D are the thickness and diameter of droplet, respectively.

Most of the quantitative characterizations of the regimes use one or a few of the governing dimensionless parameters. Other dimensionless parameters are used to study the evolution of the impact process. For instance the dimensionless diameter of crown (Cossali et al. 1997)

$$D_c^* = \frac{D_c}{D},\tag{2.9}$$

where D_c^* and D_c are dimensionless and dimensional diameter of a crown, respectively.

Another dimensionless number, the restitution coefficient (ϵ) (e.g. Richard & Quere 2000, Bach et al. 2004), is frequently used to study the bouncing process. The restitution coefficient

$$\epsilon = \left| \frac{V'}{V} \right|,\tag{2.10}$$

where V' and V are the bouncing and impinging velocities, respectively, is the absolute value of the comparison between the velocity after and before the impact. As the impact droplet remains the same in the case of bouncing, the restitution coefficient can also indicate the inertial energy after and before the impact, and thus the energy loss during the impact can be studied.

2.4 Summary of the Literature on Droplets Impacting with a Liquid-covered Surface

In general, the impinged targets can be classified into two main categories: liquid-covered or dry surface. The target of this work belongs to the former category.

2.4.1 Experiments on Splashing/Jetting

There are two main research focuses found in the investigations of splashing/jetting. The first is the characterization of the thresholds between different regimes, and the second is the formations and evolutions of the characteristic parts such as the central jet and crown.

Table 2.1 shows a summary of the literature focusing on splashing/jetting. The research focuses, fluids and focused parameters are listed in the table. D and V denote the droplet diameter and impinging velocity, respectively.

As indicated by the "Focus" column, the threshold between splashing/jetting and coalescence has been the most studied subject. Many authors characterized the threshold of splashing/jetting using dimensional parameters,

Table 2.1: Overview of literature on splashing/jetting.

Authors	D (mm)	V (m/s)	Fluid	Focus
Worthington (1876)	> 5		water, mercury, milk	pattern
Hobbs & Osheroff (1967)	2.4-3.8		milk-water	evolution: jet
Engel (1967)	≈ 5	< 2	water-dye	energy
Macklin & Metaxas (1976)	2.6-3.2		water, ethanol, glycerol	energy
Stow & Hadfield (1981)	3.4	4	water	threshold model
Rodriguez & Mesler (1985)	1-5	< 2.4	water	threshold
Hsiao et al. (1988)			mercury	threshold model
Cai (1989)	3-5.2		water-dye	evolution: crater
Shin & McMahon (1990)	1.25-5	< 3.2	water	evolution:jet
Mundo et al. (1995)	0.06-0.15	12-18	water, ethanol	threshold model
Cossali et al. (1997)	3.07, 3.51	< 6.5	water-glycerol	threshold model
Cossali et al. (1999)	3.82	2.38-4.01	water	evolution: crown
Wang & Chen (2000)	4-5	< 4	water-glycerol	threshold
Manzello & Yang (2002)	3.1	0.36-2.2	water, $C_4F_9OCH_3$	threshold
Rioboo et al. (2003)	1.42-3.81	0.65-3.14	water-glycerol etc.	threshold
Vander Wal et al. (2006a)	2	1.34-4.22	heptane etc.	threshold
Vander Wal et al. (2006b)	2	2.17-4.22	heptane etc.	threshold model
Huang & Zhang (2008)	1.8-4	< 5	water and oil	threshold model

while a few presented empirical models using the dimensionless parameters. As the focus of this work is to characterize the transitions between different regimes by using empirical models, the models are described and discussed in detail in Section 2.6.1.

The "Fluid" column shows that water has been the main experimental fluid in many studies. Only a few of the investigations included more than 3 different experimental fluids. The limited variety of the experimental fluids may restrict the threshold characterization to only a narrow range of physical properties.

The D and V columns shows that most of the investigations focused on "large", millimetric-level droplets (above 1 mm) with relatively low velocities (below 4 m/s), while very few focused on micron-scale level droplets (below 1 mm) where strong effects from viscous and capillary forces can be important. Another limitation is that the droplet diameters, in many of the investigations, are fixed at one or two values or with a narrow range of variations, and the effects from the change of droplet diameter can hardly be studied thoroughly. Compared to the millimetric droplets generated by droppers, the micro-level droplets are generated from a nozzle by Plateau-Rayleigh instability (Lord Rayleigh 1878, Lord Rayleigh 1879) where the surface tension acts to part a liquid jet into small droplets. Small droplets are generated at high frequencies and high velocities which are needed for splashing/jetting. The difficulties in carrying out experiments with micron-

level droplets by the instability method are:

1. Difficulties due to the control issues: it is hard to isolate one impact process from the neighboring impacts, and it is more difficult to focus on the micron-level droplets than on the millimetric-level droplets.

2. Difficulties due to the hardware conditions: the impact process is very fast due to the small droplet diameter and the high velocity so that the requirements for the high-speed camera are high. The high-speed camera must be fast enough to capture the process, and this depends on the resolution and the frame rate of the camera. Due to the fast evolving process, sharp pictures must be obtained using very short exposure times which can be reached through two ways: A continuous light source with the default camera shutter time or a high-frequency pulsing light source. In the latter case, the pulsing time decides the exposure time.

It can be seen from the review of previous work that more information on the splashing/jetting of micro-level droplets is needed. Specifically,

- The droplet diameter range should be as wide as possible.

- Small droplets with high velocities must be generated with a lower impact frequency so that the impact is not affected by the neighboring impacts.

- More fluids with various physical properties need to be used.

- New models may be needed for generalizing the more complete information.

2.4.2 Experiments on Bouncing and Coalescence

Table 2.2 summarizes the focuses, fluids and parameters of experiments in the literature focusing on bouncing and coalescence with low impact energy. D and A denote the diameter and impinging angle, respectively. The velocity information is not included in the table as the velocity level for bouncing and its transitions is very low, normally around or below $1\,\mathrm{m/s}$.

Most of the investigations focused on the threshold characterizations. Only one investigation gave a model for the threshold, and this is perhaps due to the fact that the impact energy level is quite low and the transitions are sensitive to the changes of the parameters. Thus, the thresholds can be well characterized using simple dimensionless parameters. The characterization methods are described and discussed in detail in Section 2.6.2.

Table 2.2: Overview of literature on bouncing and coalescence.

Authors	D (mm)	A (°)	Fluids	Focus
Schotland (1960)	0.2-0.8	5-50	water, methanol, benzene	threshold
Jayaratne & Mason (1964)	0.15-0.19	30-70	water	threshold
Zhbankova & Kolpakov (1990)	0.075-0.15	16-85	water	threshold
Bach et al. (2004)	0.02, 0.04	oblique	water	threshold
Pan & Law (2007)	0.25-0.65	vertical	tetradecane, dodecane	threshold
Huang & Zhang (2008)	1.8-4	vertical	water and oil	threshold model

The droplet diameters in most of the bouncing cases were small, as larger droplets tend to coalescence or splash/jet.

Both vertical and oblique impacts can be found in the literature. Bouncing tends to occur more easily with a stream of non-vertical impinging droplets (Rein 1993). Many investigations with oblique impacts used the normal component to characterize the transitions, and the information on vertical impacts is not abundant. Besides, disturbances from the preceding droplet can be expected for the case of a stream of droplets. Zhbankova & Kolpakov (1990) suggested that the disturbances from the preceding droplet can be neglected for the impact frequency between 40 and 60 Hz. However, when using the Plateau-Rayleigh instability, it will often not reach such a low level of impinging frequency.

Water has been the main experimental fluid. In most of the cases, only one or two fluids were used.

There are much less investigations on bouncing than on jetting/splashing. More work is needed on the investigation of this low energy impact case:

- More fluids need to be examined to find a more general rule which governs the regime transitions in low energy level.

- Investigations focusing on the vertical impact are needed.

- The droplet impact needs to be isolated.

2.5 Mechanisms for Different Phenomena

In the mechanism investigation, only the phenomena of droplets impacting on a liquid-covered surface are considered due to its relevance for the present work.

2.5.1 Mechanisms for Coalescence

Schotland (1960) observed that bouncing transited to coalescence as the impact energy increased, while Jayaratne & Mason (1964) found that coalescence transited to bouncing as the impact energy increased. These seemingly contradictory findings imply that as the impact energy increases from low to high two regimes of coalescence can be found, and the bouncing is between the two coalescence regimes.

Jayaratne & Mason (1964) and Zhbankova & Kolpakov (1990) suggested that a intermediate gas layer resisted the coalescence of droplets into a liquid layer, and the elimination or breaking down of the intermediate layer led to the coalescence. According to Zhbankova & Kolpakov (1990), two different mechanisms accounted for the two coalescence regimes:

- For the low-energy collision coalescence, the intermediate gas layer was gradually expelled by the molecular force, also known as the Van der Waals force, as a certain distance between the droplet and the liquid film had been attained. It required a certain amount of time for the impinging droplet contacting the liquid layer. The dominant driving force in this case was thus the molecular attraction.

- For the high-energy collision coalescence, the intermediate gas layer was suddenly broken or penetrated by the high inertial energy due to the high impinging velocity or large droplet diameter. The dominant driving force in this case was thus the inertia.

The surface wave in the low-energy collision coalescence is much weaker than that in the high-energy collision.

2.5.2 Mechanisms for Bouncing

Bouncing exists with a relatively moderate (between of the high- and low-energy coalescence regimes) Weber number (Bach et al. 2004) which coincides with the conclusion that bouncing is in the middle of the two coalescence regimes. The main factor for the non-coalescence phenomena is the presence of the intermediate gas layer which prevents the droplets from coalescing with the liquid layer. The moderate impact energy is propitious to bouncing because:

- In contrast to the high-energy collision coalescence, the droplets do not have enough inertial force to penetrate the intermediate gas film.

- In contrast to the low-energy collision coalescence, the impact energy of the droplets makes it possible to reserve enough energy during the

deformation for traveling upwards. Two assumptions are made in the present work for the comparison with the low-energy collision case:

1. The working distance for the molecular force is not reached due to insufficient contact time between the droplets and the liquid layer.
2. The working distance for the molecular force is reached but overwhelmed by the restituting force which droplet gained from the droplets and film deformations.

2.5.3 Mechanisms for Splashing/Jetting

Compared to coalescence and bouncing, splashing and jetting relate to high-energy impacts. A central jet is formed and observed in both splashing and jetting. The difference is that most of the investigations (e.g. Cossali et al. 1997, Vander Wal et al. 2006a) used the breaking of the crown as the criterion to characterize splashing, while in this investigation, the formation of a central jet was used as the criterion to characterize jetting, without requiring the breaking of the crown. However, the mechanisms for the two phenomena are similar.

Splashing on a shallow liquid film is different from that on a deep pool because the splashing characteristics are strongly dependent on the depth of the liquid layer. For the interaction with a thin liquid film, the interactions of the cavity subsurface with the solid substrate affect the impact processes (Macklin & Metaxas 1976). This investigation has no effects from the substrate due to the high depth of the liquid pool.

The liquid layer effects were suggested by Vander Wal et al. (2006a). According to their proposed mechanism, a thin film offers a more favorable condition for splashing than a dry surface or a deep pool does as the stationary thin film interfering with the advancing fluid front forms larger "kinematic gradient". In this investigation, a deep pool has stronger absorbing effects comparing with a dry or thin film-covered surface. The reason is that a deep liquid layer absorbs the impinging droplet rather than pushing the liquid outwards in radial direction (Vander Wal et al. 2006a). This can explain the observation in this work that the crown is formed but hardly breaks.

2.5.4 Dry Surface Impacts: Similarity and Difference

Compared to the impact on a liquid-covered surface, the impact on a dry surface have a lot in common. Splashing found in both impacts consists of crown formation, central jet and breaking of the crown into secondary droplets. Bouncing is phenomenologically the same. Coalescence cannot

occur in the dry surface impact due to the absence of the liquid layer, while the attachment of impact droplets to the dry surface is defined as deposition (Mundo et al. 1995).

2.6 Empirical Models for Threshold Characterizations

The threshold characterization can be considered as the process of finding a mathematically-expressed boundary, the empirical model, separating two different regimes. An example is illustrated by Figure 2.4, in which the Weber number and the Ohnesorge number from coalescence and jetting are plotted, and the threshold characterization aims at finding a curve-fitted model, for instance, $K = \text{We} \cdot \text{Oh}^x$ where K and x are constants, to express the threshold curve.

The thresholds between different regimes have been investigated for many years. Empirical models using dimensionless parameters have been suggested based on curve-fitting methods. Even though the experimental conditions and focuses in the literature can be different from those in this work, the approaches to organize the experimental data are very useful references for the model establishment.

In this section, the empirical models and characterization methods in the literature are described. The first section focuses on the empirical models
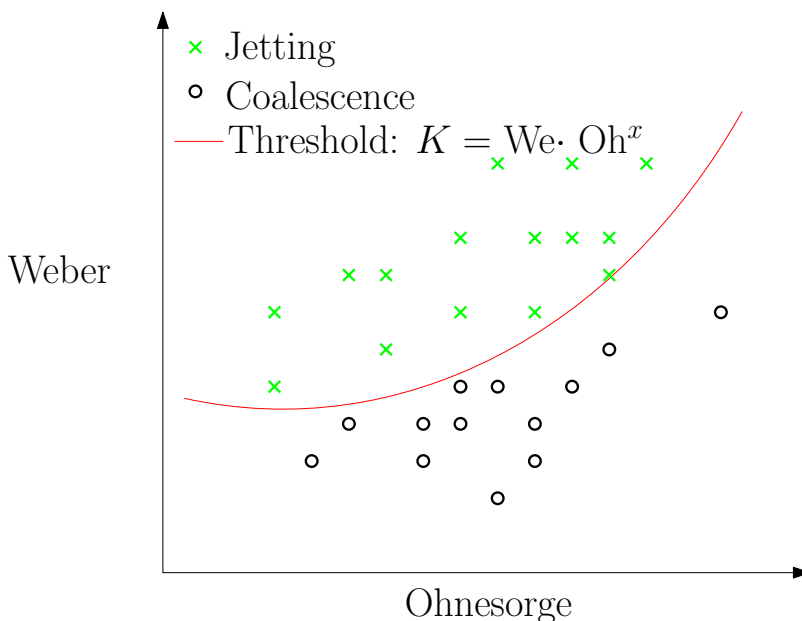
Figure 2.4: An example of threshold characterization.

for characterizing the splashing/jetting, i.e. transitions between coalescence (or deposition) and splashing/jetting. The second section focuses on the characterization of bouncing, i.e. transitions between bouncing and two types of coalescence. The investigations on bouncing are less than on splashing/jetting, and the characterization methods for bouncing are less variant than the methods for splashing/jetting.

2.6.1 Empirical Models for Characterizing Splashing/Jetting

Compared to the empirical model shown in Figure 2.4, the symbols for the constant K in the literature models can be different. In the following part, the symbols are unified by using K with subscripts denoting the names of the authors.

Stow & Hadfield (1981)

Stow & Hadfield (1981) suggested a correlation,

$$K_s = \text{Re} \cdot \text{We}^2, \tag{2.11}$$

which can characterize the splashing on a dry surface. It is suggested that the correlation can be applied to the fluids other than water, and the K_s in the equation is a function of the surface roughness. The restrictions of this model are:

- The droplet diameter was maintained at $1.70\,\text{mm}$, which is invariant and relatively large.

- The experimental fluid was invariant (water).

Hsiao et al. (1988)

Hsiao et al. (1988) studied the transition from coalescence to jetting for droplets impacting on a deep liquid pool. Experimental data of water and mercury was used in the characterization, and the model was simply based on the square rooted Weber number. The critical square rooted Weber number was found to be around 8.

$$K_{hs} = \sqrt{\text{We}} \tag{2.12}$$

The restrictions of this model are:

- The investigated data range was narrow. Droplets with almost fixed diameter and velocity ($\text{Fr} \approx 7$).

- The difference between the square-rooted Weber numbers is much smaller than the difference of their non-square-rooted values, for instance, the difference between $We_1 = 100$ and $We_2 = 81$ is 19, while the difference between $\sqrt{We_1} = 10$ and $\sqrt{We_2} = 9$ is 1. Using constant square-rooted Weber number to characterize the threshold can be questionable as the threshold variation becomes less sensitive to the change of other parameters such as the Froude number, Ohnesorge number etc., and it may lead to a false impression that the threshold is nearly invariant even though the other parameters vary.

Mundo et al. (1995)

Mundo et al. (1995) suggested a correlation,

$$K_m = \text{Oh} \cdot \text{Re}^{1.25}, \tag{2.13}$$

for the splashing on a dry surface. Mono-dispersed droplets were used in the experiment. The experimental fluids were water, ethanol and a mixture of water-sucrose-ethanol aiming at different physical properties. The droplet diameter was between 60 and $150\,\mu m$, and the impinging angle was between 4 and 65°. Due to the oblique impact, the correlation Eq. (2.13) used the normal component. K_m was found to be constant, 57.7, above which splashing happened. The restrictions of this model are:

- the model was for the threshold of splashing on a dry surface, and it might not be suitable for characterizing the threshold of jetting.

- the range of the droplet diameter was relatively narrow (60-150 μm);

- the impingement was oblique while the model used the normal component. Thus, there was no straight validation of the model by the vertical impingements.

- the droplet impinging velocity was kept at a relatively high level (12-18 m/s, vector velocity) which indicated that the impinging frequency was high and the impingements could not be isolated from the neighboring droplets. This could also be seen from the pictures in the article (Mundo et al. 1995) that the distance between neighboring droplets was very close (approximately 2 times the droplet diameter) that the impact of a droplet was definitely affected by the preceding and following droplets. Similar high-frequency impact could also be found in Yarin & Weiss (1995).

Cossali et al. (1997)

Cossali et al. (1997) suggested a model,

$$K_c = \text{We} \cdot \text{Oh}^{-0.4}, \tag{2.14}$$

for droplets impacting on a liquid film covered surface. Millimetric droplets were generated using water-glycerol mixtures. The effect from the film-thickness to the threshold level K_c was investigated. The film-thickness was interpreted using the dimensionless film-thickness, H_f^*, Eq. (2.8). K_c was found to be dependent on the film thickness, and the expression for K_c is written as

$$K_c = 2100 + 5880(H_f^*)^{1.44}, \tag{2.15}$$

above which splashing occurs. This model and its variants have been widely applied in many other investigations (e.g. Rioboo et al. 2003, Sivakumar & Tropea 2002).

The restrictions of this model are:

- the model was developed for the threshold of splashing on a film-covered surface, and it may not be suitable for characterizing the threshold of jetting on a deep pool. Thus, the impinged targets and the phenomena are different.

- droplets are in the millimetric level ($> 1\,\text{mm}$).

Vander Wal et al. (2006b)

Vander Wal et al. (2006b) characterized the transitions to splashing for both impacts on a dry surface and a thin-film covered surface by using many different fluids. The investigation focused on one droplet diameter ($2\,\text{mm}$) and four different impinging velocities ($2.17\,\text{m/s}$, $3.15\,\text{m/s}$, $3.80\,\text{m/s}$ and $4.22\,\text{m/s}$). The empirical models are

$$\begin{aligned} K_v &= \text{Oh} \cdot \text{Re}^{0.609} \, \text{Dry surface} \\ K_v &= \text{Oh} \cdot \text{Re}^{1.17} \, \text{Thin film}, \end{aligned} \tag{2.16}$$

and the values of K_v for dry surface and liquid film are 0.85 and 63, respectively.

Vander Wal et al. (2006b) suggested that the models can be simplified into $K_v = \sqrt{\text{Ca}}$ and $K_v = \sqrt{\text{We}}$ for the impacts on both a dry surface and a thin film, respectively. The values for K_v are constants, 0.35 and 20, for the impacts on a dry surface and a thin film, respectively.

The restrictions of the model are:

- the model is for the threshold of splashing, and it may not be suitable for characterizing the threshold of jetting;

- even though many fluids are used, the data of the velocity and the droplet diameter is limited due to the fact that the droplet diameter is invariant (2 mm) and the investigated velocities are very few (4 different velocities);

- the droplet diameter is above 1 mm with relatively low velocity.

Huang & Zhang (2008)

Huang & Zhang (2008) investigated droplets impacting on both a deep pool and a thin-film using two different fluids, water and oil. Transitions between different regimes including bouncing, coalescence, jetting and splashing were studied. The droplet diameter range was mainly 1.8-4 mm. The model for the transitions of coalescence-splashing and coalescence-jetting on the deep pool is

$$K_h = \mathrm{We}^{0.375} \cdot \mathrm{Re}^{0.25}, \tag{2.17}$$

where the constant K_h is, 70 and 28 for coalescence-splashing and coalescence-jetting, respectively.

The restrictions of this model are:

- only two fluids were used, and it may limit the validation of the model to other fluids;

- the droplet diameter is in the millimetric level above 1 mm.

Conclusions on Splashing/Jetting Characterization

Based on the restrictions and comparisons between different models, the following conclusions are made:

1. There are only two models (Hsiao et al. 1988, Huang & Zhang 2008), which were specifically characterized for the threshold of jetting on a deep pool, while the other models are for the threshold of splashing on either a dry or film covered surface, both of which are phenomenologically different from jetting.

2. One common restriction for the models is that due to the insufficient information, either too few data points, or narrow ranges of velocity and droplet diameter, the validations of the threshold models in wider diameter and velocity ranges are limited.

3. Many models are based on experiments using "large" droplets (above 1 mm), and there are not enough validations from the micro-level droplets (below 1 mm). Small droplets may behave very differently due to stronger viscous and capillary effects as the inertial and gravitational effects become smaller.

4. The models for the impacts with a deep liquid pool are not abundant.

5. Comparing between the models from Mundo et al. (1995), Cossali et al. (1997) and Vander Wal et al. (2006b), it is found that the mathematical expressions are similar that $K_c = K_m^{1.6}$ and $K_v \approx K_m$. The fine tunings in the expressions indicate that numerical adjustments of the exponents have been used to find better fits.

6. The discrepancies between different models, or between different levels of values in the same model, suggest that it is difficult to find a universal model to describe various conditions.

2.6.2 Characterization of Bouncing

Bouncing occurs when the impact energy is low, and it is adjacent to two different coalescence regimes. Bouncing is less investigated than splashing may due to the following reasons:

- Bouncing exists in more narrow ranges of diameter and velocity than high-energy impact phenomena such as coalescence and splashing/jetting, and thus it may not be the dominant phenomenon for many applications.

- Generating bouncing droplets at very low impact energy level, i.e. low velocity and small diameter, is more difficult.

As the inertial energy level is low for the transitions between bouncing and two coalescence regimes, the threshold is very sensitive to the variations of different variables such as diameter and velocity. The transitions were well characterized, in many cases, using simpler mathematical expressions such as constant velocity or Weber number without developing complex models.

- Bach et al. (2004) characterized the transition between low-energy collision coalescence and bouncing. Different dimensionless parameters including the Weber number and the Knudsen number were used to characterize the thresholds. Water was used in the experiment.

- Bartolo et al. (2006) characterized the two transitions between bouncing and the two coalescence regimes simply using the impact velocity. Water was used in the experiment.

- Pan & Law (2007) used the Weber number to characterize the transition from bouncing to coalescence. The experimental fluids were tetradecane and dodecane.

- Huang & Zhang (2008) investigated transition of bouncing-coalescence besides splashing and jetting. The model, Eq. (2.17), is the same as the one for splashing and jetting but with different value of K_h ($K_h = 13$).

Conclusions on Bouncing Characterization

Due to the insufficient work on low-energy impact, investigations with more fluids need to be carried out to obtain further improve the understanding of bouncing.

2.7 Summary of the Chapter

- The focused regimes, jetting, coalescence and bouncing in this work are defined and described specifically with schematic drawings, and the mechanisms for the phenomena are investigated through a literature review. The intermediate gas film plays an important role in low energy impact as coalescence and bouncing depend on the elimination or breaking of the film. The liquid layer thickness is very influential to the characteristic observations such as crown formation and breaking in the high-energy impact as a deep layer tends to absorb the impact and change the outcomes.

- Dimensionless parameters are very useful in characterizing the thresholds as the parameters can account for effects from different sources. The empirical models in the literature show that the Weber number and the Ohnesorge number are the most commonly used combination of the dimensionless parameters for characterizing the threshold of coalescence-splashing/jetting (the Reynolds number can also be presented as a combination of the Weber number and the Ohnesorge number). The Weber number is used for determining the threshold between coalescence and bouncing, and the restitution coefficient is investigated in bouncing to study the energy loss during the impacts. The restrictions such as too few data points, narrow ranges of velocity and diameter, insufficient study on micro-level droplet and very few fluids, and lack of threshold for jetting etc. indicate the need for more research.

Chapter 3

Experimental Methods

3.1 Introduction

This chapter describes the experimental apparatus in the present work. An overview of the experimental setup is given at the beginning, and it is followed by detailed descriptions of various parts in the experimental setup. The physical properties, density, viscosity and surface tension, were obtained from the literature and also from the measurements carried out in this work, and the values from different sources are compared and selected. The measuring methods for their physical properties are also described at the end of the chapter.

3.2 Overview of the Experimental Setup

The phenomena were observed and studied using high-speed visualization techniques. This section gives an overall description of the experimental apparatus, and more detailed description of the components of the apparatus is given after this section.

Figure 3.1 shows the experimental setup. The schematic overview of the experiment is shown in Figure 3.2, and the experiment consists of three main parts:

- Phenomena-generation:
  One of the critical components in this part was the test cell, inside which droplets impacts were generated. A nozzle for generating droplets was mounted on the lid of the test cell. An optical cuvette on a cylindrical stage was placed in the middle of the test cell. The four surrounding walls were mounted with optical glasses made of quartz for the observation purposes. On the front side of the test cell, there were four ports, T_1, T_2, P and V. T_1 and T_2 were for temperature
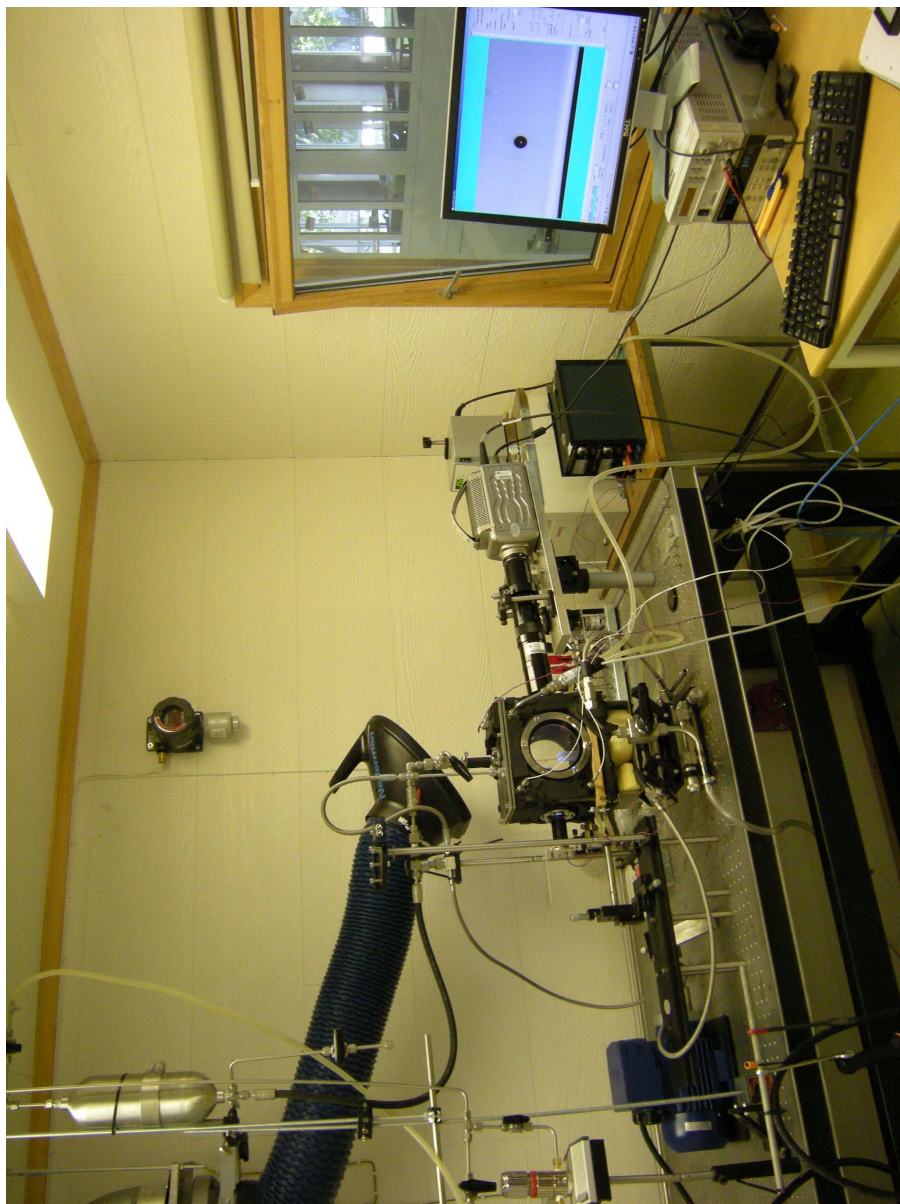
Figure 3.1: Picture of the experimental apparatus.
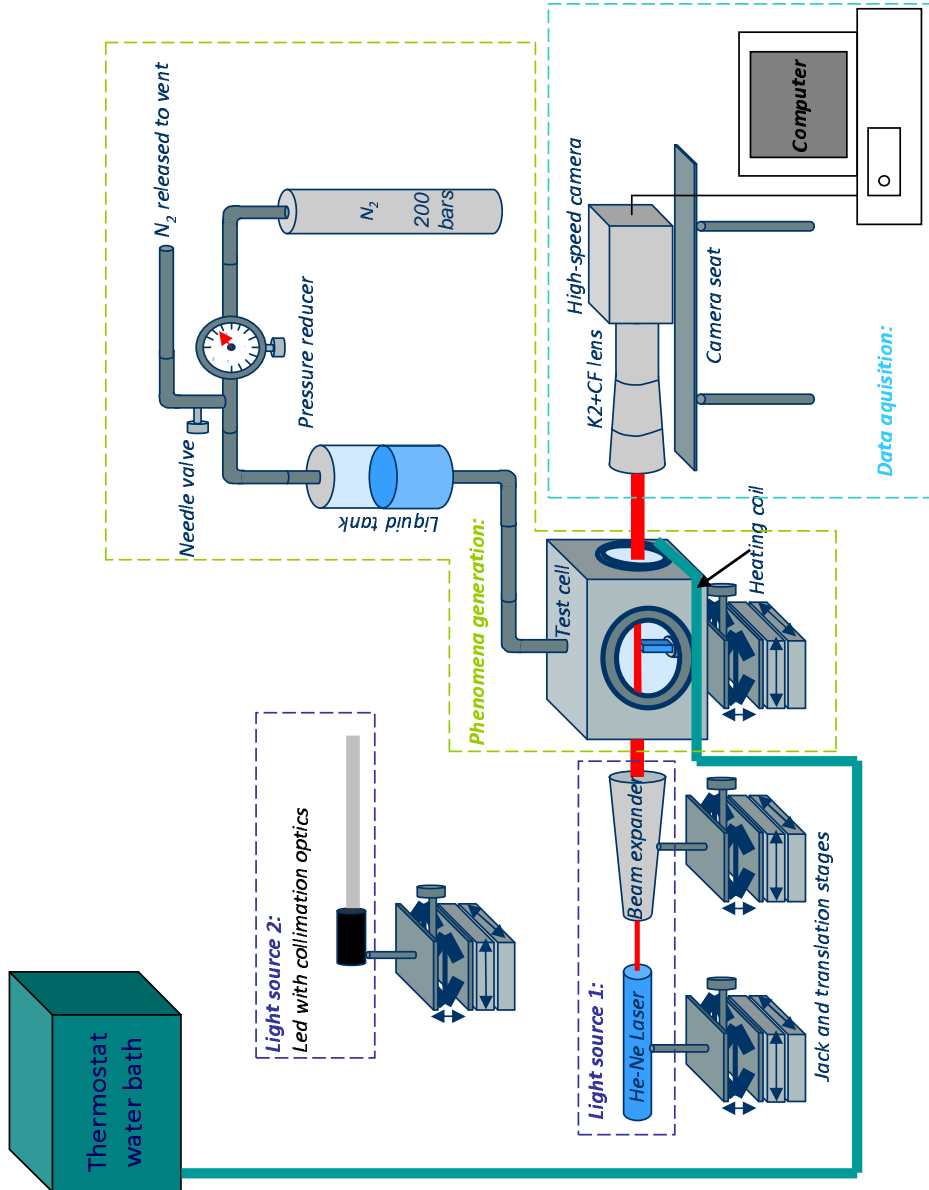
Figure 3.2: Schematic drawing of the experimental apparatus. (Figure from Sevault (2008) with modifications)

sensors. P and V were for pressure transducer and ventilation, respectively. The liquid tank in the figure contained the fluid which was used for generating droplets. The pressure exerted in the liquid tank was given by the nitrogen cylinder and could be controlled through the reducer and the needle valve. In case temperature adjustment was needed, the thermostat water bath circulates heated water to the copper coil coupling around the bottom of the test cell.

- Light source:
  During the investigation, two light sources were used. Light source 1 was a Helium-Neon laser with a beam expander. The light source 1 was used when the experiments with the first two fluids, distilled water and technical ethanol, were carried out. Light source 2 was a white light LED collimated by different optical lenses. Figure 3.1 shows the setup with the LED light source.

- Data acquisition:
  A high-speed camera mounted with a long-distance microscope and close-focus lens was used to capture the phenomena. The data was transferred and stored in a computer for analysis.

Components in the three main parts are described in the following sections.

3.3 Components in the Experiment

3.3.1 Test Cell

The test cell is given in Figure 3.3(a), and Figure 3.3(b) shows a three-dimensional schematic drawing of the test cell.

The assembly and main dimensions of the test cell is shown in Figure 3.4.

The test cell was a core component in the phenomena-generation part, and it integrated different components that were necessary for the present experiments. More specifically, the following main components were integrated in the test cell.

- A droplet generator on the top of the cell.

- A cabling port, for an electronic shutter, on the top of the cell.

- A deep pool placed in the middle of the cell.

- Two temperature sensors on the front side of the cell.
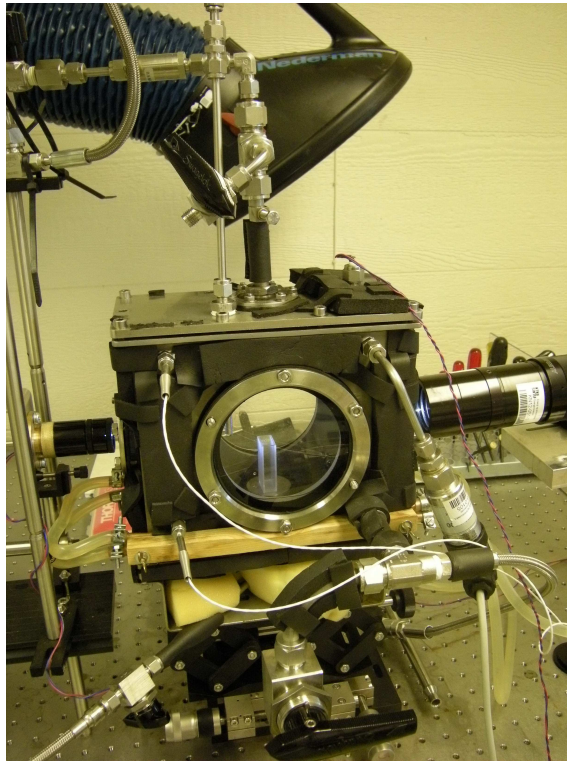
(a) Picture of test cell.
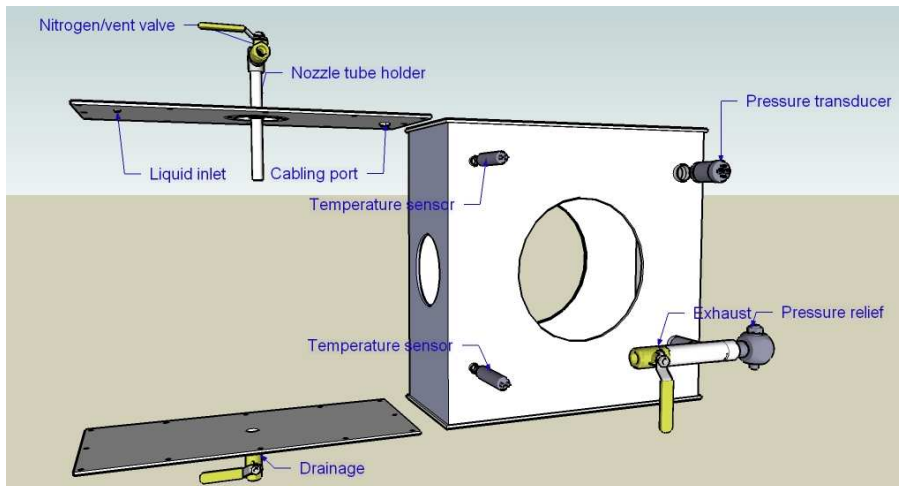
(b) Schematic drawing of test cell.

Figure 3.3: Test cell overview.
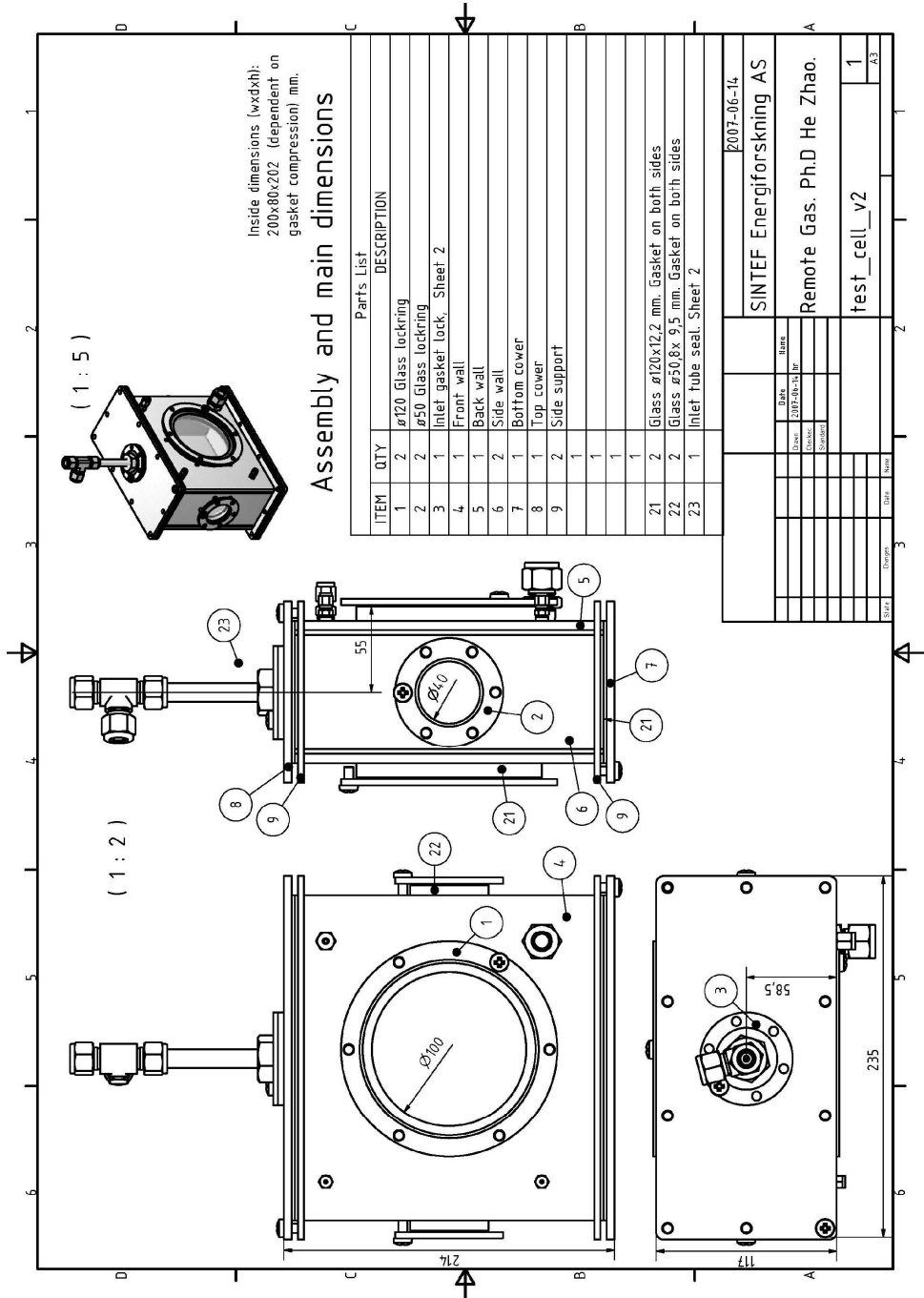
Figure 3.4: Assembly and main dimensions of the test cell (Figure made by Mr. Håvard Rekstad).

- A pressure transducer on the front side of the cell.

- A gas-loop which includes a nitrogen purging port on the top and a gas-outlet on the front side of the cell.

As shown in Figure 3.3(b), the test cell consists of three main parts, which are cell lid, cell bottom and cell body made of stainless steel. The lid and the bottom were made from one-piece plates, and the body was welded. The cell can withstand over pressure (1.5 bar, absolute) and vacuum (1 mbar, absolute).

Cell Lid

Figure 3.5 shows the lid of the test cell. The main components in the picture are marked.

A tee was mounted on the the nozzle tube holder. One end of the tee connected with a valve for nitrogen purging and for vacuuming the test cell, and the nozzle tube could be tightly fixed inside the holder from the other end of the tee. The nozzle tube holder was fixed in the middle of
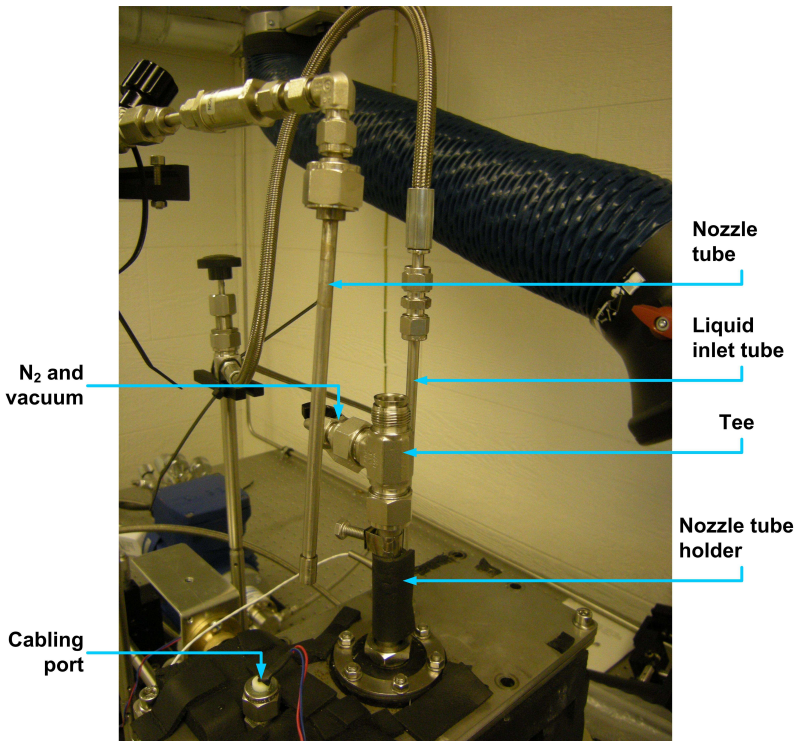
Figure 3.5: Picture of the cell lid.

the lid with a circular rubber gasket and a bolt, and the gasket was tightly locked by a metal flange. The radial direction of the hold could be slightly adjusted due to the flexibility of the rubber gasket. A cabling port was located near one edge of the lid for leading the cable of an electronic motor, and a Teflon plug was inserted in the port for sealing the cabling port gas-tightly. Another port for the liquid inlet was located at the opposite edge of the cabling port. The liquid inlet port is denoted in the schematic drawing of the test cell (Figure 3.3(b)), while it cannot be seen in Figure 3.5 due to the hindrance of the nozzle tube holder. Only the liquid inlet tube is shown in Figure 3.5.

Cell Bottom and 3D Positioning Base

A drainage was located at the center of the bottom. In the present work the drainage was closed by a valve, while the valve will be opened for circulating liquid to generate liquid film in future experiments. The bottom of the cell was adapted to a seat which can be mounted on a heavy duty lab jack (Thorlabs, L490). The lab jack can vertically adjust the position of the test cell but not transversally. In order to tune the position of the test cell transversally, the jack was mounted on two stacked translation stages (Thorlabs, LNR50M) for realizing x-y adjustment.

Cell Body

Figure 3.6(a) shows the front of the cell body. The dimensions can be found in Figure 3.4. The front of the cell body was nearly square, and the inner length of the front square was 200 mm. Figure 3.6(b) shows the side of the cell body, and the inner width of the side was 80 mm. The considerations for choosing the dimensions are:

- The side dimension ($80\,\text{mm} \times 200\,\text{mm}$): The focal length of the CF1 objective was around 40 mm, and so the camera was able to capture the phenomena with the CF1 lens through the side-path (80 mm) when the phenomena was set in the center of the cell.

- The front dimension ($200\,\text{mm} \times 200\,\text{mm}$): The cell should have large enough space so that it was able to enclose necessary apparatus for the experiment and for modification of the experiment.

Customized laser windows (Thorlabs) made of BK7 material which was a type of borosilicate crown glass with low refractive index and low dispersion were mounted on the cell body by metal flanges. The diameter of the front windows was 120 mm which was larger than the side windows (diameter
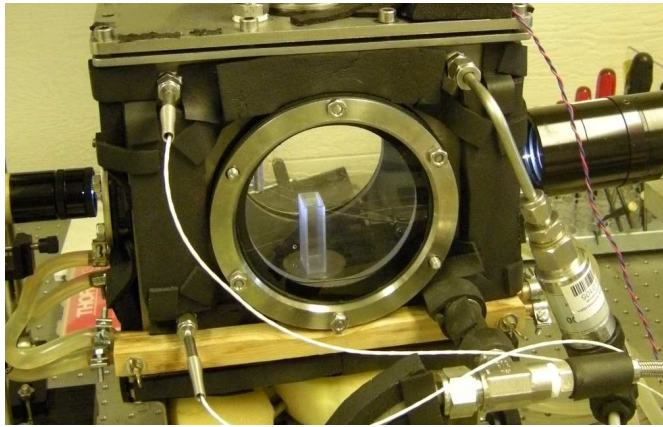
(a) Cell front.
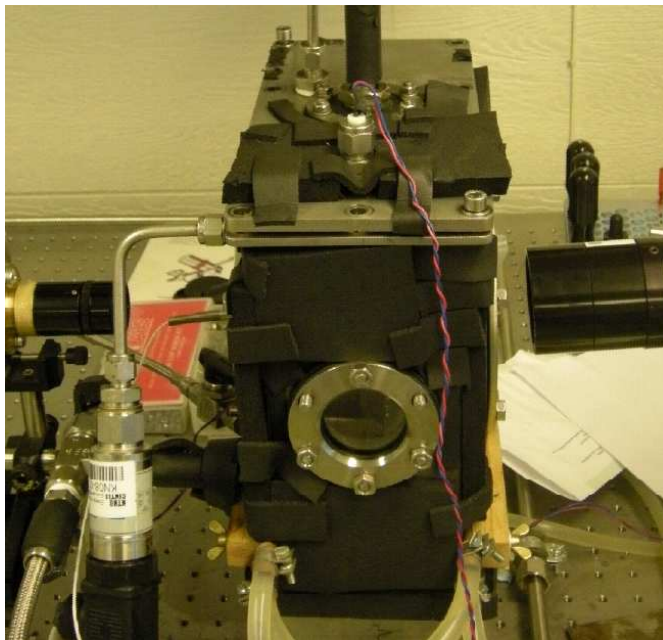
(b) Cell side.

Figure 3.6: The front and side of the test cell.

50.8 mm) as the cell front was larger than the cell side, and the experiment can benefit from a larger visualization area when trying to investigate the phenomena at different locations. Due to the larger window area, the front windows were thicker (12.2 mm) than the side window thickness (9.5 mm) for having a better strength. A rubber gasket made of neoprene with a good chemical resistance to the experimental fluids was used to ensure the sealing of the windows.

Four ports can be found on the front of the cell body. Two ports on the left side were used for temperature sensors (PT100). The upper port on the right side was used for pressure transducer (PXT1400). The port on the bottom of the right side was used for a gas outlet on which two valves, a manual valve and a safety valve, were mounted. The manual valve was for fast release of the gas in the test cell, and it was useful, for instance, when flushing nitrogen into the test cell. The safety valve was calibrated to be opened when the pressure was over 1.3 bar (abs) which was below the design pressure for the test cell (1.5 bar, abs).

Inside the Cell

Figure 3.7 shows the schematic drawing of the arrangements inside the test cell. A single stream of droplets was generated from a nozzle located in the center of the test cell, and the droplets were screened by a fast-rotating shutter mounted on an electronic motor. A cuvette was placed on a cylindrical seat on the bottom center of the cell.

3.3.2 Droplet-Generation System

Droplet generation is a critical element in the experiment. The apparatus for generating a single stream of droplets in the micron-scale level (below 1 mm) is described in this section.

Overview of the Droplet-Generation System

The schematic drawing of the droplet generator system is shown in Figure 3.8(a) and (b). The main parts are denoted in the figures.

Droplets were generated through the Plateau-Rayleigh instability according to which a liquid jet breaks into small droplets due to the surface tension. The liquid jet was generated from the nozzle mounted on the nozzle tube. A filter of 5 μm nominal pore size was placed between the liquid bottle and the nozzle tube for filtrating impurities which might block the nozzle. Scientific level nitrogen (99.9999%) was used to pressurize the liquid in the liquid bottle for generating the liquid jet, and thus the characteristics of the liquid jet and the droplets were decided by the pressure exerted on the

liquid side. In order to vary the pressure accurately and fast, two pressure regulators were used. The first one was for coarse regulation within 15 bar, and the other was for the fine regulation within 1 bar. A release valve was for fast reducing the pressure in the liquid bottle.

In the droplet-generation process, the nitrogen pressure in the liquid bottle was first increased using the coarse regulator. The liquid jet was generated until a certain starting pressure was overcome, and at this point, the droplet velocity were relatively high that the dominant phenomenon was splashing/jetting. In order to decrease the velocity for generating coalescence and bouncing, the pressure must be reduced. The release valve was used to lower the pressure quickly, and the fine regulator were used to tune the pressure finely as bouncing existed in narrow ranges of velocity and diameter.

Liquid Bottle

The bottle was a 1 litre sampling cylinder (Swagelok, 304L-HDF4-1000) made of stainless steel, and the bottle can sustain pressure up to 124 bar. There were two ends on the bottle. A tee on the top end of the bottle connects with the pressure-reduced nitrogen and the release valve. The other tee was placed on the bottom end of the bottle. It connects to the
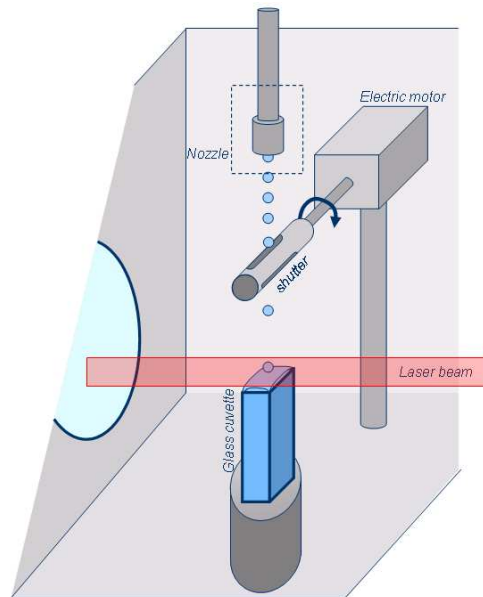
Figure 3.7: Schematic drawing of the arrangement inside the test cell. (Figure from Sevault (2008))
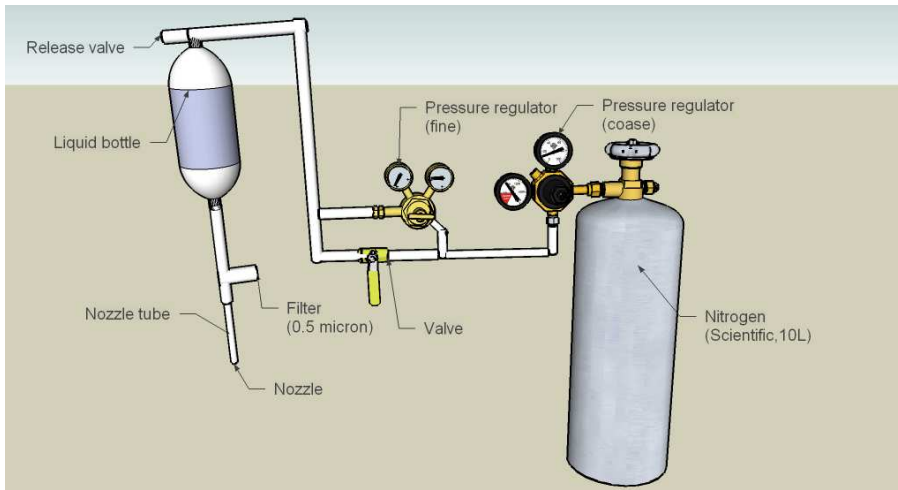
(a) Schematic drawing of droplet-generation system.
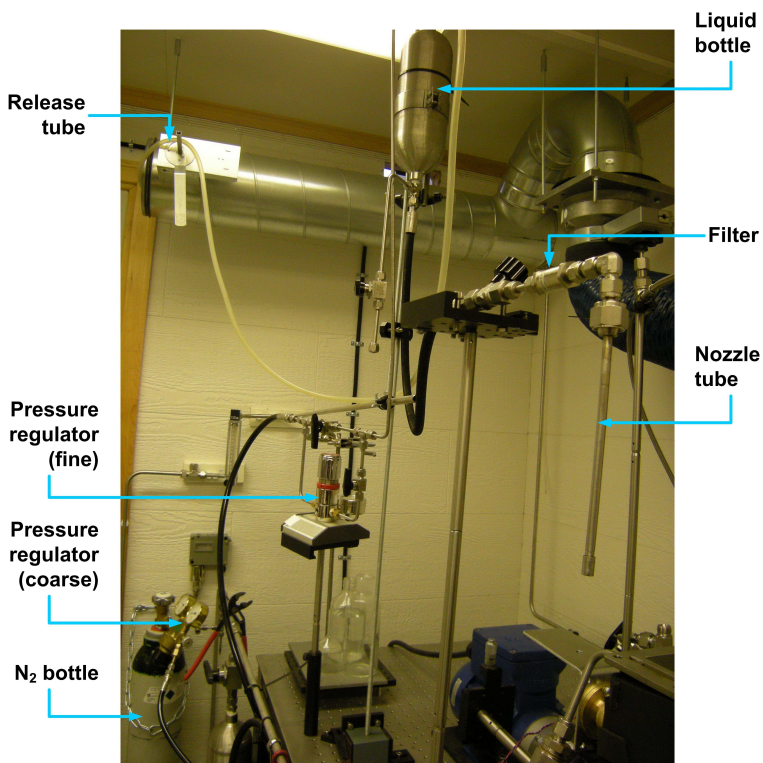
(b) Picture of droplet-generation system.

Figure 3.8: Droplet-generation system.

nozzle tube and a tube which can be used for circulation of the liquid in future experiments.

Assembly of the Nozzle

Figure 3.9 shows the assembly of the nozzle. The assembly consists of several critical parts which are indicated in the figure. In the assembly, a ball valve connected with the tube from the liquid bottle, and it was used for controlling the production of the liquid jet. A filter (Swagelok, 4F series) with a $0.5\,\mu$m nominal pore size was mounted between the ball valve and the nozzle tube for filtering impurities in the liquid. According to the observations in the experiments, the liquid jet was easily affected, either blocked or split, if impurities such as very small particles and fibers got stuck around the nozzle.

Generally, the flow rate in the experiment was below $0.015\,$l/min, and as the usage time increased, the pressure drop increased due to more impurities retained in the porous structure. A certain pressure drop needed to be overcome to reach the flow rate.

Figure 3.10(a) shows the schematic drawing of the main assembly of the nozzle, and a picture is shown in 3.10(b).

The main assembly of the nozzle consists of three parts: the nozzle tube, the laser pinhole and the nozzle cap.
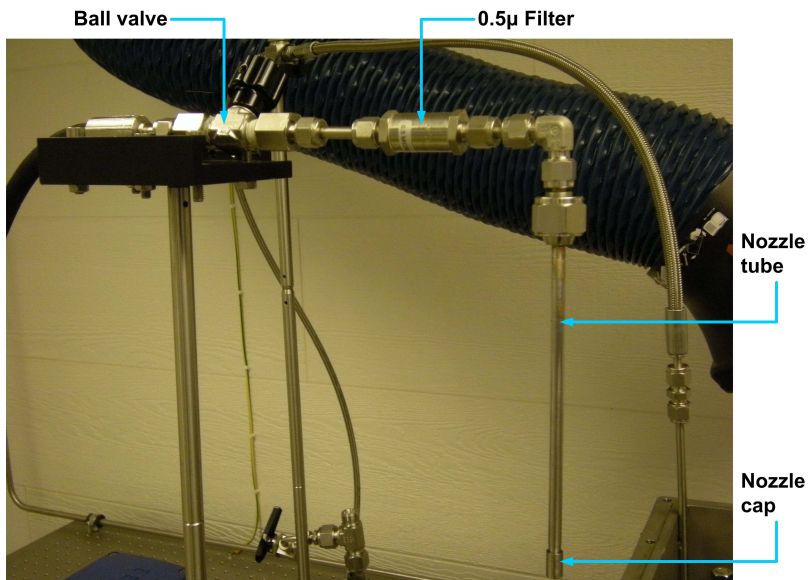
Figure 3.9: Picture of the assembly of the nozzle.
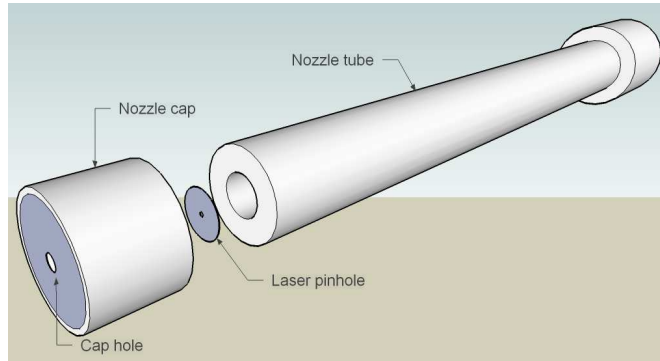
(a) Schematic drawing.
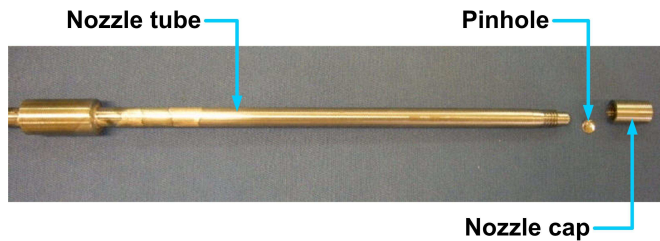
(b) Picture.

Figure 3.10: Main assembly of the nozzle tube.

- The nozzle tube was a 6 mm (o.d.) stainless steel tube. One end of the tube was made with external screw thread so that the nozzle cap can be screwed on, and this end contained an O-ring to press the laser pinhole tightly in the nozzle cap. The other end of a tube was connected to the liquid bottle.

- The pinholes used in the experiments were $20\,\mu$m (P20S), $50\,\mu$m (P50S), $100\,\mu$m (P100S) and $150\,\mu$m (P150S) the mounted-pinholes from Thorlabs. The thickness of the pinholes was $12.5\,\mu$m. A $200\,\mu$m (04 PIP 017) pinhole was the unmounted standard pinhole from Melles Griot, and the thickness was $13\,\mu$m. All the pinholes were precisely cut with the holes centered to fit in the nozzle cap.

- A $1\,$mm cap hole was located in the center of the nozzle cap, and this central hole was for preliminary focusing the laser pinholes. The laser pinholes can be positioned and well-centralized inside the nozzle cap.
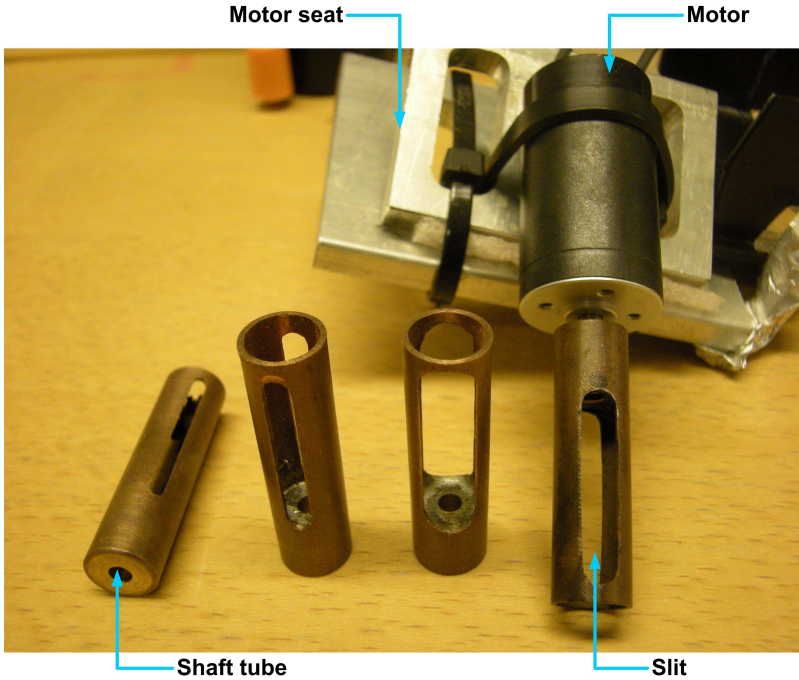
Figure 3.11: Picture of the assembled fast-rotary shutter and unmounted shutters.

3.3.3 Fast-Rotary Shutter for Isolating Droplets

The droplets generated from the nozzle needed to be isolated because the neighboring droplets could affect the impact outcome of a droplet if the impact frequency is high. In the present work, a fast-rotary shutter which can reduce the impact frequency by screening a large number of droplets is presented.

Figure 3.11 shows an assembled fast-rotary shutter and unmounted shutters. The assembled shutter consists of two parts, an unmounted shutter and an electric motor (Faulhaber, 1935 BRE-009BRE).

The unmounted shutter was made of a copper tube. A pair of slits were made on the tube, and when a stream of droplets passes through, some of the droplets were screened by the fast-rotating shutter and only a part of them can go through. A droplet passing through the shutter must satisfy the condition that it falls in either one of the slits when it intersects the surface of the shutter. Shutters with different slit-widths were made as shown in Figure 3.11, and the slits of different sizes can give different "opening-time" during which a droplet can go through. The shaft tube was

welded on one end of the unmounted shutter, and the shaft of the motor can be inserted in the shaft tube as shown in the figure.

The motor was a brushless DC motor with a shaft of 3 mm in diameter. The speed range and nominal power were the two most important parameters for choosing the motor. The speed range should preferably be as wide as possible so that the shutter was able to filtrate a single stream of droplets with a wide range of impinging velocities. The nominal power was very important when it comes to the safety analysis because the motor was placed in the test cell where flammable fluids were used. The minimum power for generating sparks is 2.5 Watt, and thus the power of the electronic device in the test cell must be limited below this level to avoid sparks. The motor had a wide speed range of 1600-10000 revolution per minute (RPM) depending on the voltage. The nominal power was 0.315 Watt which was safe with a reasonable margin of power.

3.3.4 Liquid Pool

Figure 3.12 shows the picture of the cuvette for generating a deep liquid pool.
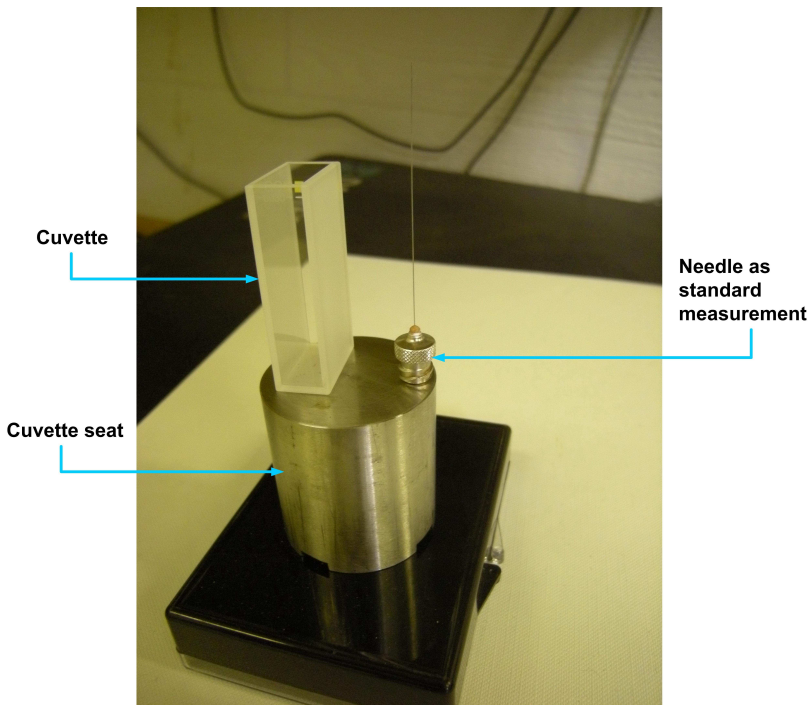
Figure 3.12: Picture of the cuvette for generating a deep liquid pool.

In the experiments, two cuvettes (Hellma, QS101 and OG6030) with the same inner dimension (Height: 42.5 mm, Width: 10 mm, length: 20 mm) were used. The deep liquid pool was generated by filling the cuvette fully to its top, and the droplets impinged on the free surface of the fluids in the cuvette. Considering a droplet of 1 mm in diameter impinging in the center of the cuvette, the pool depth was 42.5 times the diameter, and the distances to the surrounding walls were 5 and 10 times the diameter. In the present study, the maximum droplet size was around 0.7 mm, and most of the droplet sizes were far below 1 mm. So, influences from the bottom of the pool and the surrounding walls can be neglected. A needle (Hamilton, Gauge 33) with outer diameter of 0.21 mm was used as the standard measurement (gauge) for converting the length-measurements from the image-processing unit, pixel, into the standard length unit, millimeter. The cuvette and the needle were put on the cuvette seat which was a stainless steel cylinder. The seat was placed in the center of the test cell, and the bottom of the seat was hollowed to enable the fluids to flow into the drainage, which was located below the seat.

3.3.5 Light Source

Two light sources were used in the experiments. The first light source was a Helium-Neon laser (LIMAB, RC 2), and it was used in the experiments with distilled water and technical ethanol. The second light source was a white light LED (Seoul, ZLED-N), and it was used in the experiment with n-pentane, methanol and 1-propanol.
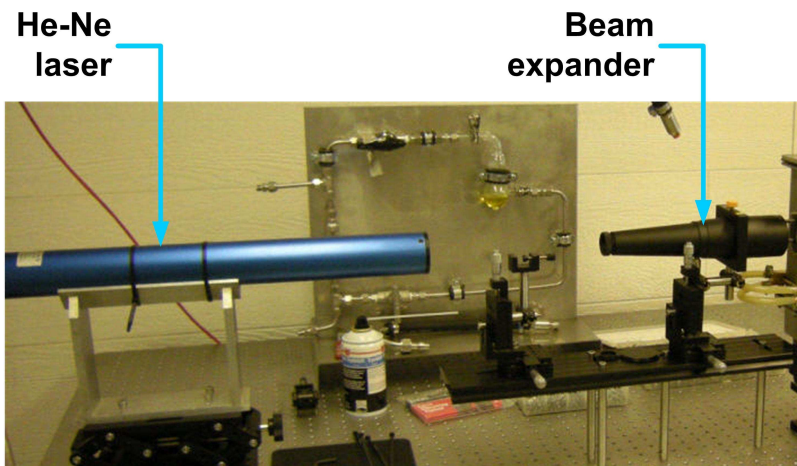
Figure 3.13: Picture of the He-Ne laser and beam expander.
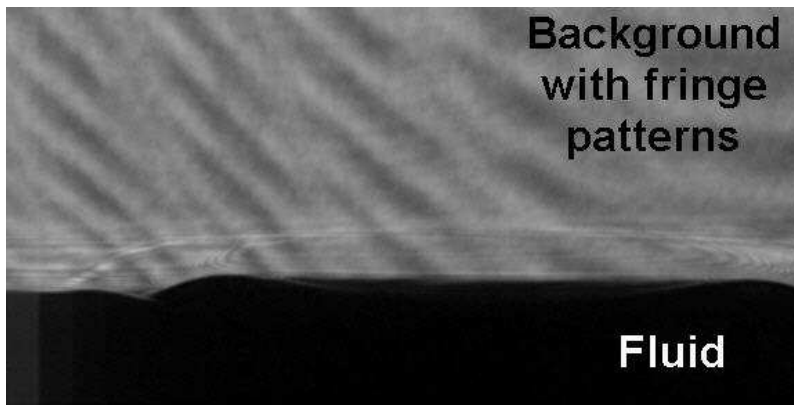
Figure 3.14: A picture taken by using He-Ne laser shows fringe patterns.

The first light source, He-Ne laser, was used with a beam expander (Thorlabs, BE20M-A). Figure 3.13 shows the He-Ne laser and the beam expander. The wavelength of the He-Ne laser was 632.8 nm, and the output power was 2 mW. The expander can enlarge the diameter of the input laser beam by 20 times, and the output beam was collimated. The anti-reflection coating range was 350-650 nm which was suitable for the laser. The laser was placed on a heavy duty lab jack (Thorlabs, L490) for height adjustment, and the beam expander was placed on two stacked translation stages (Thorlabs, MT1/M) for vertical and transversal adjustment.

The problem of using this light source was the light interference. The interference occurs as two or more coherent waves superpose (Bennenson et al. 2006). The coherence is "a property of electromagnetic waves which are in phase in both time and space" (Al-Azzawi 2006). The He-Ne laser generates single-wavelength light which was very coherent and can be easily interfered during the transmission. The result was that it produced fringe patterns in the picture background such as shown in Figure 3.14. The fluid in the figure is an object, and the background is the observation above the fluid. In the ideal case, the background should be purely white, and the object is purely black. Due to the interference, the background contains black and white patterns (or patterns of different gray-levels) in the case displayed in the figure. The black patterns introduces noise to the picture when the picture is later converted into the binary picture (only black and white) for image-processing.

The second light source was a white light LED. Emitted light from the LED must be collimated by using necessary lenses. Figure 3.15 shows the assembly parts for the white light source. Either a plano-convex lens (Edmund optics) or a double-convex lens can be used to collimate the light.
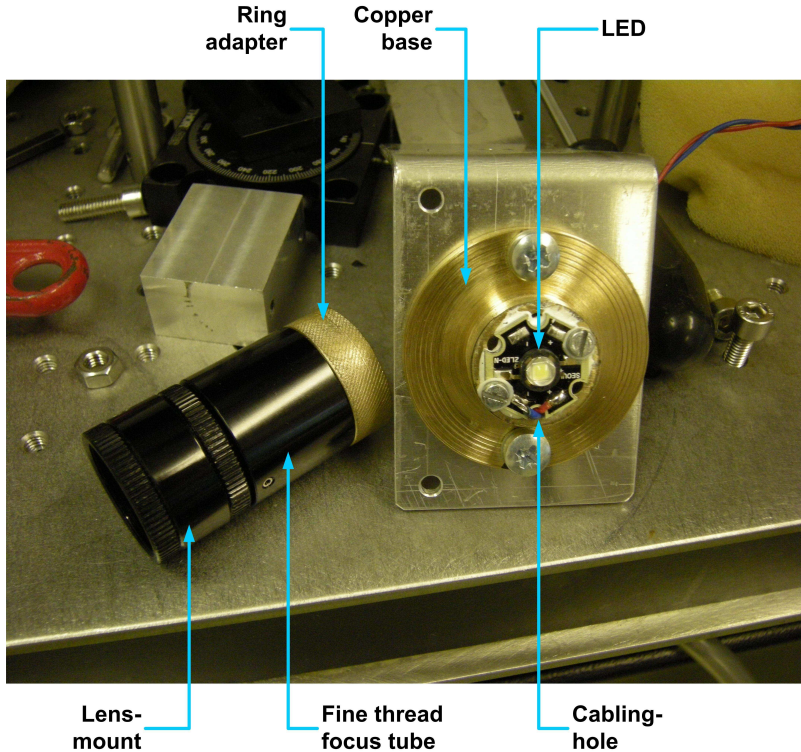
Figure 3.15: Picture of the assembly for the white light LED.

The effective focal length was 40 mm, and the diameter was 25 mm for both chosen lenses. A suitable lens-mount (Edmund optics, simple/thin lens mount) with the appropriate diameter and edge thickness was chosen to mount the lens, and a distance-adjustable tube (Edmund optics, fine thread focus tube) was connected with the lens-mount for adjusting the focus for generating the collimated light. The LED was mounted on a copper base (lab-made) by using a ring-adapter (lab-made), and there were cabling holes drilled on the base for leading the LED cables and mounting fixing screws. The copper base was also used as a heat sink for the LED with a thin layer of thermo paste (white matter around the LED) smeared between the surface of the LED and the surface of the base.

The white light has multiple wavelengths, and it is much less coherent than the monochromatic light. It can be seen in Figure 3.16 that the fringe patterns were reduced by using the white light.

Table 3.1: Specifications of the CF series objectives tested using an 1/2-inch camera sensor and an 13-inch monitor (Edmund Optics ^{TM} Ltd. 2009).

Objective	Primary magnification	System magnification	Field of view	Working distance
CF-1	2.1-0.8×	86.7-33×	3-8 mm	286-715 mm
CF-2	4.1-2.4×	169-99×	1.56-2.7 mm	144-222 mm
CF-3	5.6-3.8×	231-157×	1.1-1.7 mm	96-132 mm
CF-4	9.8-7.7×	405-318×	0.65-0.8 mm	54-63 mm

3.3.6 High-speed Camera

As one of the most critical parts in the high-speed photography system, the camera must be mounted solidly and stably. This section describes the mount of the camera.

Figure 3.17 shows the mount of the high speed camera which was slightly tilted (objective-lens downwards 3.6°) from the horizontal plane.

In order to magnify the observation, a long-distance microscope (Infinity, K2) with a close-focus objective (Infinity, CF series) were adapted to the high speed camera (Vision Research, Phantom V9.1). Table 3.1 shows the specifications of the CF series.

The situation in the environment of the Phantom V9.1 camera and the PC monitor varied a little from the table, but it was useful to have an overview of the working ranges and to choose the right objective from this table. Most of the experimental videos were captured using the CF-3 objective with which a reasonable magnification, observation area and working distance could be reached.
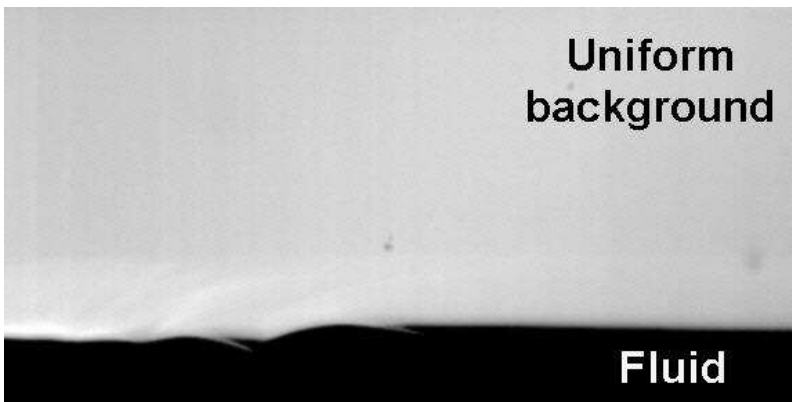
Figure 3.16: Homogeneous background obtained using the white light.

According to the experimental design, the seat needs to be lifted and fixed stably on a certain setup, and it must be able to adjust the angle of the seat. A thick and strong post (LINOS, post 38-350-M M6) was used as the main support. The seat was mounted on a angle bracket (LINOS, angle bracket 80-M), and an arc-slot on one side of the bracket can be attached to a clamping block (LINOS, clamping block 38-M) for adjusting the angle of the seat.

The highest resolution of the camera is 1632×1200 pixels, and the maximum frame rate at the highest resolution is 1000 fps. It can be operated at minimum $2\,\mu s$ exposure time. In most of the experiments, the resolution was set at 576×288 pixels, and the frame rate at this resolution was 9216 fps. The exposure time was in a range of 5-10 μs.

3.3.7 Data Logger

The temperature sensors and pressure transducer mounted on the test cell are shown in Section 3.3.1. The temperature and pressure data were converted into electronic signals which were read and recorded by a data logger (Hewlett Packard, 34970A). The data logger was connected with the
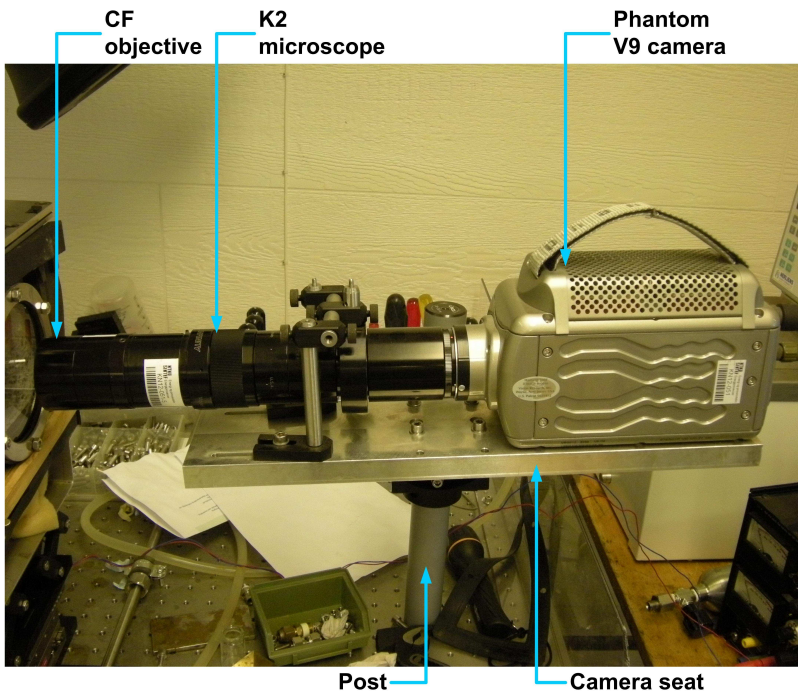
Figure 3.17: Mount of the high speed camera.

PC, and it has 20 channels. In the experiment, two channels were for two temperature sensors and one channel was for the pressure transducer. The interval for data logging was set to 10 seconds.

Due to safety reasons, the temperature sensors and the pressure transducer could not directly connect with the data logger because the computer or the data logger might generate power which could be conducted to the test cell, and if the power was higher than 2.5 Watt, sparks could be generated and created an explosion. Thus, power barriers were needed to restrict the power conduction to the test cell. The power barrier for the temperature sensors was a temperature signal converter (GM International Safety, D1072D), and the power barrier for the pressure transducer was a pressure signal converter (GM International Safety, D1014D).

3.3.8 Components for N-pentane Experiment

This section describes the two important components, a heater and a vacuum pump, in the procedures.

Heater

The heater used for heating the test cell was a water bath (Julabo, 12). The heater consists of water bath and a pump, and the pump was used to transport the heated water to a desired place such as the copper coils around the test cell in the experiment. The temperature was controllable, and it had a function for over temperature control.

Vacuum pump

A vacuum pump (Leybold S 1.5) was used in the n-pentane experiment for vacuuming the test cell. The vacuum level was dependent on the capability of the pump and the gas-tightness of the test cell. In the present setup, the pump could vacuum the test cell below 1 mbar.

3.4 Safety Measures

As flammable fluids were used, Section 3.3 refers several times to the safety considerations in the material and equipment selection. Table 3.2 summarizes the safety measures in the equipment selection.

Besides the measures in the table, all the electronic equipment such as the computer, data logger and power supplies were placed out of the optical table where the experiments were carried out. The location of the test cell was semi-isolated from the surrounding equipment by a barrier made of plexiglass.

Table 3.2: Safety measures in the equipment selection.

Equipment	Danger	Safety measures	Referred section
Safety valve on cell	Overpressure	Safety valve 1.3 bar	3.3.1
Windows on cell	Overpressure	Thick glass $\approx 10\,\mathrm{mm}$	3.3.1
Motor for shutter	Explosion	Brushless, low-power	3.3.3
Power supply	Explosion	Current/voltage control	3.3.3
T. P. sensor	Explosion	Power barrier	3.3.7
Heater	Explosion	Safe zone	3.3.8
Overall	Explosion, toxicity	Ventilation	3.2

Power sockets were located on the other side away from the test cell because they might generate sparks. The fluid vapors (methanol, ethanol, 1-propanol and n-pentane) were heavier than air they tend to flow downwards the floor, and so the sockets were placed on the middle of the wall.

Three gas detectors for hydrocarbon gases (n-pentane in this experiment) were distributed around the laboratory. Two of them were mounted on the top and bottom of the wall, and the other one was mounted in the main ventilation. When a flammable gas was detected, an alarm and an emergency light installed out side the room will be triggered to inform the personnel for the evacuation, and the electricity in the room will be cut off. An emergency shut down switch can also be found in the laboratory.

3.5 Experimental Fluids

3.5.1 Overview

This section describes on the fluids which were used in the experiment. The similarity of the physical properties of n-pentane to the mixed refrigerants was introduced in the first part of this section. In the second part, the physical properties obtained from different sources are described. Some of the properties of the experimental fluids were measured in the present work, and they were compared with properties from the literature.

3.5.2 Comparison between N-pentane and the Mixed Refrigerants

Definition of the Mixed Refrigerants

Two sets of mixed refrigerants, MR1 and MR2, were defined as the basis for comparison. MR1 and MR2 consist of typical mole-concentrations of

Table 3.3: Specified general mixed refrigerants and corresponding conditions (pressure assumed 4.5 bar).

Refrigerant(mole%)	MR1	MR2
Nitrogen	0	10
Methane	5	55
Ethane	90	35
Propane	5	0
Sum	100	100

refrigerants which have been commonly used in LNG processes. Table 3.3 shows information on the specified mixed refrigerants.

Comparison between Physical Properties of N-pentane and the Mixed Refrigerants

Lex et al. (2007) used 80 mol% n-pentane and 20 mol% iso-octane as the model fluid for mixed refrigerant. A possible problem of using a mixture was that the composition could vary as there might be temperature gradients in the test cell. Pure n-pentane was therefore selected to avoid composition change in the present experiments. An attempt was made to compare the physical properties of the test fluid with those of the mixed refrigerants, and the data of water and air was also investigated to serve as a reference. The chosen physical properties are liquid viscosity, surface tension, liquid density, vapor viscosity and vapor density.

Fluid properties were taken from Aspen HYSYS 2006. The Peng-Robinson correlation was suggested to be used as the thermodynamic method for both the test fluid and the mixed refrigerants by ThermSel V1.0 which was a thermodynamic package selector for HYSYS, and the SRK correlation was recommended for air and water system. Detailed description of methods, results and discussion is given in the following sections.

The temperature conditions for comparing n-pentane and the mixed refrigerants are listed in Table 3.4, and water was chosen as a reference.

Figure 3.18(a) to (e) compare n-pentane (black curve) and two sets of mixed refrigerants (green and blue curves) regarding liquid viscosity, surface tension, liquid density, vapor viscosity and vapor density, respectively. The properties of water (red curve) were also plotted in the figures as a reference.

Table 3.4: General mixed refrigerants and corresponding operational conditions

Temperature points selected for comparison of properties (°C)									
n-pentane	20	25	30	35	40	45			
MR1	−82	−80	−78	−76	−74	−72	−70	−68	−66
MR2	−160	−150	−140	−130	−120	−110	−100	−90	
Water	20	25	30	35	40	45			
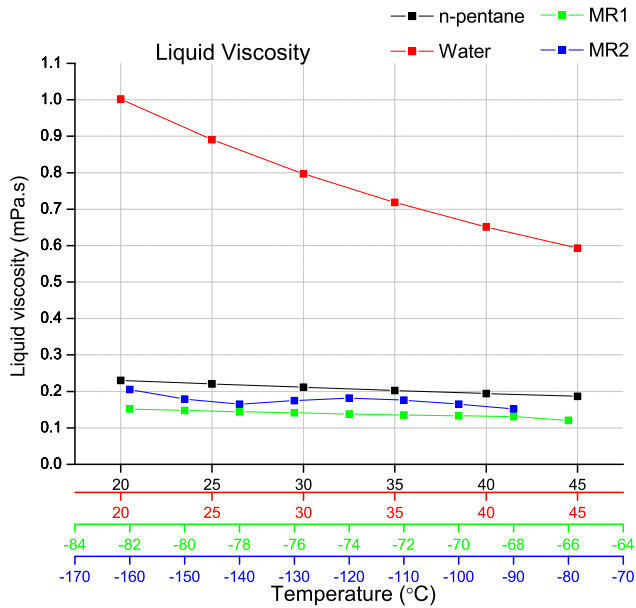
(a) Comparison of liquid viscosity.

Figure 3.18: Comparison between the physical properties of n-pentane and the mixed refrigerants.
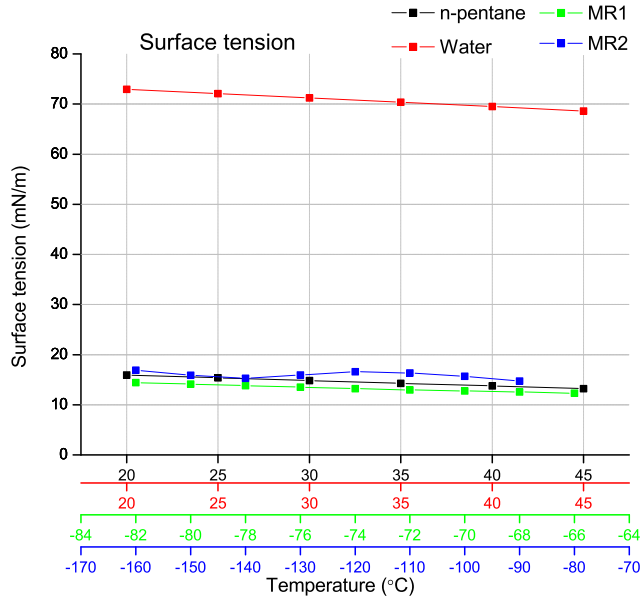
(b) Comparison of surface tension.
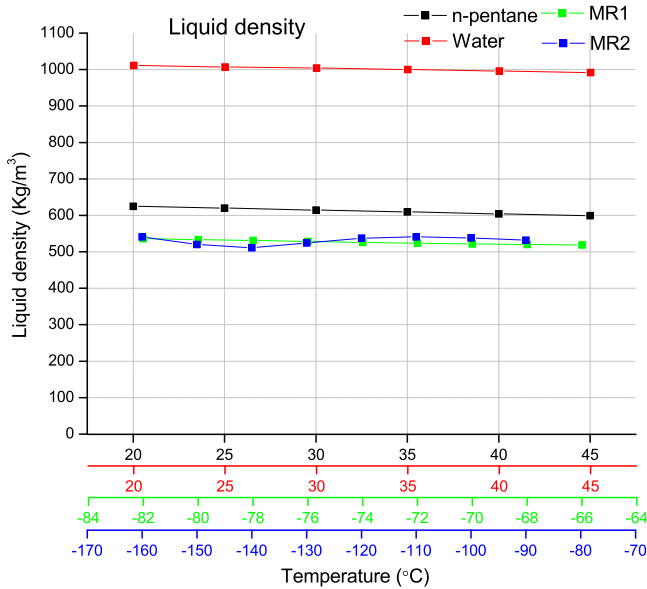
(c) Comparison of liquid density.

Figure 3.18: Comparison between the physical properties of n-pentane and the mixed refrigerants.
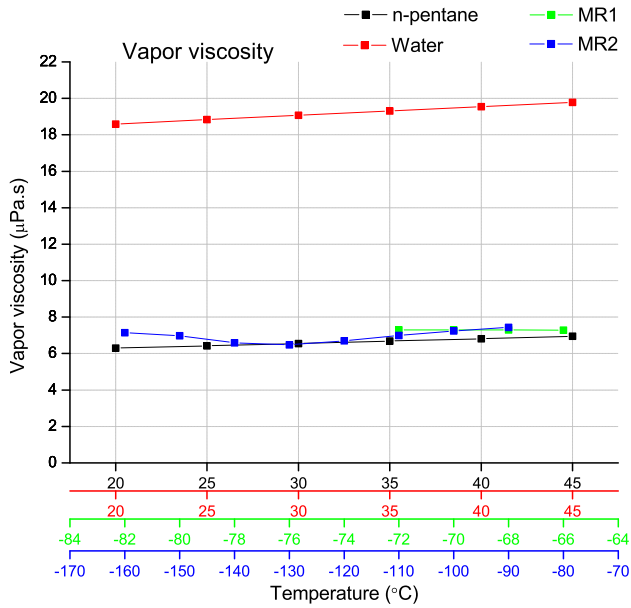
(d) Comparison of vapor viscosity.
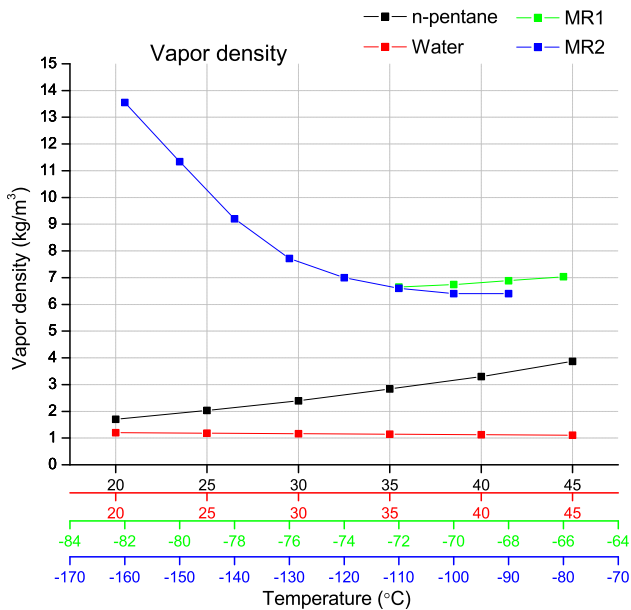
(e) Comparison of vapor density.

Figure 3.18: Comparison between the physical properties of n-pentane and the mixed refrigerants. (Cont.)

Figure 3.18(a) to (e) show that, compared to water, n-pentane shows much similar physical properties to the typical mixed refrigerants, MR1 and MR2. To make a quantitative evaluation of the properties, the following parameters are defined.

$$\bar{\Pi} = \frac{\sum_1^n \Pi_n}{n} \tag{3.1}$$

$$\Omega_1 = \frac{|\bar{\Pi} - \bar{\Pi}_{MR1}|}{\bar{\Pi}_{MR1}} \tag{3.2}$$

$$\Omega_2 = \frac{|\bar{\Pi} - \bar{\Pi}_{MR2}|}{\bar{\Pi}_{MR2}} \tag{3.3}$$

$$\bar{\Omega} = \frac{\Omega_1 + \Omega_2}{2} \tag{3.4}$$

where

- Π denotes a property of a fluid, and $\bar{\Pi}$ denotes the averaged property of a fluid over different temperatures;

- Ω denotes the "difference" between a fluid and the mixed refrigerants. Ω_1 and Ω_2 denote the differences to MR1 and MR2 respectively, and $\bar{\Omega}$ denotes the mean value of Ω_1 and Ω_2.

As can be seen from the equations, $\Omega = 0$ means no difference between a fluid and a set of MR, and thus lower value of Ω means higher similarity of a fluid to a set of MR.

Table 3.5 shows the physical property differences of n-pentane and water to MR1 and MR2. For most of the properties, n-pentane was quite similar to the two sets of mixed refrigerants, and in most of the cases the differences are within 20%. Comparing between n-pentane and water, it can be seen that, in most of the cases, the properties of n-pentane are much closer to the properties of the mixed refrigerants. In the comparison of vapor density, both n-pentane and water are not very close since the differences are above 50%, but n-pentane was still closer.

Table 3.5: Physical property differences of n-pentane (pt) and water (wt) to MR1 and MR2.

Property	Diff. to MR1 (Ω_1)	Diff. to MR2 (Ω_2)	Mean diff. to MR (Ω)
μ_{pt}	0.501	0.187	0.344
μ_{wt}	4.617	3.436	4.024
σ_{pt}	0.096	0.084	0.090
σ_{wt}	4.322	3.447	3.855
ρ_{pt}	0.167	0.155	0.161
ρ_{wt}	0.907	0.888	0.897
$\mu_{\mathrm{pt-gas}}$	0.093	0.047	0.070
$\mu_{\mathrm{wt-gas}}$	1.631	1.764	1.698
$\rho_{\mathrm{pt-gas}}$	0.606	0.685	0.645
$\rho_{\mathrm{wt-gas}}$	0.831	0.864	0.848

Determination of the Experimental Condition for N-pentane

For determining the experimental temperature, two factors were considered. The first factor was the similarity of the physical properties of the test fluid to those of the mixed refrigerants, and it can be seen from the above figures that as the experimental temperature increases from 20 °C to 45 °C the physical properties of n-pentane get closer with the properties of the mixed refrigerants.

The second factor was the saturation pressure which should be preferably close to and slightly higher than the atmospheric pressure so that the danger of overpressure and air suction can be avoided. Figure 3.19 shows the saturation pressures of n-pentane at different temperatures. It can be seen from the figure that when the experimental temperature is higher than 36 °C the saturation pressure becomes higher than the atmospheric pressure. The physical properties of n-pentane at 45 °C are the closest to those of the mixed refrigerants among the chosen temperatures from 20 °C to 45 °C. The saturation pressure at 45 °C is $136 \cdot 10^3$ Pa, and the design pressure will be exceeded if a safety factor of 1.3 is multiplied with this pressure. Due to the above arguments, the experimental temperature were chosen to be 40 °C at which the saturation pressure was $115 \cdot 10^3$ Pa.
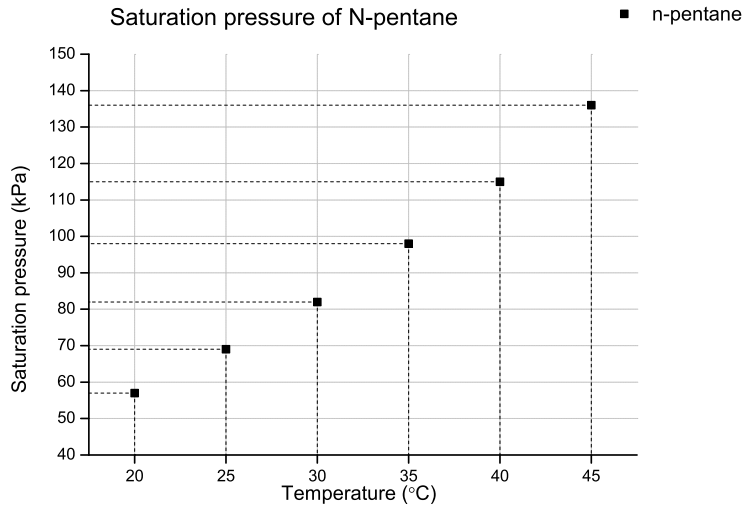
Figure 3.19: Saturation pressure of the test fluid at different tempratures

3.5.3 Physical Properties of Fluids

Physical properties are important in the characterization of the the experimental results. Different values were reported from different sources. In the present work, the physical properties for some of the fluids were also measured in the laboratory. The main reason for carrying out measurements for fluid properties was that the physical properties of the technical ethanol were not certain as the water content was unknown.

The liquid density was measured by using a volumetric pipette (Duran, 20 mm) and a analytical balance (DeltaRange, Mettler AT261).

The liquid viscosity was measured by using two capillary viscometers (Cannon-Fenske-Routine viscometer, 51300/25 and 51303/50) with different measuring ranges (0.5-$2\,mm^2/s$ and 0.8-$4\,mm^2/s$) and a timer.

The surface tension was measured by simply using capillary tubes (Duran, inner diameter 0.8 mm and 0.6 mm). The surface tension can be calculated with known values for the liquid density, capillary size and the rising height of the liquid in the tube.

Table 3.6 shows the physical properties of the experimental fluids from different sources, and an "*" on a fluid means that the data was from the measurements in this work. A measurement value was the mean value of up to 8 samples. The conclusion of the comparisons from different sources was:

Table 3.6: Physical properties of the experimental fluids from different sources.

Fluid	ρ (kg/m^3)	μ (mPa $\cdot$ s)	σ (mN/m)	Source/model
Distilled water(25°C)	1007	0.8904	72.10	HYSYS/SRK
Distilled water(25°C)	996.93	0.890	71.99	Lide (2009)
Distilled water*(25°C)		0.902	72.1	Measured
Technical ethanol (25°C)	810.2	0.9780	29.28	HYSYS/SRK
Technical ethanol (25°C)	810.2	0.9783	29.28	HYSYS/Twu
Technical ethanol (25°C)	838.6	1.001	29.28	HYSYS/BWRS
Technical ethanol (25°C)	745.4	0.9252	29.28	HYSYS/GCEOS
Technical ethanol (25°C)	810.2	0.9783	29.28	HYSYS/G P
Technical ethanol (25°C)	849.6	1.010	29.28	HYSYS/L-K-P
95 vol% Ethanol (25°C)	790	1.16	22.27	Tanaka et al. (1987), Vaquez et al. (1995)
Technical ethanol* (25°C)	805.8	1.367	22.406	Measured
n-pentane(40°C)	605.20	0.1943	13.76	HYSYS/PR
n-pentane(40°C)	605.69	0.1969	13.66	Fröba et al. (2004)
Methanol(25°C)	786.6	0.5486	29.67	HYSYS/SRK
Methanol(25°C)	786.65	0.544	22.07	Lide (2009), Shukla et al. (2008)
Methanol(25°C)		0.546	22.51	Tanaka et al. (1987), Vaquez et al. (1995)
Methanol(25°C)			22.10	Carey et al. (1980)
Methanol*(25°C)	782.64	0.524		Measured
1-propanol (25°C)	799.55	1.968	23.28	Lide (2009), Tanaka et al. (1987), Vaquez et al. (1995)
1-propanol* (25°C)	792.9	1.924	23.78	Measured

- Distilled water: The liquid density was not measured as the density for distilled water was quite consistent in the literature. Even though the viscometers were not very suitable for measuring the viscosity of a fluid with surface tension higher than 30 mN/m, the measurement of water viscosity does not show a very different value compared to the literature. The surface tension of the measurement agrees well with the values from literature. For distilled water, literature data was chosen to be used in the characterization.

- Technical ethanol: The technical ethanol contains 98 vol% of ethanol and 2 vol% of methyl isobutyl ketone (MIBK). The water content was unknown. The properties were calculated by HYSYS, and the values

Table 3.7: The chosen physical properties for the experimental fluids.

Fluid	ρ (kg/m^3)	μ (mPa $\cdot$ s)	σ (mN/m)	Source
Distilled water(25°C)	996.93	0.890	71.99	Lide (2009)
Technical ethanol* (25°C)	805.8	1.367	22.406	Measurement
n-pentane(40°C)	605.69	0.1969	13.66	Fröba et al. (2004)
Methanol(25°C)	786.65	0.544	22.07	Lide (2009), Shukla et al. (2008)
1-propanol (25°C)	799.55	1.968	23.28	Lide (2009), Tanaka et al. (1987), Vaquez et al. (1995)

varies according to different models. Pure or high concentration of ethanol can absorb moisture from the air, and the technical ethanol used in the experiment was "old" (container opened for a long time). High water concentration was assumed, and the reported properties of 95 vol% ethanol-water mixture shows higher viscosity and much lower surface tension. There were uncertainties if the calculated data or literature data of ethanol-water was used. The measurement of the properties were considered to be more reliable and used in the characterization.

- N-pentane: Measurement for n-pentane was not carried out due to the difficulties of creating the environment of pure pentane gas. The calculated data and the reported data were very close, and the reported data was chosen to be used in the characterization.

- Methanol: Values of density and viscosity from different sources were consistent, while the calculated surface tension deviates from the measurement and the reported values. The reported values from the literature were chosen to be used in the characterization.

- 1-propanol: The values from the measurement and the literature were close, and the values from the literature were chosen to be used in the characterization.

The chosen physical properties which were used in the characterization of the results were shown in Table 3.7.

3.6 Summary of the Chapter

In this chapter, a description of the experimental setup, main equipment and experimental fluids is made.

- A test cell was designed and constructed. It has four windows for the visualization of the phenomena. The test cell was gas-tight and strong enough for the vacuum and slightly over-pressure condition.

- Components have been integrated on the test cell for carrying out the droplet impact experiments. The droplet nozzle was fixed at the top of the cell with the possibility of changing impinging angles. Temperature and pressure sensors are mounted on the wall of the cell.

- Droplet impacts were generated in a way that the impact frequency was efficiently reduced by an electrical shutter. The electrical shutter was mounted on the shaft of a motor which was situated on a seat inside the cell.

- Two light sources, a He-Ne laser and a white light LED, were used in the experiments. Due to the interferences of the monochromatic light, fringe patterns were observed when the He-Ne laser was used. The image quality was greatly improved when the white light LED was used.

- A high speed camera was lifted, slightly tilted ($3.6°$ with the objective downwards) and mounted stably on a camera seat.

- Safety issues were carefully considered, and the corresponding measures were made.

- Both theoretical and experimental work was done for determining the physical properties of the experimental fluids.

Chapter 4

Image-processing and Uncertainty Analysis

4.1 Introduction

During the experimental period, $5,319$ raw videos corresponding to around $10,000$ events were captured. The raw videos had to be converted to the individual pictures with the most compatible format (JPEG file) for image processing since the raw video format (CIN file) is not compatible with most of the analyzing tools. The conversion of the raw videos produced $449,930$ pictures, and an efficient method was required to analyze the large amount of pictures. This chapter describes the image processing method which includes the description of the image processing software, ImageJ (Abramoff et al. 2004), for getting the preliminary information such as droplet size and positions (in pixels) and the the post-processing for obtaining the impact parameters such as diameter, velocity and impinging angle (in SI units).

The final results contains uncertainties from different sources. The uncertainties are described and analyzed in this chapter.

4.2 Image Processing

4.2.1 Overview

The fundamental parameters, diameter and velocity, can be manually obtained through the measuring functions integrated in the Phantom camera software. However, this method is not good enough regarding the measuring accuracy and efficiency.

For instance, for each impact, two points of a droplet in the neighboring frames need to be chosen for calculating the velocity, and these two points must be either the same or representative such as the center of mass for calculating the displacement and the velocity. Manually choosing the points

increases the measuring uncertainty because it is difficult to manually pick out the same point of a droplet from two frames and there is not a way in the camera software that can define the center of mass. A similar uncertainty can be found in the diameter measurement where it is not certain that the diameter defined by the two selected points crosses the center of the circle. The measuring efficiency is another main limitation for the manual processing because even for one diameter measurement there can be tens of samples to be analyzed for having an averaged diameter.

ImageJ (Abramoff et al. 2004) was originally designed for processing biological microscopic images, but it can also be applied in other image processing fields such as material, fluid dynamics etc.

The present work uses the basic "Analyze" function to process the images, and with proper measurement settings, the software can automatically identify a droplet and return the information (e.g. area, center of mass, circularity) fast, and by processing the returned information, the demanded parameters (diameter, velocity, impact angle) can be calculated.

4.2.2 Image-processing by ImageJ

The main steps are introduced in this section. The preparation includes the following steps:

- Loading images.

- Cropping images (optional): for the images containing much noise.

- Converting to binary images: in order to make the image recognizable by the analyzing function in the software, the images need to be converted into binary images (black and white).

When sequential binary images are prepared, the analysis is ready to be carried out. The analysis procedures are:

- Setting measurements: Different measurements such as area, center of mass, circularity etc. can be selected.

- Analyzing particles: Measuring ranges can be defined to make the analysis more efficient.

When the analysis is finished, a result file is returned. The result file is a matrix which is loaded into MATLAB, and a script with proper sequential procedures was implemented to find parameters such as diameter, velocity and impinging angle.

4.3 Uncertainty Analysis

4.3.1 Overview of the Uncertainty Sources and Combined Uncertainty Models

The random and systematic experimental uncertainties from the experiment and the propagation to different dimensionless numbers are described in this section, and the uncertainty analysis refers to Wheeler & Ganji (2004).

The fundamental quantities obtained from the measurement are the diameter and the velocity of the droplets. Due to the experimental conditions, there are random uncertainties and systematic uncertainties. Different sources of uncertainties are listed in the following text, and the uncertainties can propagate into the fundamental parameters (diameter and velocity) and dimensionless numbers.

1. Frame rate of the camera (systematic)

2. Gauge (systematic)

3. Gauge measurement (systematic)

4. Measurement of the tilted angle of the camera (random)

5. Image segmentation (systematic)

6. Threshold judgment in the image processing (random)

7. Oscillation of droplet and inhomogeneous light condition (random)

8. Variation of the physical properties (systematic)

In these uncertainties, some of the information for the systematic standard uncertainties was not explicitly given such as the manufacture uncertainty of the gauge, and the random standard uncertainties evaluations were sometimes limited by the measurements, for instance, the degree of freedom or samples could not be increased if the velocity of a droplet was high. However, the maximum uncertainties (or approximately maximum) from different sources were always predictable based on the methods and results from the measurement. If it was assumed that all the estimated uncertainties were approximately the maximum uncertainties, and they were obtained with 95% confidence level. The combined uncertainties in diameter and velocity could be evaluated using an uncertainty model

$$U = [(B_x)^2 + (P_x)^2]^{\frac{1}{2}} \tag{4.1}$$

where B_x and P_x were the systematic standard uncertainty and the random uncertainty, respectively, and they could be calculated as

$$B_x = \left(\sum_{i=1}^{n} \omega^2_{\text{syst}-\text{n}} \right)^{\frac{1}{2}} \tag{4.2}$$

$$P_x = \left(\sum_{i=1}^{n} \omega^2_{\text{rand}-\text{n}} \right)^{\frac{1}{2}} \tag{4.3}$$

where $\omega_{\text{syst}-\text{n}}$ and $\omega_{\text{syst}-\text{n}}$ denoted the systematic uncertainty and the random uncertainty from individual source number "n".

The sources of uncertainties are described and analyzed in the following section.

4.3.2 Sources of Uncertainties

Uncertainty 1: Frame Rate of the Camera

The manual-designated frame rate, frames per second (fps), is 9216.59 fps, which is obtained from dividing the amount of frames over a time more than 1 second. According to the physical limitation, a decimal frame does not exist. Hence, it can give a possible uncertainty in the time step between two neighboring frames. The uncertainty is expressed

$$\omega_{\text{t}} = \pm \left(\frac{1}{9216} - \frac{1}{9217} \right) \text{ s} = \pm 1.18 \times 10^{-8} \text{ s.} \tag{4.4}$$

Uncertainty 2: Gauge

Due to the imperfect manufacture, the diameters of the standard measurements (gauges) may vary from their reported values. Two types of gauges, a tungsten thread of $300\,\mu\text{m}$, and a Hamilton needle of $210\,\mu\text{m}$ were used. A vernier caliper was used to calibrate the gauges, and approximately 1% uncertainty was found with regard to the standard sizes. Here it was assumed that the uncertainty level was 1% of the diameter, and thus,

$$\omega_{\text{g}} = \pm \frac{300 + 210}{2} \times 1\% = 2.55 \ \mu\text{m.} \tag{4.5}$$

The uncertainty of the gauge corresponded to the measurement of a $255\,\mu\text{m}$ object size which was equivalent to the mean gauge size, and as the gauge was used for scaling the measurements, any gauge-related uncertainty would be proportionally introduced into the measurements. It means that this uncertainty will be linearly reduced for measuring smaller size objects (compared to the gauge size), and amplified for measuring larger size
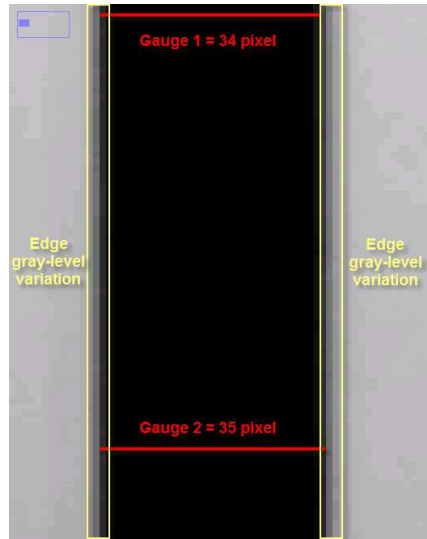
Figure 4.1: Gauge measurement uncertainty due to gray-level on the edge - observation magnified 8 times of the original magnification.

objects. The uncertainty from this source could be reduced by using a larger (while still within the observation area) and more accurately-made standard measurement.

Uncertainty 3: Gauge Measurement

The gauges were vertically set against the horizontal plane, and there were uncertainties in the gauge measurement due to the gray-level variation shown in Figure 4.1. The variation of the gray-level leads to an assumed uncertainty of ± 1 pixel (≈ 6 μm), and so the uncertainty is expressed

$$\omega_{\mathrm{gm}} = 6 \ \mu\mathrm{m}. \tag{4.6}$$

The uncertainty of the gray-level edge always existed as described, and it is defined as a systematic uncertainty.

Similar to the former uncertainty, this uncertainty is also gauge-related, and it is proportional to the object size. The uncertainty from this source can be reduced by using a larger and more accurately-made standard measurement, and besides, a better focus of the gauge will also reduce this uncertainty as the gray-level variation can be reduced with a better focus.
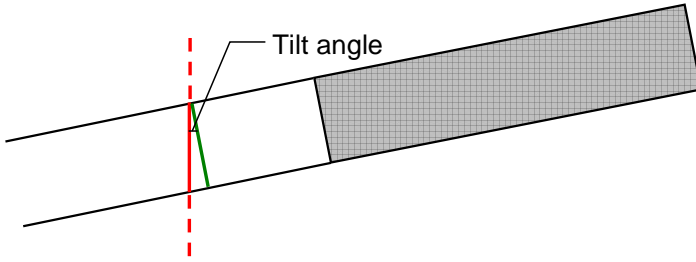
Figure 4.2: Displacement measurement by a tilted camera.

Uncertaity 4: Measurement of the Tilted Angle of the Camera

Figure 4.2 shows the real path of a falling droplet (the red line) and the path read by the camera (the green line), and the angle between these two paths are the tilt angle of the camera. An uncertainty exists in the displacement measurement if the tilt angle is not measured accurately. The tilt angle was measured by trigonometric calculations. The uncertainty from the tilt angle was not considered in the diameter measurement due to the sphere-symmetry which made the measurement of the diameter the same from different angles.

The maximum angle uncertainty is assumed to be $\pm 0.5°$. Based on the approximate maximum displacement ($1000\,\mu$m) that a droplet can cover between two frames, the uncertainty in the measurement of the displacement due to the angle uncertainty is

$$\omega_{\,\text{am}} = 0.59 \ \mu\text{m}. \tag{4.7}$$

Uncertainty 5: Image Segmentation

The camera resolves the physical objects in the pictures using pixels which are the most fundamental units in an image. In our case, the resolution was kept at 576×288 pixels, and the equivalent length for 1 pixel is approximately $5.9\,\mu$m.

The uncertainty comes when the reality meets the ideal pixel-imaging where the length and area of any objects have to be interpreted as integral pixels. When converting an image shown in Figure 4.3 into a binary picture, it has to be decided whether the edge pixel, the grid marked with bold line, should be recognized as a part of the object (a black pixel) or as a part of the background (a white pixel). The process for recognizing the edge of an object in an image is called the image segmentation. The algorithms
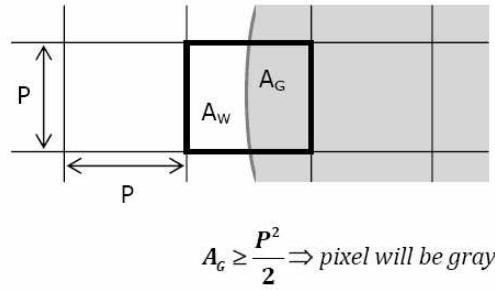
Figure 4.3: Image segmentation. (Figure from Sevault (2008))

for image segmentation are many and complex. For simplicity, a rounding-off method (García-Tabarés et al. 2002) was used here for analyzing the uncertainty introduced by the segmentation. The principle of the method is shown in Figure 4.3: if more than 50% of an edge-grid is covered by a an object, the segmentation will count the whole edge-grid into the object, otherwise, the edge-grid will be excluded from the object.

Displacement measurement:
The displacement measurement is a one-dimensional analysis as a displacement is decided by the coordinates of the mass center in two images. It is obvious that the maximum uncertainty for an end of a line from its real position to its rounded integral-pixel position is 0.5 pixel when the end lies in the middle of a pixel grid, and thus the maximum for a length of a line the uncertainty is 1 pixel which is approximately $6\,\mu$m. Hence the uncertainty of the displacement measurement due to the segmentation is

$$\omega_{\text{disp\_seg}} = 6 \ \mu\text{m}. \tag{4.8}$$

Diameter measurement:
For measuring the diameter of a droplet, it is either possible to use the one-dimensional analysis or to use two-dimensional analysis in which the diameter is calculated using the equivalent diameter

$$D_{\text{efficient}} = \sqrt{\frac{4 \cdot \text{Area}}{\pi}} \tag{4.9}$$

where $D_{\text{efficient}}$ and Area denotet the equivalent diameter and intersection area of the droplet, respectively. It has been proven that the equivalent diameter can give less uncertainty than the one-dimensional measurement (García-Tabarés et al. 2002). García-Tabarés et al. (2002) only gave the predicted uncertainty of the diameter ranging between 200 and 300 pixels.
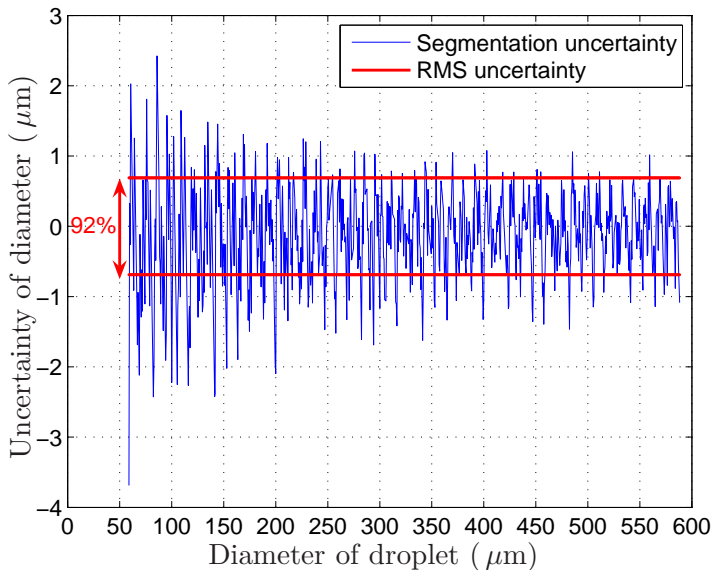
Figure 4.4: The uncertainty of the diameter measurement due to the segmentation (investigated using 2D analysis)

For most of our cases, the diameter ranges between 10 and 100 pixels corresponding to 60-600 μm, and a simulation, which utilized the rounding-off principle for the edge-grids, was carried out to investigate the uncertainty.

The simulation result is shown in Figure 4.4. It shows a random pattern of the uncertainty, and the absolute value is between 0 and $3\,\mu$m. The figure shows that the uncertainty seldom goes to the extreme value $(3\ \mu m)$, and therefore the extreme value cannot be used to give a reasonable evaluation. In the simulation, 92% of the uncertainties were below the uncertainty root mean square (RMS) value, 0.69 μm, and thus the root mean value was used to evaluate this uncertainty. Compared to the displacement uncertainty $(6\,\mu$m), the lower diameter uncertainty also proved that the two-dimensional analysis for the diameter measurement is more efficient ($\approx$ 9 times lower uncertainty) than the one-dimensional analysis.

Hence, the uncertainty of the diameter measurement due to the segmentation is

$$\omega_{\text{diam\_seg}} = \pm 0.69 \ \mu\text{m}. \tag{4.10}$$

Uncertainty 6: Threshold Judgment in the Image Processing

For image processing, all images need to be converted to binary images. More specifically, an image containing multiple gray-scale levels is to be

converted into two levels (black and white), and the boundary is denoted as the threshold.

An uncertainty can be introduced if the threshold of an image is not precisely judged, the threshold level can be either underestimated or over-estimated such as shown in Figure 4.5. As can be seen from the figure, if the threshold is under the precise level, the image processing filters some necessary information of the droplet, and thus the area (red part) of the droplet is smaller than the real value. On the contrary, if the threshold is over the level, the image processing includes noise from the background, and thus the area of the droplet is larger than the real value. In most of the measurements in the present work, the auto-calculated threshold (by ImageJ) of the first image in a sequential images was used, and this was based on the ideal condition that the calculated value was reliable and the threshold condition was invariant over the impact duration. However, in the real condition, there were uncertainties both in the calculated value and the threshold condition due to the fact that background noise might
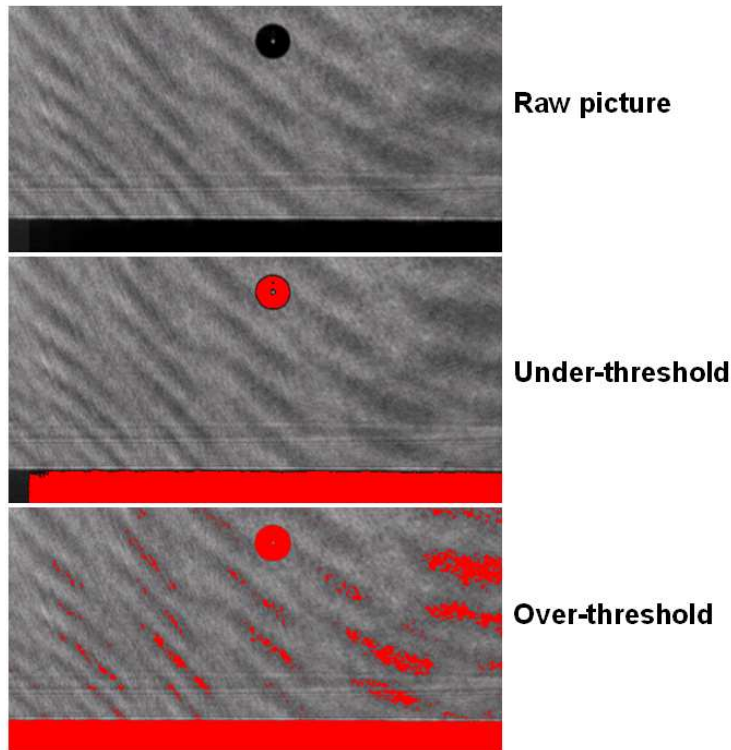
Figure 4.5: The uncertainty from threshold judgment
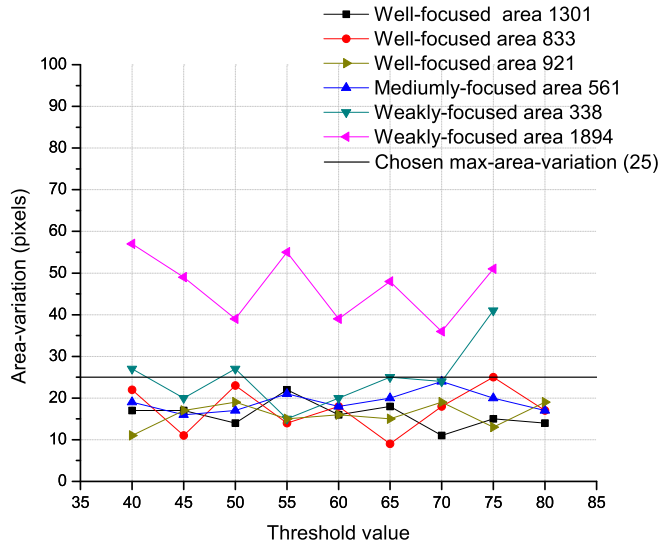
Figure 4.6: Sensitivity analysis for the threshold judgment

deviate the threshold from its real value. A sensitivity analysis was carried out to show how the threshold judgment can affect the area measurement.

6 typical cases, which included well-focused, mediumly focused and weakly-focused droplets of different areas, were investigated. For each case, the area variations (absolute value) between different threshold values and the calculated value are given in Figure 4.6. The figure shows that the area variations randomly change, and except one case, which is the weakly-focused droplet with relatively large area (1894 pixels), most of the maximum area-variations are below 25 pixels. The exceptional case was very rare in the experiments, as large droplets with slow velocities were more easily located with good focuses. Thus, it can be assumed that the maximum uncertainty in the area measurements due to thresholding is ± 25.

In the present work, the droplet diameter approximately varied between 0.06 and 0.6 mm, and the uncertainty in the diameter measurement due to the threshold judgment is shown in Figure 4.7. It is shown that the uncertainty is dependent on droplet diameter. This uncertainty is defined as a random uncertainty since it can be reduced by measuring the area with several thresholds around the most ideal threshold condition. The uncertainty from this source can be reduced by using a light source that gives a more homogeneous light condition and by focusing of droplets better.
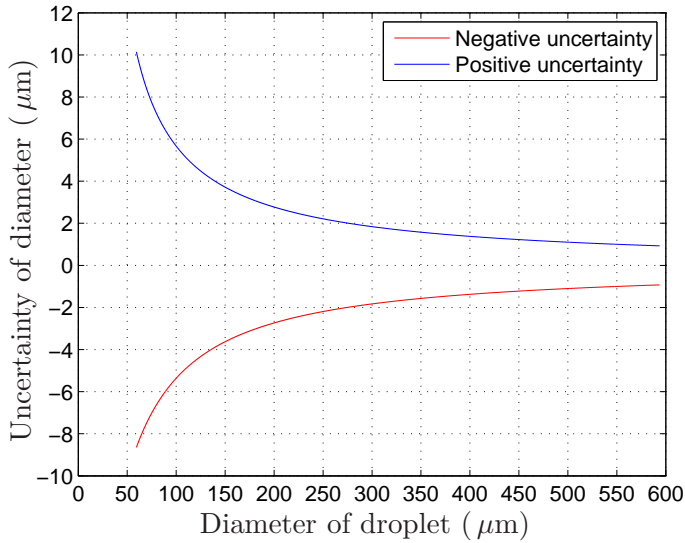
Figure 4.7: The uncertainty of diameter measurement due to the the threshold judgment

Uncertainty 7: Oscillation of Droplet

When measuring a droplet, an uncertainty may be introduced into the area measurement if the droplet oscillates and deforms. The reason is that a droplet with a different shape has a different area.

Due to the image segmentation, the edge of a droplet is rugged (this can be seen by zooming-in the image), and thus the perimeter is longer than it should be. The circularity

$$\text{Circularity} = 4 \cdot \pi \, (\text{area}/\text{perimeter}^2) \tag{4.11}$$

is therefore lower than 1 even for a perfect circle, and a droplet can be assumed to be a perfect circle if the the circularity is around or above 0.9. In our case, the circularities for most of the droplets were kept around 0.9, and this means that in most of the cases droplets remain well in circular shape.

The uncertainty from droplet oscillation is caused by the area variations of a droplet during its falling process as the shape of the droplet varies. The maximum uncertainty in most of the cases is around 2% of the measured area, and this value is assumed as the uncertainty for droplet oscillation. This uncertainty can be reduced if multiple samples are measured, and thus it is defined as a random error. The uncertainty is diameter-dependent, and the approximate maximum value of the uncertainty is shown in Figure 4.8.
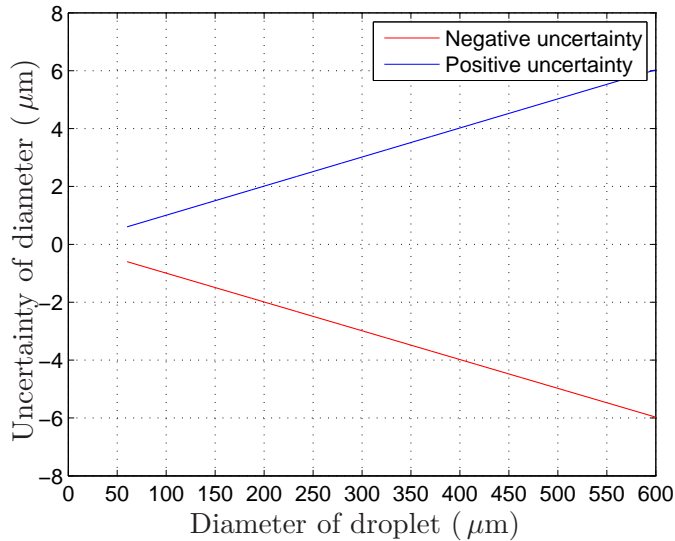
Figure 4.8: The uncertainty of the diameter measurement due to the oscillation of a droplet

The uncertainty from this source can be reduced by selecting impinging droplets with more circular shape.

Uncertainty 8: Uncertainties in the Physical Properties

Physical properties of the fluids were used in the calculation of the dimensionless groups such as the Reynolds, Froude, Ohnesorge and Weber numbers. The property uncertainties originate from two origins:

- Origin 1: Uncertainty from the temperature variation in the experiments.

- Origin 2: Uncertainty from the property-measurements such material (composition/pollution), measuring methods etc.

The temperature variation in the present work is maximum $\pm 3°$C.

The property uncertainties due to the temperature variation are evaluated using HYSYS. The maximum uncertainties for properties are used, and the uncertainties are assumed to be symmetrical below and above the specified temperature.

The uncertainty from the measurements can be obtained from the literature or comparing the values between different sources shown in Table 3.6.

Table 4.1: Uncertainty of the physical properties from two places.

Fluid	$(\frac{\omega_\rho}{\rho})_1$	$(\frac{\omega_\rho}{\rho})_2$	$(\frac{\omega_\rho}{\rho})$	$(\frac{\omega_\mu}{\mu})_1$	$(\frac{\omega_\mu}{\mu})_2$	$(\frac{\omega_\mu}{\mu})$	$(\frac{\omega_\sigma}{\sigma})_1$	$(\frac{\omega_\sigma}{\sigma})_2$	$(\frac{\omega_\sigma}{\sigma})$
Distilled water	0.3%	0.3%	0.4%	7.23%	0.3%	7.24%	0.72%	0.1%	0.73%
Technical ethanol	0.36%	1%	1.06%	5.59%	5%	7.5%	1.13%	3%	3.2%
n-pentane	0.53%	0.08%	0.54%	2.52%	1.0%	2.7%	3.15%	1.2%	3.37%
Methanol	0.39%	0.01%	0.39%	4.37%	0.37%	4.39%	1.62%	1.9%	2.5%
1-propanol	0.39%	0.8%	0.89%	7.60%	2%	7.86%	1.48%	2%	2.49%

The two uncertainties for the physical properties are shown in Table 4.1, where $(\frac{\omega_{\rho,\mu,\sigma}}{\rho,\mu,\sigma})_1$ denotes the property uncertainties from the Origin 1, and $(\frac{\omega_{\rho,\mu,\sigma}}{\rho,\mu,\sigma})_2$ denotes the property uncertainties from Origin 2.

The combined uncertainty, $(\frac{\omega_{\rho,\mu,\sigma}}{\rho,\mu,\sigma})$, is calculated by using the U in Eq. (4.1), and it is used in the calculations of the uncertainty propagations into the dimensionless parameters.

4.3.3 Combined Uncertainty Evaluations for the Fundamental Parameters

This section describes the method for evaluating the uncertainties in the fundamental parameters parameters (diameter and velocity) which are irrelevant to the physical properties. The uncertainties of the fundamental parameters are evaluated using the uncertainty sources described in Section 4.3.2.

It must be pointed out that the uncertainties evaluated in this section are based on general diameter and velocity ranges in the experiment, and the specific uncertainties of the diameter and velocity are presented in Chapter 5.

Diameter

The expression for the diameter measurement is:

$$D = D_m \cdot f, \tag{4.12}$$

where D_m and f are the diameter measurement and the scaling factor. If there are no gauge-related uncertainties (ω_{g} and ω_{gm}), the scaling factor, f, equals 1. Thus, ω_{g} and ω_{gm} are used to evaluate the combined uncertainty of the scaling factor.

The uncertainties that propagate into the diameter measurement (D_m) are from: The segmentation of the diameter measurement ($\omega_{\mathrm{diam\_seg}}$), the

judgment of threshold for diameter measurement (ω_{tj}), and the oscillation of the droplet (ω_{os}). Among those uncertainties, $\omega_{\mathrm{diam\_seg}}$ is a systematic uncertainty, while ω_{tj} and ω_{os} are random uncertainties.

The uncertainties of the gauge (ω_{g}) and the gauge measurement (ω_{gm}) propagate into the scaling factor.

The uncertainty propagated into the diameter is described by Eq. (4.13)

$$\frac{\omega_D}{D} = \left\{ \left(\frac{\omega_{Dm}}{D_m} \right)^2 + \left(\frac{\omega_f}{f} \right)^2 \right\}^{\frac{1}{2}}. \tag{4.13}$$

The uncertainty (ω_D) is derived as

$$\omega_D = \left\{ D^2 \cdot \left(\frac{\omega_{Dm}}{D_m} \right)^2 + D^2 \cdot \left(\frac{\omega_f}{f} \right)^2 \right\}^{\frac{1}{2}}, \tag{4.14}$$

and by using the relation $D \approx D_m >> \omega_{Dm}$, this equation can be readily simplified to

$$\omega_D = \left\{ (\omega_{Dm})^2 + D^2 \cdot \left(\frac{\omega_f}{f} \right)^2 \right\}^{\frac{1}{2}}. \tag{4.15}$$

The uncertainty model, Eq. (4.1), is used to calculate

$$\omega_{Dm} = \sqrt{(\omega_{\mathrm{diam\_seg}})^2 + (\omega_{\mathrm{tj}})^2 + (\omega_{\mathrm{os}})^2} \tag{4.16}$$

and

$$\omega_f = \sqrt{\left(\left(\frac{\omega_{\mathrm{g}}}{255} \right)^2 + \left(\frac{\omega_{\mathrm{gm}}}{255} \right)^2 \right)} \tag{4.17}$$

The uncertainty of the diameter measurement is dependent on the diameter, and Figure 4.9(a) shows the estimated uncertainty of diameter measurement, and Figure 4.9(b) shows that the value of $\frac{\omega_D}{D}$ varies in a narrow from 2.75% to 3.01%.

Velocity

The equation for the velocity measurement is

$$V = \frac{L}{t} \tag{4.18}$$

where V, L, t denote velocity, displacement and time step, respectively.

Similar to the diameter measurement,

$$L = L_m \cdot f, \tag{4.19}$$
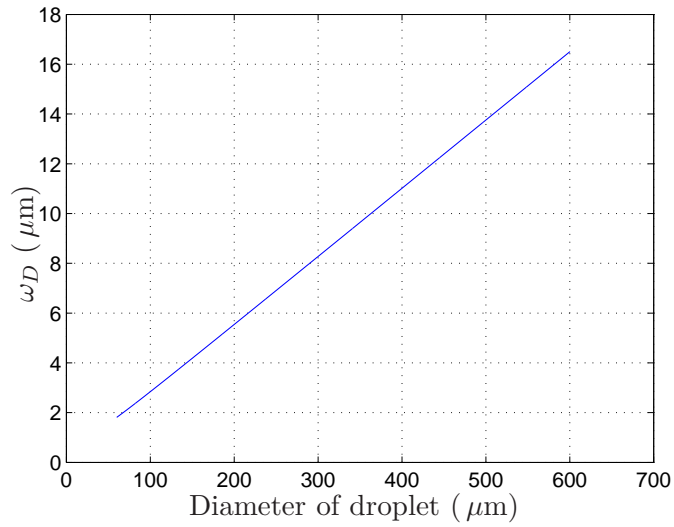
(a) Diameter uncertainty vs. diameter.
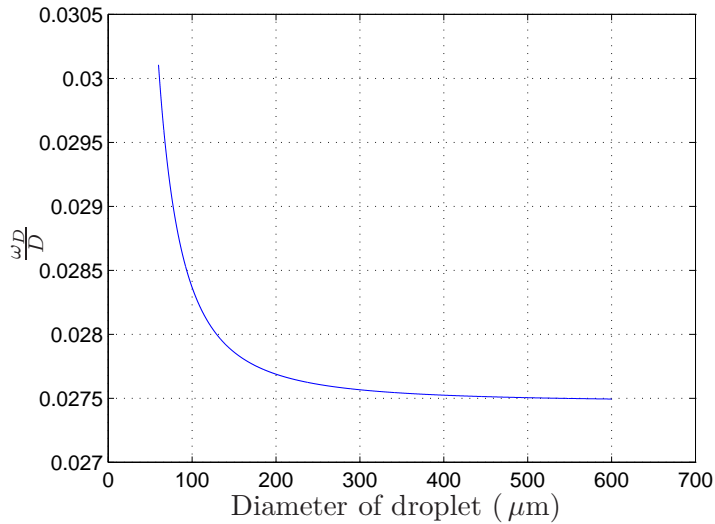
(b) Relative uncertainty of diameter.

Figure 4.9: Uncertainty of droplet diameter measurement.

where L_m is the displacement measurement and f is the scaling factor.

The uncertainty evaluation for the displacement is the same as for the evaluation for diameter. The uncertainties that propagate into the displacement measurement (L_m) are from: the tilt angle measurement (ω_{am}) and the segmentation of the displacement measurement (ω_{disp_seg}). ω_{disp_seg} is a systematic uncertainty, while ω_{am} is a random uncertainty.

The uncertainties of the gauge (ω_g) and the gauge measurement (ω_{gm}) propagate into the scaling factor uncertainty.

The uncertainty propagates into the velocity has a relation with the uncertainty of displacement and the uncertainty of the time step, and the relation is

$$\frac{\omega_V}{V} = \left\{ \left(\frac{\omega_{disp}}{V \cdot t} \right)^2 + \left(\frac{\omega_t}{t} \right)^2 \right\}^{\frac{1}{2}}. \qquad (4.20)$$

Figure 4.10(a) shows that the uncertainty of velocity is dependent on the velocity of the falling droplet, the lower limit of the velocity is set to 0.1 m/s which corresponds to the lowest velocity in this work. Figure 4.10(b) indicates that the relative uncertainty ($\frac{\omega_V}{V}$) approaches a very high value which is around 55% as the velocity gets close to 0.1. The reason is that, due to the uncertainty assumptions, the displacement for calculating the velocity approaches the resolution limit in this case, and thus, the velocity is comparable to the velocity uncertainty.

In the experiments, the minimum velocity that can be reached is around $0.1\,\mathrm{m/s}$, in the case of low energy coalescence. Even though the relative uncertainty of velocity ($\frac{\omega_V}{V}$) is high around 55%, the absolute uncertaity (ω_V) is very small around $0.055\,\mathrm{m/s}$. So, generally, this does not affect much the overall measuring accuracy.

For most of the data with velocities above $1\,\mathrm{m/s}$, the relative uncertainty decreases to lower than approximately 5% and finally reaches a stable level around 2.6%.
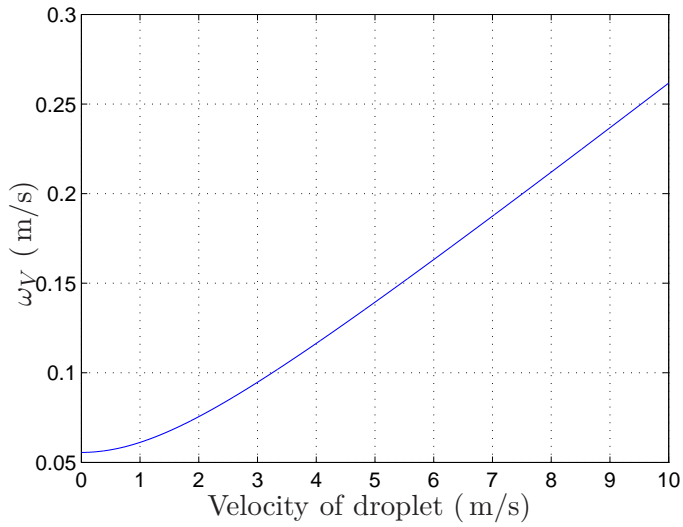
(a) Velocity uncertainty vs. velocity.
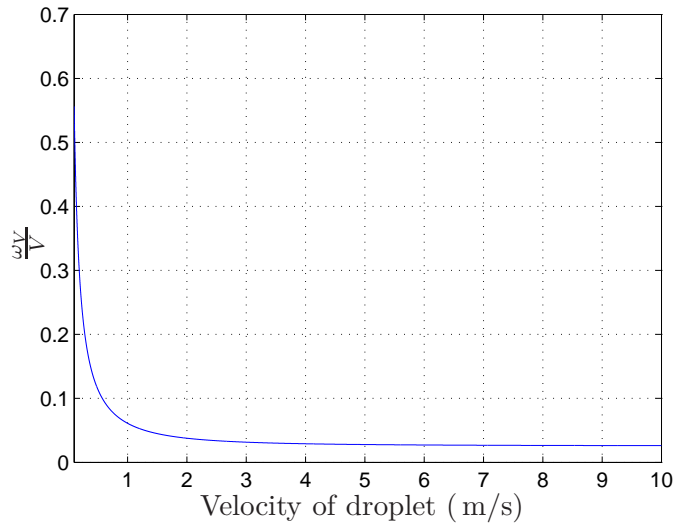
(b) Relative uncertainty of velocity.

Figure 4.10: Uncertainty of droplet velocity measurement.

4.3.4 Uncertainty Evaluations for Dimensionless Parameters

The uncertainties of the fundamental parameters, as well as the physical properties, propagate into the dimensionless parameters such as the Reynolds, Weber, Ohnesorge and Froude number.

This section describes the method for evaluating the uncertainties in the dimensionless parameters. The uncertainties evaluated in this section are based on general diameter and velocity ranges in the experiment, and the specific uncertainties of the dimesionless parameters are presented in Chapter 6.

Reynolds Number

The Reynolds number is expressed by Eq. (2.1). The uncertainty of Reynolds number (ω_{Re}) can be expressed as

$$\frac{\omega_{\text{Re}}}{\text{Re}} = \left\{ \left(\frac{\omega_\rho}{\rho}\right)^2 + \left(\frac{\omega_D}{D}\right)^2 + \left(\frac{\omega_V}{V}\right)^2 + \left(\frac{\omega_\mu}{\mu}\right)^2 \right\}^{\frac{1}{2}}. \tag{4.21}$$

The uncertainty of Reynolds number is dependent on both the diameter and the velocity of the droplet. Besides, the uncertainties of the physical properties have to be considered. In our case, most of the velocities are in a range of 1-10 m/s, and thus 10 velocity samples (1, 2, 3, $\cdots$, 10 m/s) were taken to show the uncertainty of Reynolds number versus the diameter and the Reynolds number.

As can be seen from Figure 4.11(a), the uncertainties increase as the Reynolds number increases. For a given fluid, the slope of the uncertainty decreases as the velocity increases, and the slope presents slightly non-linear trend when the Reynolds number is low.

The relative uncertainty of Reynolds number ($\frac{\omega_{\text{Re}}}{\text{Re}}$) is shown in Figure 4.11(b), and the variation limits are shown in Eq. (4.22) for each fluid. Higher velocity corresponds to lower uncertainty.

$$\text{Distilled water}: 8.18\% \leq \frac{\omega_{\text{Re}}}{\text{Re}} \leq 9.95\%$$

$$\text{Technical ethanol}: 8.47\% \leq \frac{\omega_{\text{Re}}}{\text{Re}} \leq 10.19\%$$

$$\text{n} - \text{Pentane}: 4.69\% \leq \frac{\omega_{\text{Re}}}{\text{Re}} \leq 7.35\% \tag{4.22}$$

$$\text{Methanol}: 5.82\% \leq \frac{\omega_{\text{Re}}}{\text{Re}} \leq 8.12\%$$

$$1 - \text{Propanol}: 8.77\% \leq \frac{\omega_{\text{Re}}}{\text{Re}} \leq 10.44\%$$
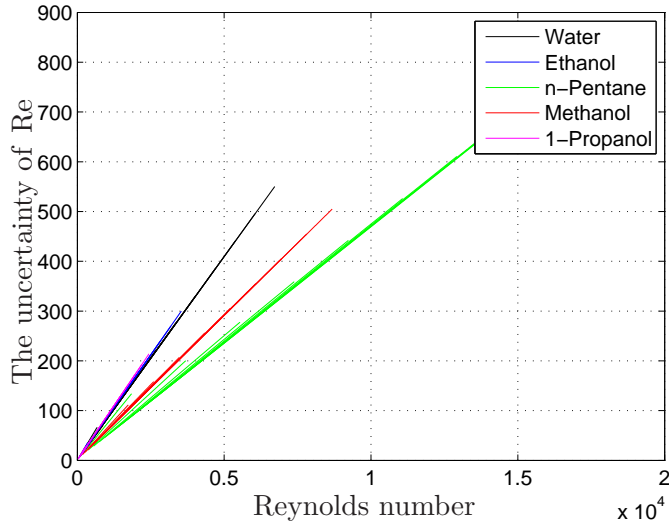
(a) Reynolds number uncertainty vs. Reynolds number.
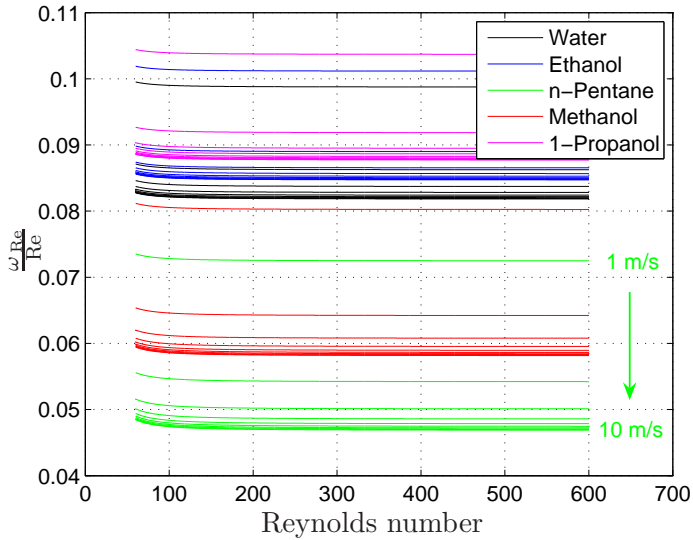
(b) Relative uncertainty of Reynolds number.

Figure 4.11: Uncertainty of Reynolds number of droplet. The uncertainty is velocity-dependent. For each fluid, 10 velocity samples (1-10 m/s) are plotted in the figure, and higher velocity corresponds to lower relative uncertainty as shown for the relative uncertainty of n-pentane (green).

Ohnesorge Number

The Ohnesorge number is expressed by Eq. (2.2). The uncertainty of Ohnesorge number (ω_{Oh}) can be expressed as

$$\frac{\omega_{\text{Oh}}}{\text{Oh}} = \left\{ \left(\frac{\omega_\mu}{\mu}\right)^2 + \left(-\frac{1}{2}\cdot\frac{\omega_\rho}{\rho}\right)^2 + \left(-\frac{1}{2}\cdot\frac{\omega_\sigma}{\sigma}\right)^2 + \left(-\frac{1}{2}\cdot\frac{\omega_D}{D}\right)^2 \right\}^{\frac{1}{2}}. \quad (4.23)$$

The uncertainty of Ohnesorge number is dependent on the diameter of the droplet besides the physical properties. The relative uncertainties of Oh for five fluids are shown in Figure 4.12. As can be seen, the relative uncertainties for different fluids tend towards constants. The relative uncertainty ranges for different fluids are shown in equation (4.24) for each fluid, and the ranges are all very small.
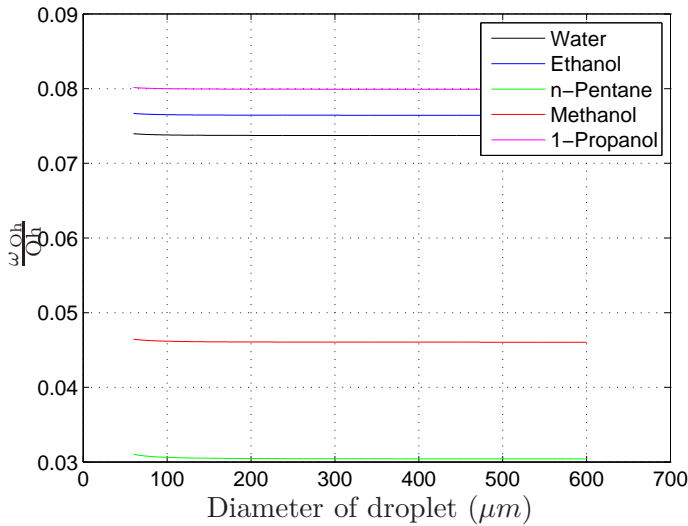
Figure 4.12: Relative uncertainty of Ohnesorge number ($\frac{\omega_{\text{Oh}}}{\text{Oh}}$) versus diameter of droplet.

$$\text{Distilled water}: 7.37\% \leq \frac{\omega_{\text{Oh}}}{\text{Oh}} \leq 7.40\%$$

$$\text{Technical ethanol}: 7.64\% \leq \frac{\omega_{\text{Oh}}}{\text{Oh}} \leq 7.67\%$$

$$\text{n} - \text{Pentane}: 3.04\% \leq \frac{\omega_{\text{Oh}}}{\text{Oh}} \leq 3.10\% \qquad (4.24)$$

$$\text{Methanol}: 4.60\% \leq \frac{\omega_{\text{Oh}}}{\text{Oh}} \leq 4.65\%$$

$$1 - \text{Propanol}: 7.99\% \leq \frac{\omega_{\text{Oh}}}{\text{Oh}} \leq 8.02\%$$

Weber Number

The Weber number is expressed by Eq. (2.3). The uncertainty of Weber number (ω_{We}) can be expressed as

$$\frac{\omega_{\text{We}}}{\text{We}} = \left\{ \left(\frac{\omega_\rho}{\rho} \right)^2 + \left(\frac{\omega_D}{D} \right)^2 + \left(2 \cdot \frac{\omega_V}{V} \right)^2 + \left(\frac{\omega_\sigma}{\sigma} \right)^2 \right\}^{\frac{1}{2}}. \qquad (4.25)$$

The uncertainty of Weber number is dependent on both the diameter and the velocity of the droplet besides the physical properties. The relative uncertainties of We for five fluids are shown in Figure 4.13, where 10 velocity samples were taken for each fluid.

As can be seen, the relative uncertainties for different fluids vary with the velocities, and higher velocity corresponds to lower relative uncertainty. Curves for different fluids are at a certain velocity are almost overlapping, and this indicates that the fluid properties are not the main source to the uncertainty due to small variations in the densities and surface tensions.

The figure shows that the relative uncertainty varies between 5.98% and 12.63% depending on different velocities, and higher velocity corresponds to lower relative uncertainty. The relative uncertainties for all fluids at a certain velocity are very close to a constant.

Froude number

The Froude number is expressed by Eq. (2.5). The uncertainty of Froude number (ω_{Fr}) can be expressed as

$$\frac{\omega_{\text{Fr}}}{\text{Fr}} = \left\{ \left(\frac{\omega_V}{V} \right)^2 + \left(-\frac{1}{2} \cdot \frac{\omega_D}{D} \right)^2 \right\}^{\frac{1}{2}}. \qquad (4.26)$$

The uncertainty of Froude number is dependent on the diameter and the velocity of droplet. The uncertainty of the Froude number for each velocity
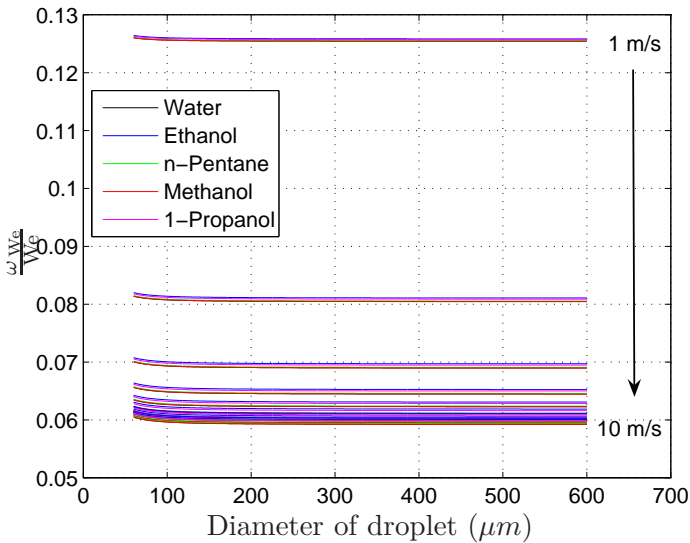
Figure 4.13: Relative uncertainty of Weber number ($\frac{\omega_{\text{We}}}{\text{We}}$) versus diameter of droplet. The uncertainty is velocity-dependent. For each fluid, 10 velocity samples (1-10 m/s) are plotted in the figure, and higher velocity corresponds to lower relative uncertainty.

is shown in Figure 4.14, and higher velocity corresponds to lower relative uncertainty.

As can be seen, the relative uncertainty of Fr varies between 2.96% and 6.30% depending on the size and the velocity of droplet. The uncertainty of Fr is independent of the physical properties as the properties are not included in the calculation of the Froude number. The figure shows that, for a certain velocity, the relative uncertainty is nearly a constant.

Capillary number

The Capillary number is expressed by Eq. (2.6). The uncertainty of Capillary number (ω_{Ca}) can be expressed as

$$\frac{\omega_{\text{Ca}}}{\text{Ca}} = \left\{ \left(\frac{\omega_{\mu}}{\mu} \right)^2 + \left(-\frac{\omega_{\sigma}}{\sigma} \right)^2 + \left(\frac{\omega_V}{V} \right)^2 \right\}^{\frac{1}{2}}. \tag{4.27}$$

The uncertainty of Capillary number depends on the velocity of the droplet besides the physical properties. The relative uncertainties of the Capillary number for five fluids are shown in Figure 4.15.
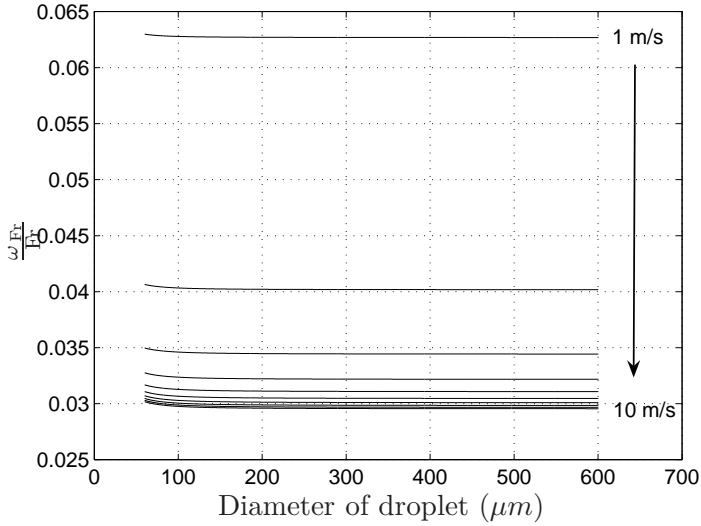
Figure 4.14: Relative uncertainty of Froude number ($\frac{\omega_{\mathrm{Fr}}}{\mathrm{Fr}}$) versus diameter of droplet. The uncertainty is velocity-dependent but independent of fluid (physical properties). 10 velocity samples (1-10 m/s) are plotted in the figure, and higher velocity corresponds to lower relative uncertainty.
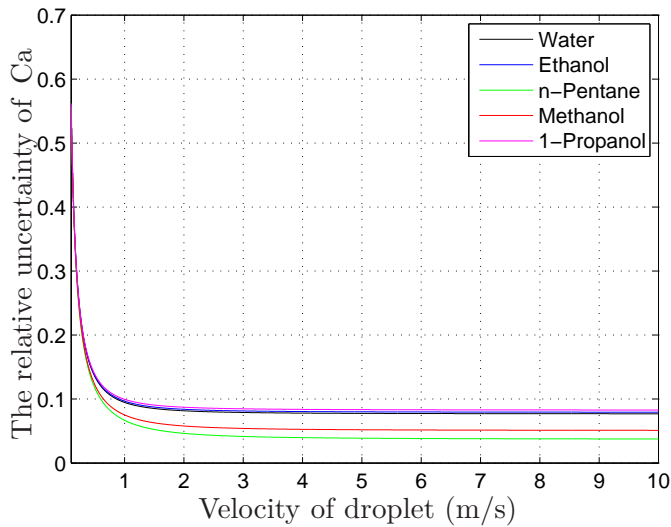
Figure 4.15: Relative uncertainty of Capillary number ($\frac{\omega_{\mathrm{Ca}}}{\mathrm{Ca}}$) versus velocity of droplet.

Figure 4.15 is very similar to Figure 4.10(b), and this is due to the fact that the Capillary number is velocity-dependent. Similar to $\frac{\omega_V}{V}$, $\frac{\omega_{Ca}}{Ca}$ approaches a very high value which is around 55% as the velocity gets close to 0.1. The reason is that, due to the uncertainty assumptions, the displacement for calculating the velocity approaches the resolution limit in this case, and thus, the velocity is comparable to the velocity uncertainty.

For most of the data with velocities above $1\,\text{m/s}$, the uncertainty ration decreases to less than 10%.

4.4 Summary of the Chapter

- This Chapter describes the image-processing method in a general sense. The method enables image-processing to be carried out in a more accurate and efficient way than manual processing. The image-processing software was used to obtain the fundamental information of droplets such as the area, coordinates, circularity etc., and a MAT-LAB script was written to process the fundamental information to calculate the fundamental parameters, i.e. diameter and velocity.

- The uncertainty propagations into the fundamental parameters (diameter and velocity) and the dimensionless parameters (Re, Oh, We, Fr and Ca) are analyzed by using general diameter and velocity ranges. The general uncertainties for the parameters are:

  - Diameter: around 3%.
  - Velocity: for most of the cases ($V > 1\,\text{m/s}$), within 5%.
  - Re: in most of the cases within 10%.
  - Oh: in most of the cases within 8%.
  - We: in most of the cases within 13%.
  - Fr: in most of the cases within 6.5%.
  - Ca: in most of the cases within 10%

  Generally, the uncertainties are below 10%, and one advantage is that the uncertainty is reduced if the Froude number is used to characterize the thresholds.

Chapter 5

Experimental Observations and Results

5.1 Introduction

This chapter gives an overview of observations and results from the experiments of droplets impacting on a deep liquid pool. In general, the regimes are arranged according to the impact energy level from high to low, and the impact energy level can be indicated by the combination of diameter and velocity. Figure 5.1(a) shows the distribution of different regimes from the technical ethanol experiment, and a schematic drawing of the typical distributions of the regimes is illustrated in Figure 5.1(b).

In each section, observations of the regime are illustrated by using sequential images from the experiment, and the experimental results are described and presented according to the experimental fluids.

All of the pictures shown in this chapter are with the resolution of 576×288 pixels, and the images are cropped in order to illustrate more clearly the observations near the impinging location. The frame rate at this resolution is 9216 fps, and thus the interval between two neighboring images is about $0.1\,\mathrm{ms}$. The duration of the evolution process is different for different phenomena. For showing processes with longer evolution time, a part of the images with insignificant observations may be omitted in sequential images. The exposure time varies from 5-$10\,\mu\mathrm{s}$.

(a) Different regimes of technical ethanol.
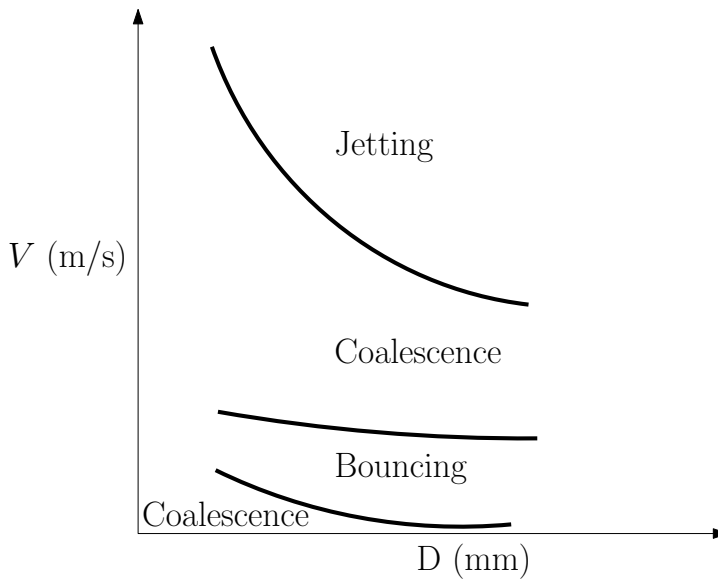
(b) Typical distribution of regimes.

Figure 5.1: Distribution of different regimes.

5.2 Observations and Results of Jetting

5.2.1 Observations from Jetting

Depending on the dynamic parameters (diameter and velocity), there are different types of observations in jetting. The central jet is used to characterize the jetting, however sometimes the central jet can barely be observed as it is blocked by the swelling waves around the impingement location. When the central jet is not observed, the secondary droplets generated from the central jet are used as the criterion for jetting. Instead of the swelling wave, a crown-like wave is also observed in jetting. The following sections show different types of jetting observed in the experiments.

Jetting Type 1: Observation of Swelling Wave, Secondary Droplet Ejected from Central Jet & Without Observation of Central Jet

In this type of jetting, the observation of the central jet is hindered by the swelling wave, and a crown-like wave is not observed. Figure 5.2 shows the observation of this type of jetting with several characteristic steps:

- Row 1: The droplet falls down and impacts nearly vertically onto the surface of the deep liquid pool, and a swelling wave is raised. Due to the vertical impact, the shape of the swelling wave is symmetrical. The diameter and the height of the swelling wave grow.

- Row 2: As the diameter of the swelling wave continues to expand, the height decreases.

- Row 4: As the swelling wave recoils, a central jet, which cannot be observed, is formed and ejects a small secondary droplet which can be seen in the last image of this row. It must be pointed out that the central jet ejects a relatively large droplet like the one shown in the images, or several relatively small droplets which, sometimes, are difficult to observe, especially with monochromatic light condition which generates fringe patterns in the background. It will be seen later that the observation of the secondary droplets can be improved by using white light which generates a more homogeneous background.

- Row 5 and 6: The secondary droplet travels upwards, and the surface returns to calmness.

Figure 5.2: Sequential images of jetting type 1: Observation of swelling wave, secondary droplet ejected from central jet & without observation of central jet. Technical ethanol droplet: diameter $D = 0.25$ mm, vertical velocity $V_y = 5.3$ m/s, velocity $V = 5.3$ m/s.

Jetting Type 2: Observation of Crown-like Wave (Unbroken), Secondary Droplet Ejected from Central Jet, Central Jet

For a given fluid, the generation of this type of jetting requires higher impinging energy which corresponds to either larger droplet diameters or higher velocities than the first type. Figure 5.3 shows the observation of this type of jetting, and the phenomenon has the following characteristic steps:

- Row 1: The impact forms a symmetrical crown-like wave, and the crown-like wave is unbroken. A close view of the crown-like wave is shown in Figure 5.4(a). A comparison to the swelling wave shown in Figure 5.4(b), the outer wall-surface of the crown-like wave is developed into a concave arc shape, and on the top-end of the wave, an obvious rim is formed and grows radially. Secondary droplets are not ejected from the rim of the crown, and it is thus called unbroken.

- Row 2: As the diameter of the crown-like wave expands, the height starts to retract.

- Row 3: The first image in this row shows that a very small secondary droplet is ejected from the central jet, and it travels upwards until it is out of the observation area in the fifth image in this row. Small droplets like this are more difficult to see with a background full of fringe patterns, but it is obvious against the homogeneous background.

- Row 4: Following the secondary droplet, the central jet rises above the horizontal surface. Due to the limited kinetic energy, the central jet moves upwards slowly, and it does not go far until the maximum height is reached.

- Row 5: As the central jet reaches the maximum height, it starts to retract. Since more and more liquid retracts, the lower part of the jet becomes wider.
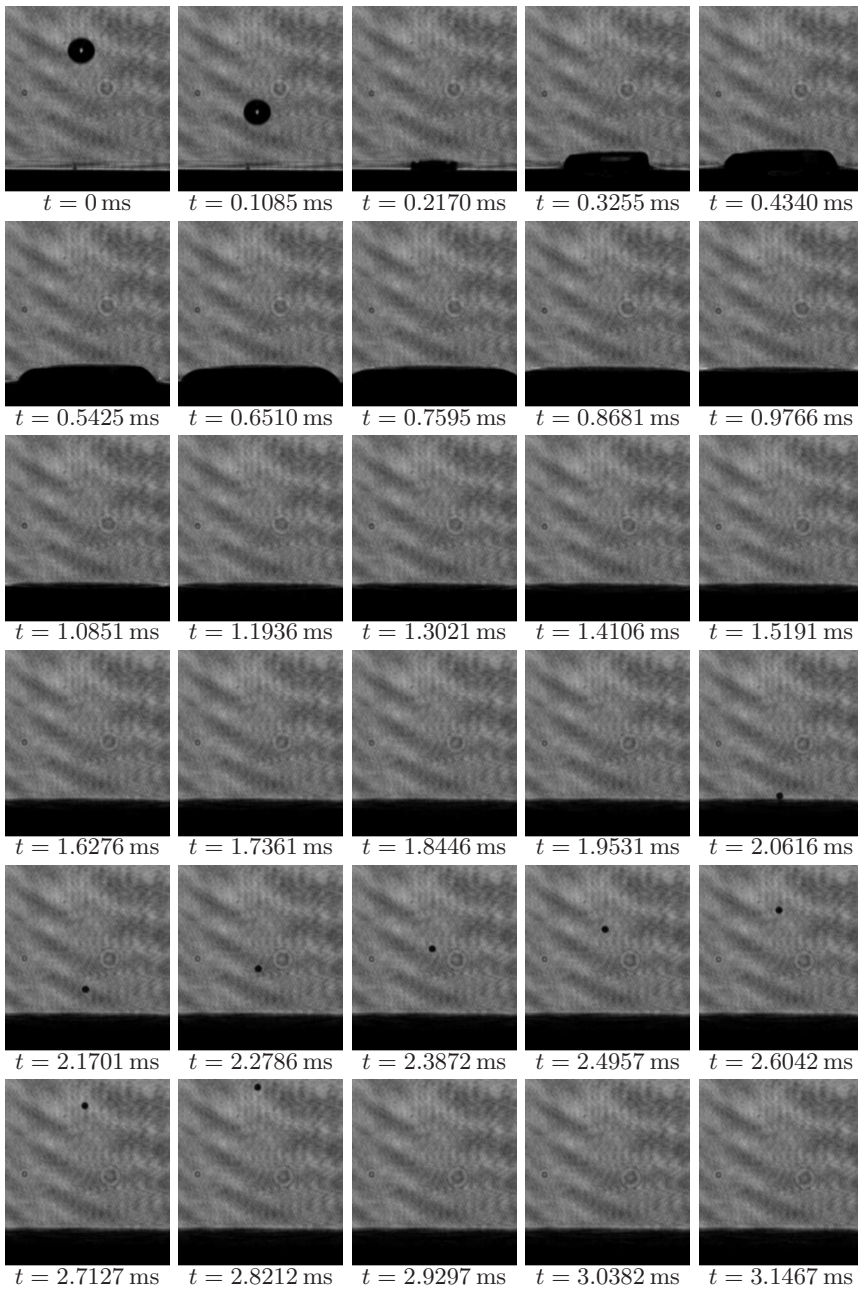
- Row 6: The surface of the pool recovers.
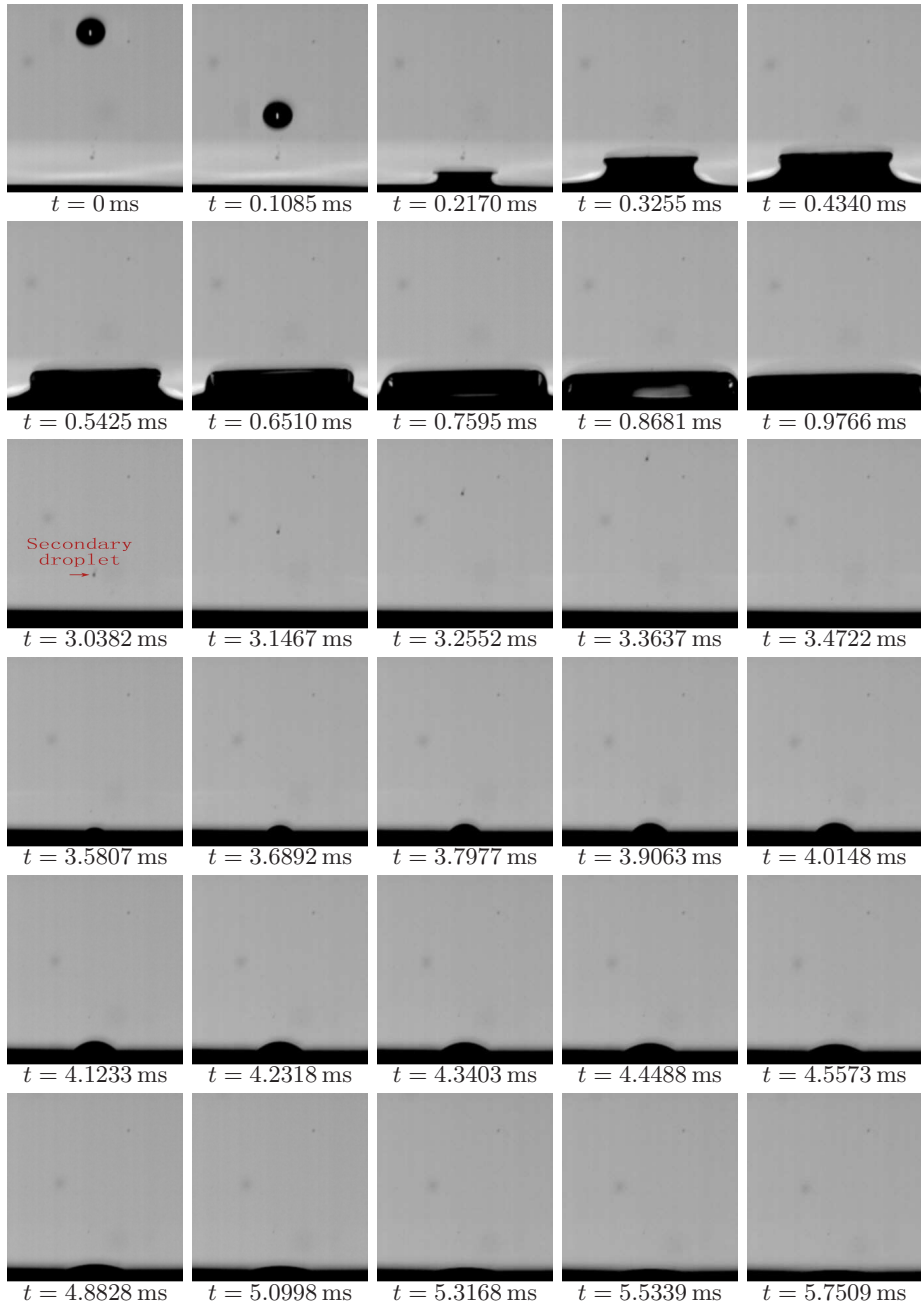
Figure 5.3: Sequential images of jetting type 2: Observation of crown-like wave, secondary droplet ejected from central jet, low central jet. 1-propanol droplet: diameter $D = 0.28\,\text{mm}$, vertical velocity $V_y = 7.3\,\text{m/s}$, velocity $V = 7.3\,\text{m/s}$.

(a) Crown-like wave in jetting type 2.

(b) Swelling wave in jetting type 1.
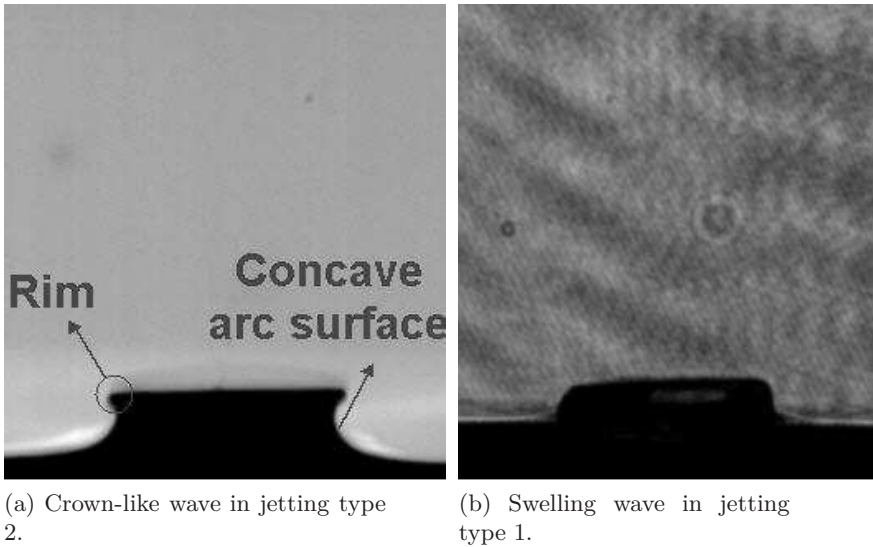
Figure 5.4: A comparison of a Crown-like wave in jetting type 2 and a swelling wave in jetting type 1.

Jetting Type 3: Observation of Crown-like Wave (Broken), Central Jet & With/out Generation of Secondary Droplet Ejected from Central Jet

For a given fluid, the crown-like wave is broken when the impact energy is further increased from the jetting type 2. A more obvious central jet can be observed, and depending on the energy level, the secondary droplets may or may not be generated from the central jet. Figure 5.6 and Figure 5.5 show the observation of this type of jetting with/out secondary droplets ejected from the central jet, respectively, and the phenomenon has several characteristic steps:

- Row 1: One notable thing for Figure 5.5 and Figure 5.6 is that the backgrounds in the figures contain more small droplets than the background from jetting type 2. The small droplets are thrown-off by the shutter due to a high flow rate, and most of them are not in the camera focus.

  - Figure 5.5: The droplet falls vertically, and the crown-like wave is formed without breaking as shown in the fourth picture in this row. The crown-wave is broken in the last picture of this row, and small secondary droplets are ejected in radial and upward direction from the rim.

– Figure 5.6: Similarly, the unbroken crown-like wave is formed in the third picture, and the secondary droplets are ejected in the following picture.

The maximum height of the crown-like wave is reached in a short time within a couple of frames. Due to the discrete image capture, the exact moment can be missed, while it is around the last figure of Row 1 or the first figure of the Row 2.

- Row 2: The wave descends in both cases.

- Row 3:
  – Figure 5.5: The wave nearly decreases to the surface of the pool.
  – Figure 5.6: A small secondary droplet is ejected in the first picture of the row, and it travels upwards. The central jet is observed in the last image of this row.

- Row 4: As the central jet can be seen in both Figures, the two central jets are compared.
  – Figure 5.5: The central jet moves upwards, and a "neck" is formed and can be observed in the third image in this row. The stretching effect from the inertial, gravitational and surface tension forces is not strong enough to break the neck, and as the liquid in the top part of the central jet retracts the neck is thickened again (in fourth and fifth images in this row).
  – Figure 5.6: Differently, the neck reaches nearly the narrowest status in the second image, and it is broken longitudinally in the third image. The breaking of the central jet ejects a secondary droplet, and it travels upwards.

- Row 5 and 6: The central jet retracts, and the surface of the liquid pool recovers.

$t = 0\,\mathrm{ms}$	$t = 0.1085\,\mathrm{ms}$	$t = 0.2170\,\mathrm{ms}$	$t = 0.3255\,\mathrm{ms}$	$t = 0.4340\,\mathrm{ms}$
$t = 0.5425\,\mathrm{ms}$	$t = 0.6510\,\mathrm{ms}$	$t = 0.7595\,\mathrm{ms}$	$t = 0.8681\,\mathrm{ms}$	$t = 0.9766\,\mathrm{ms}$
$t = 1.9531\,\mathrm{ms}$	$t = 2.0616\,\mathrm{ms}$	$t = 2.1701\,\mathrm{ms}$	$t = 2.2786\,\mathrm{ms}$	$t = 2.3872\,\mathrm{ms}$
$t = 2.4957\,\mathrm{ms}$	$t = 2.6042\,\mathrm{ms}$	$t = 2.7127\,\mathrm{ms}$	$t = 2.8212\,\mathrm{ms}$	$t = 2.9297\,\mathrm{ms}$
$t = 3.0382\,\mathrm{ms}$	$t = 3.1467\,\mathrm{ms}$	$t = 3.2552\,\mathrm{ms}$	$t = 3.3637\,\mathrm{ms}$	$t = 3.4722\,\mathrm{ms}$
$t = 3.5807\,\mathrm{ms}$	$t = 3.6892\,\mathrm{ms}$	$t = 3.7977\,\mathrm{ms}$	$t = 3.9063\,\mathrm{ms}$	$t = 4.0148\,\mathrm{ms}$
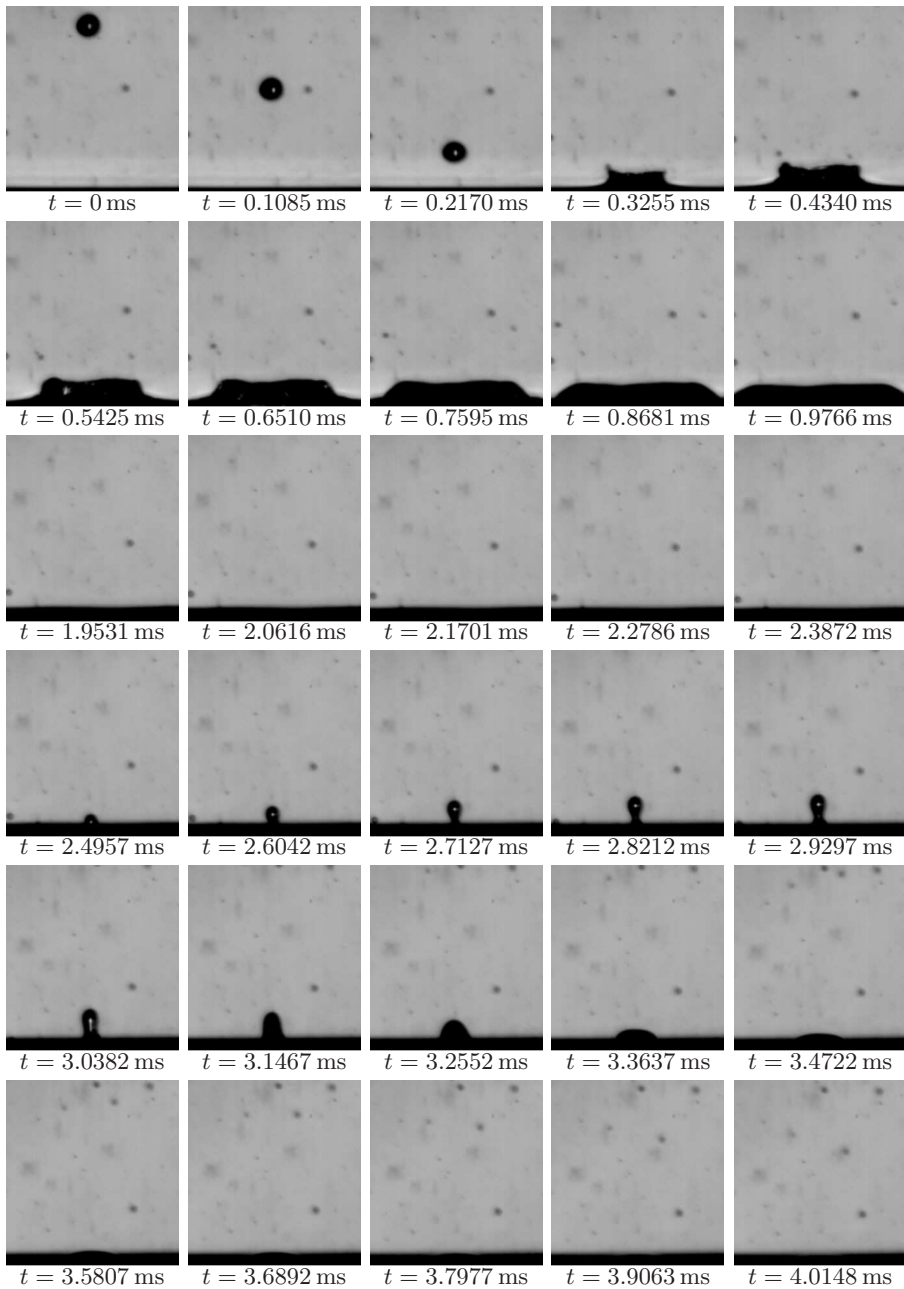
Figure 5.5: Sequential images of jetting type 3: Observation of crown-like wave (broken), central jet & without generation of secondary droplet ejected from central jet. n-pentane droplet: diameter $D = 0.22\,\mathrm{mm}$, vertical velocity $V_y = 5.2\,\mathrm{m/s}$, velocity $V = 5.2\,\mathrm{m/s}$.
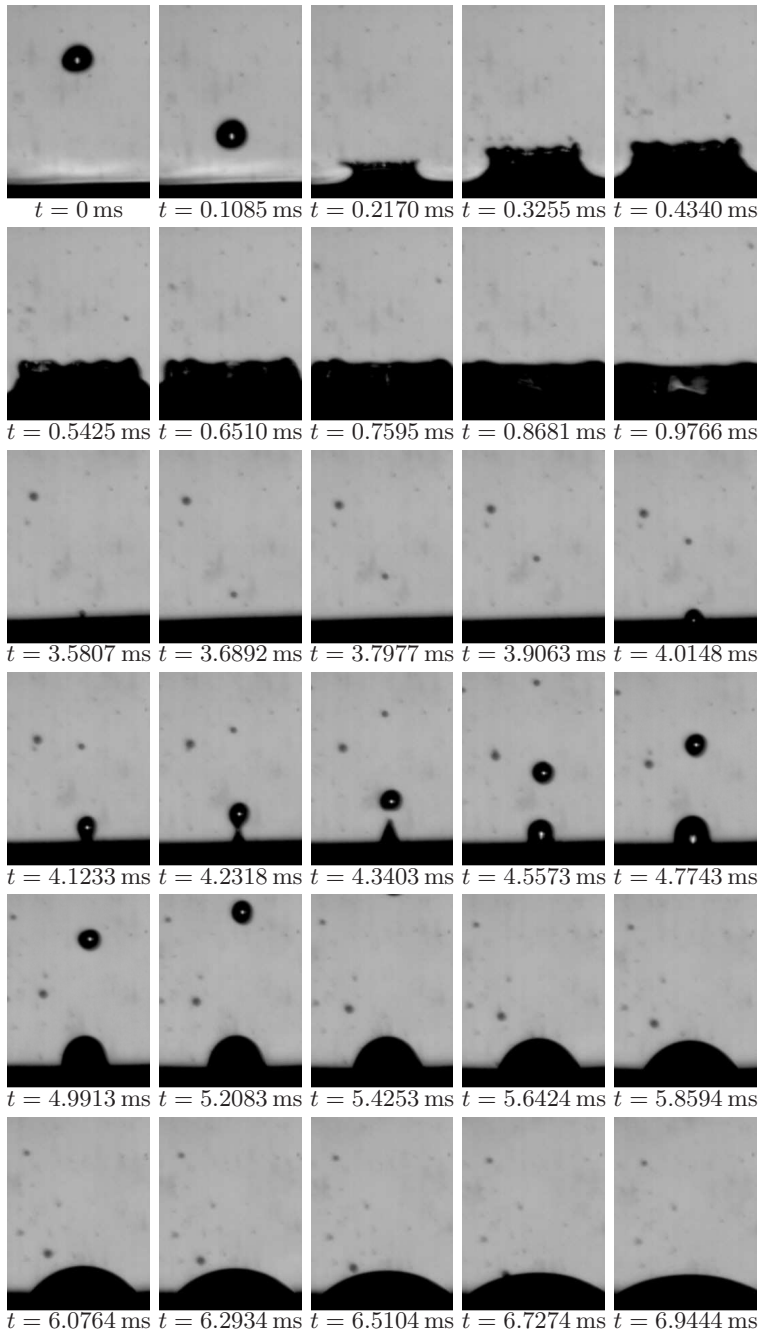
Figure 5.6: Sequential images of jetting type 3: Observation of crown-like wave (broken), central jet, secondary droplet ejected from central jet. n-pentane droplet: diameter $D = 0.26\,\text{mm}$, vertical velocity $V_y = 5.9\,\text{m/s}$, velocity $V = 5.9\,\text{m/s}$.

5.2.2 Results from Jetting

The fundamental parameters, diameter and velocity, are arranged according to experiment sets with different fluids. The specific uncertainty for each data point is evaluated by using the method described in Chapter 4.

In order to check that the impacts are vertical, the impinging angles from all experiment sets are presented after the fundamental parameters.

Fundamental Parameters from Jetting

The fundamental parameters, diameter (D) and velocity (V), of jetting from distilled water, technical ethanol, n-pentane, methanol and 1-propanol are shown in Figure 5.7(a), (b), (c), (d) and (e), respectively. By using the method in Section 4.3, the uncertainties for the parameters are investigated for each single data point, and the results are shown in the figures.

The information of the fundamental parameters from jetting for all fluids is shown in Table 5.1. The table reports the information on the following aspects:

- The velocity ranges (m/s) and the uncertainty ranges for the velocity ($\pm\%$).

- The diameter ranges (mm) and the uncertainty ranges for the velocity ($\pm\%$).

- The number of measurements.

Table 5.1: Information of fundamental parameters from jetting.

Fluid	D (mm)	$\frac{\Delta D}{D}(\pm\%)$	V (m/s)	$\frac{\Delta V}{V}(\pm\%)$	Measurements
Distilled water	0.15-0.53	2.75-2.78	4.5-12.1	2.60-2.72	230
Technical ethanol	0.16-0.35	2.75-2.80	5.2-9.8	2.62-2.77	179
n-pentane	0.13-0.57	2.75-2.80	2.2-6.3	2.70-3.63	542
Methanol	0.21-0.40	2.75-2.77	2.9-7.9	2.65-3.19	439
1-propanol	0.17-0.43	2.75-2.78	4.7-9.9	2.62-2.82	428
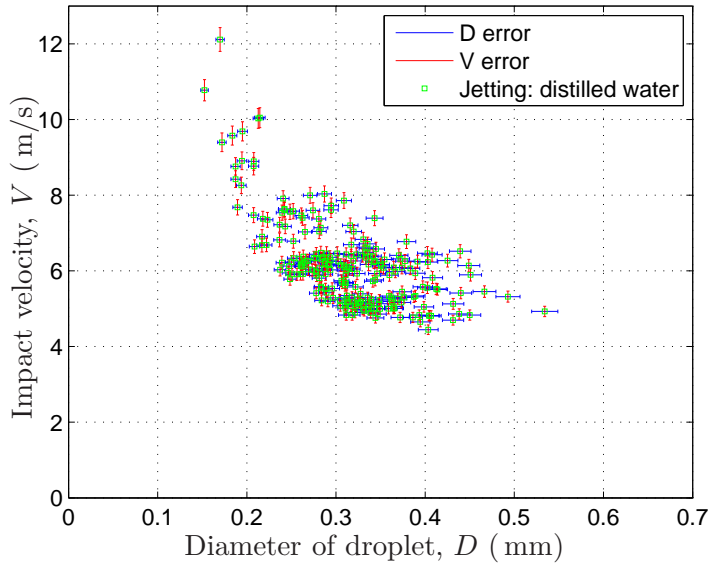
(a) Distilled water
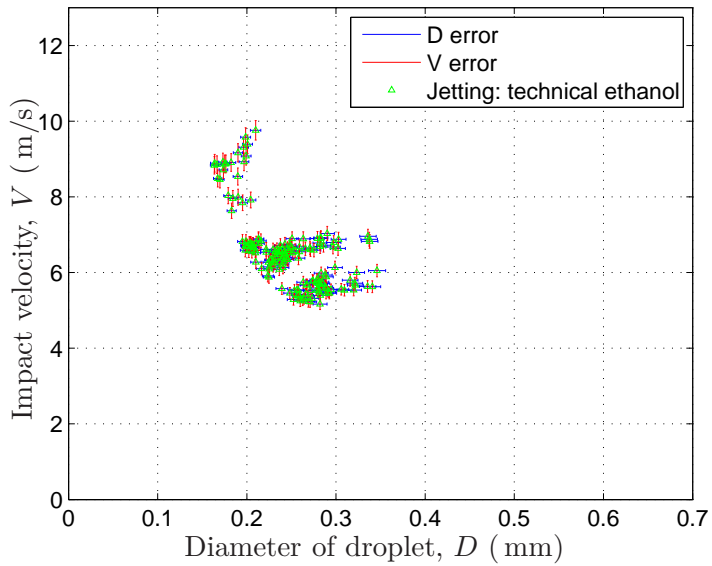
(b) Technical ethanol

Figure 5.7: Fundamental parameters of jetting: velocity versus diameter.
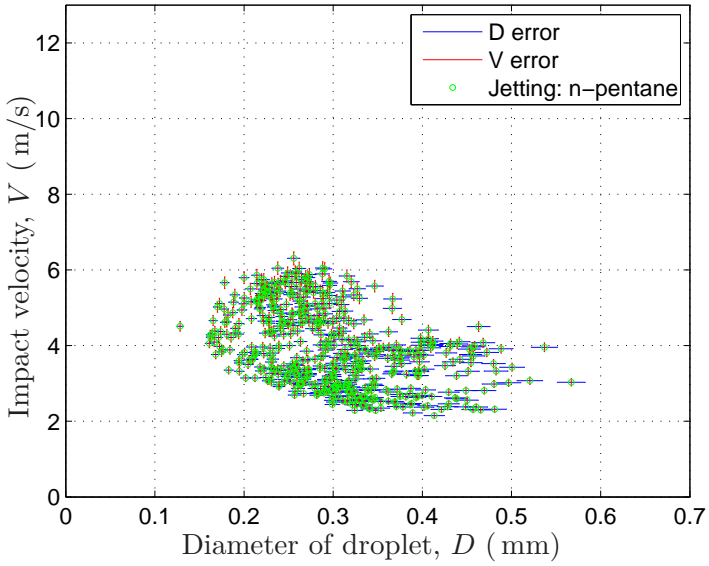
(c) n-pentane
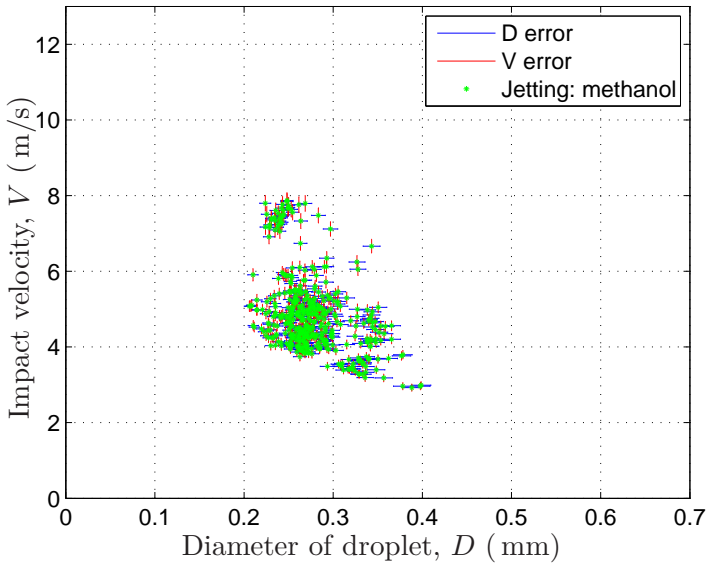
(d) Methanol

Figure 5.7: Fundamental parameters of jetting: velocity versus diameter. (Continued)
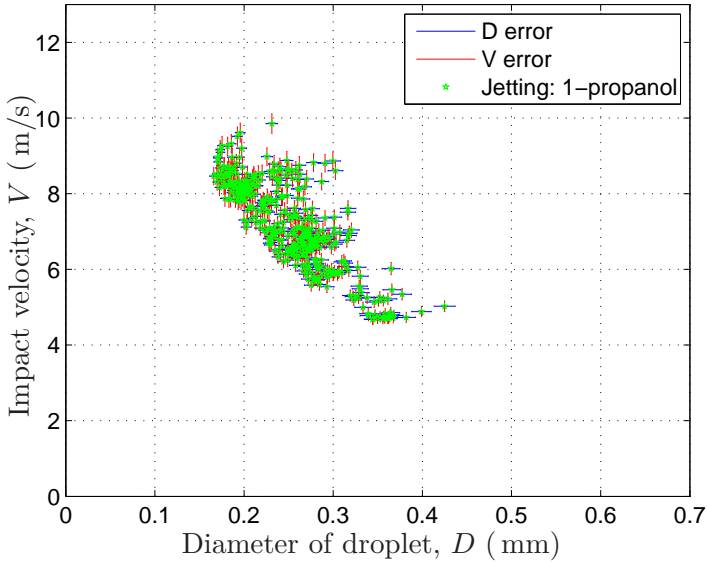
(e) 1-propanol

Figure 5.7: Fundamental parameters of jetting: velocity versus diameter. (Continued)

Impact Angle from Jetting: All Fluids

The impact angles in the jetting regime are investigated. The schematic drawing of the impact angle is shown in Figure 5.8. As the normal component of velocity was tracked without direction, the calculated angle is below 90°. Thus, the impact angle is defined as the ≤ 90° angle formed by the incident path and the horizontal surface, and this means that droplets following two incident paths, path 1 and path 2, which are symmetrically distributed on different side of the axis have the same impact angle as shown in the figure.

90° angle represents a completely vertical impact. The angles from all different experiment sets are shown in Figure 5.9.

As shown in the figure, most of the impact angles are above 85°, and it indicates that the impacts are nearly vertical as the mean value of the impact angles is close to 90°. If droplets impacting from different sides are considered with directions, a mean value of the impact angles would be even closer to 90°.

It must be noted that the investigation is in one plane (x-z plane) of the two planes, and the same condition can be expected on the other plane (y-z plane).
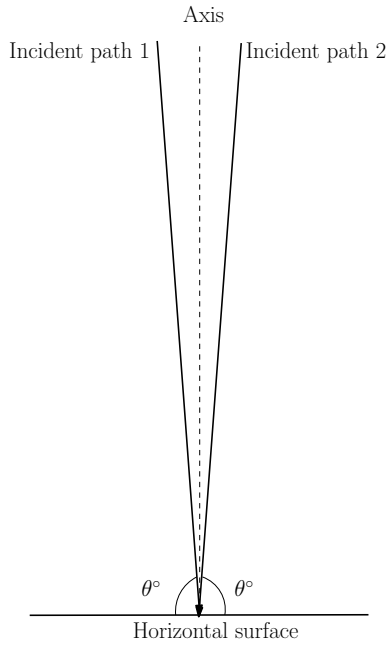
Figure 5.8: Schematic drawing of the impact angle ($\theta°$).
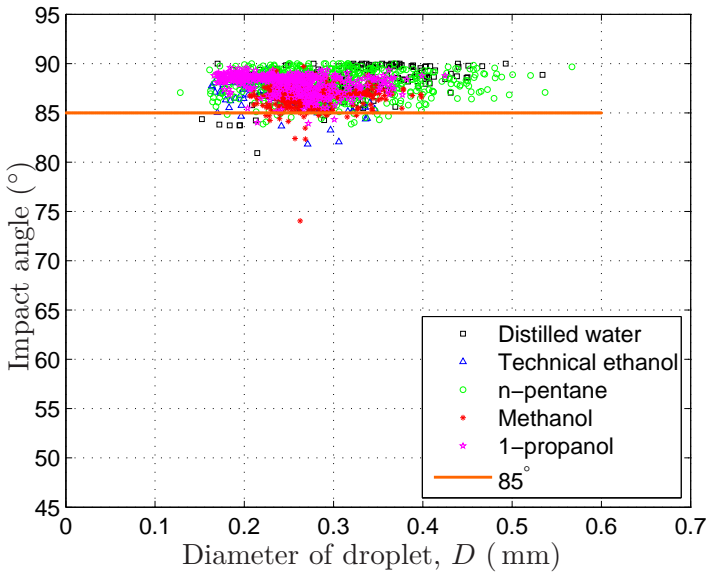
Figure 5.9: Impact angles in jetting versus diameter (D).

5.3 Observations and Results of Coalescence

5.3.1 Observations from Coalescence

Coalescence occurs at a lower-level impact energy than jetting, and the main phenomenological difference from jetting is that characteristic observations other than merging of the impinging droplet are not found. Two types of coalescence, associated with two different energy levels, were observed in the experiments. The first type happens when a droplet impacts with extremely low energy which means, in general, small droplet size and low velocity. The low energy impact causes a small and subtle wave on the surface of the deep liquid pool, and the wave disappears in a very short time. The other type of coalescence happens when a droplet impacts with higher energy. The high energy impact causes an obvious and strong wave which lasts for a much longer time than the small wave does in the first type of coalescence.

Coalescence Type 1: Low Impact Energy, Small and Subtle Wave

This type of coalescence occurs when the impact energy is low. The low collision energy droplets can be observed under two conditions of different parameters: in the first condition the droplet can have large size and extremely low velocity, in the second condition the droplet can have smaller size but slightly higher velocity. Due to the physical characteristics of the experimental setup, this type of coalescence was mostly observed with small distilled water droplets (below $0.2\,\mathrm{mm}$) with low velocities (below $1\,\mathrm{m/s}$). Due to the small size, the event proceeds very fast, some characteristic steps may not be observed. In order to see more status in the low collision energy coalescence, 3 successions of sequential images are given in Figure 5.10(a), (b) and (c).

The characteristic steps in 3 successions of sequential images are:

- Row 1 in Figure 5.10(a), (b) and (c): Row 1 shows the falling of the droplets. Comparing to the falling droplets in jetting, the falling distances are much shorter since the cropped images are much smaller in height, while more images with falling droplets are obtained. This means that the falling velocities in coalescence type 1 are much lower.

- Row 2 in Figure 5.10(a), (b) and (c): In this row, the droplets coalesce into the liquid pool. Due to the smaller size and relatively high velocity. Figure 5.10(c) shows that the droplet is first deformed (the second image in this row), and at this point, the interface between the
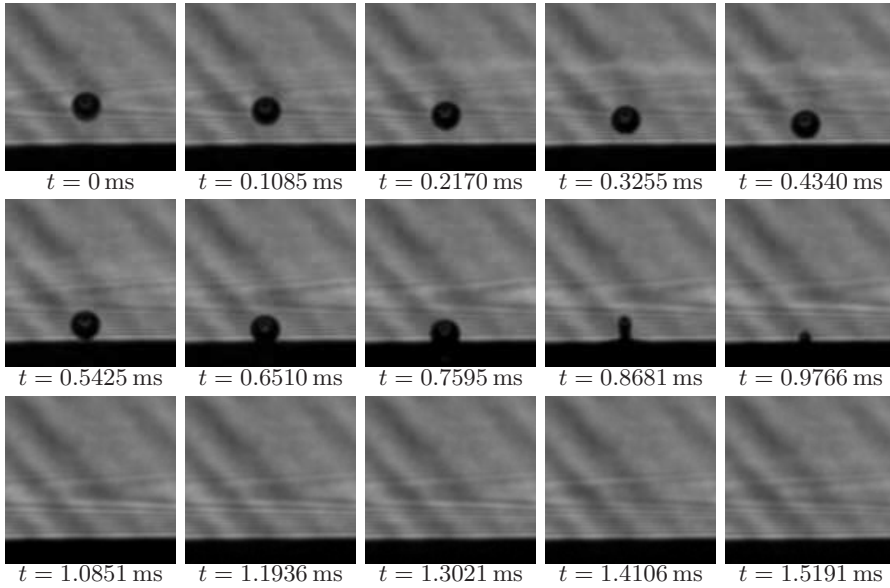
(a) Coalescence type 1-1.

Figure 5.10: (a) Coalescence type 1-1: Low impact energy, small and subtle wave. Distilled water droplet: diameter $D = 0.11\,\mathrm{mm}$, vertical velocity $V_y = 0.17\,\mathrm{m/s}$, velocity $V = 0.17\,\mathrm{m/s}$.

droplet and the pool surface is not broken. Due to the compression, the top of the droplet is flat. When the droplet coalesces into the liquid pool (the third image in the row in both Figure 5.10(c) and Figure 5.10(a)), the top part of the droplet is restored to the circular shape due to the disappearing of the compression force. A wave propagates along the surface of the droplet, and a "neck" is formed at the interface of the droplet and the liquid film due to the imbalanced surface tension.

- Row 3 of Figure 5.10(c): As more and more liquid in the top part of the droplet flows into the liquid pool, the neck becomes thinner and the top part becomes smaller as shown in the row. The similar status can also be seen in the second row in both Figure 5.10(a) and Figure 5.10(b). The droplet finally merges into the pool. The surface slightly shakes and returns to calmness.

$t = 0\,\text{ms}$ $\quad$ $t = 0.1085\,\text{ms}$ $\quad$ $t = 0.2170\,\text{ms}$ $\quad$ $t = 0.3255\,\text{ms}$ $\quad$ $t = 0.4340\,\text{ms}$

$t = 0.5425\,\text{ms}$ $\quad$ $t = 0.6510\,\text{ms}$ $\quad$ $t = 0.7595\,\text{ms}$ $\quad$ $t = 0.8681\,\text{ms}$ $\quad$ $t = 0.9766\,\text{ms}$

(b) Coalescence type 1-2.

$t = 0\,\text{ms}$ $\quad$ $t = 0.1085\,\text{ms}$ $\quad$ $t = 0.2170\,\text{ms}$ $\quad$ $t = 0.3255\,\text{ms}$ $\quad$ $t = 0.4340\,\text{ms}$

$t = 0.5425\,\text{ms}$ $\quad$ $t = 0.6510\,\text{ms}$ $\quad$ $t = 0.7595\,\text{ms}$ $\quad$ $t = 0.8681\,\text{ms}$ $\quad$ $t = 0.9766\,\text{ms}$

$t = 1.0851\,\text{ms}$ $\quad$ $t = 1.1936\,\text{ms}$ $\quad$ $t = 1.3021\,\text{ms}$ $\quad$ $t = 1.4106\,\text{ms}$ $\quad$ $t = 1.5191\,\text{ms}$
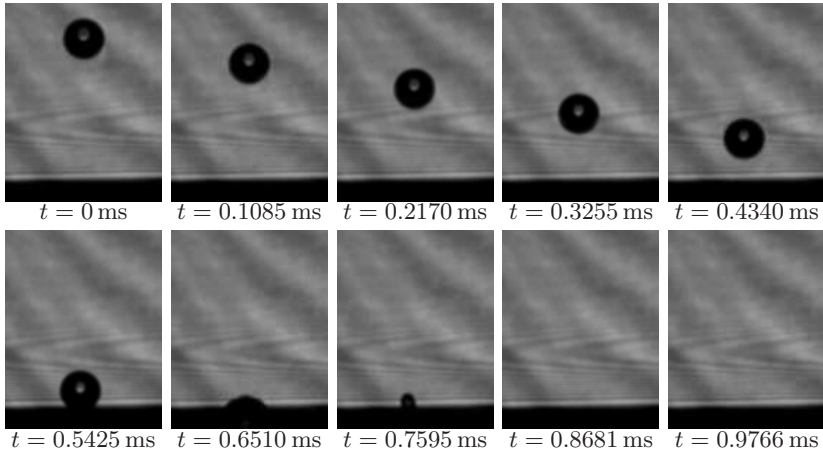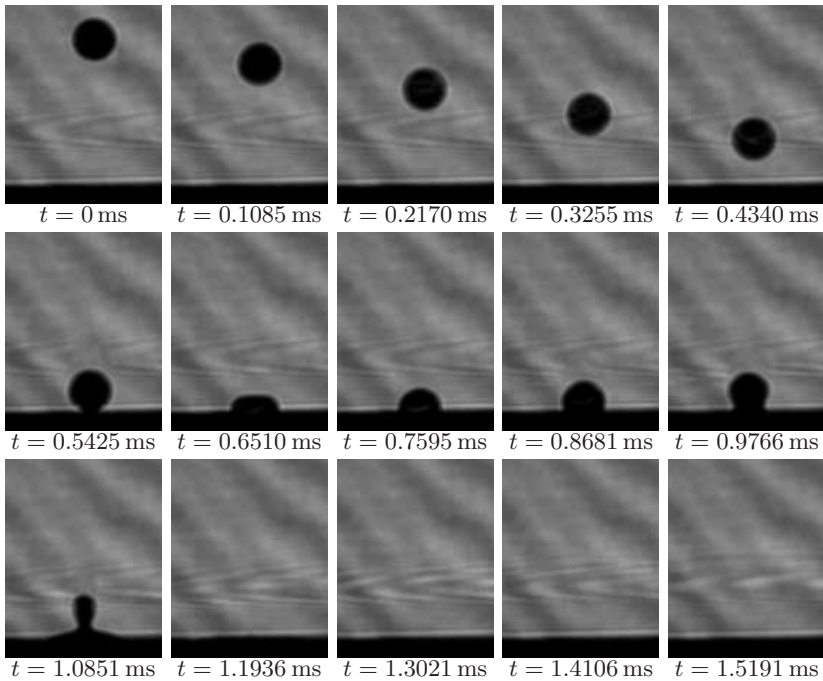
(c) Coalescence type 1-3.

Figure 5.10: (b) Coalescence type 1-2: Low impact energy, small and subtle wave. Distilled water droplet: diameter $D = 0.17\,\text{mm}$, vertical velocity $V_y = 0.97\,\text{m/s}$, velocity $V = 0.97\,\text{m/s}$.
(c) Coalescence type 1-3: Low impact energy, small and subtle wave. Distilled water droplet: diameter $D = 0.17\,\text{mm}$, vertical velocity $V_y = 0.96\,\text{m/s}$, velocity $V = 0.96\,\text{m/s}$.

Coalescence type 2: High impact energy, obvious and strong wave

Comparing with the coalescence type 1, this type of coalescence happens with higher impact energy. The impact leads to an obvious and strong wave on the pool surface. Figure 5.11 shows the characteristic steps in the coalescence:

- Row 1: A droplet falling vertically, and approaches the surface of a deep liquid pool.

- Row 2: The droplet impacts onto the pool surface in the second image in this row. In the second image, the top part of the droplet remains
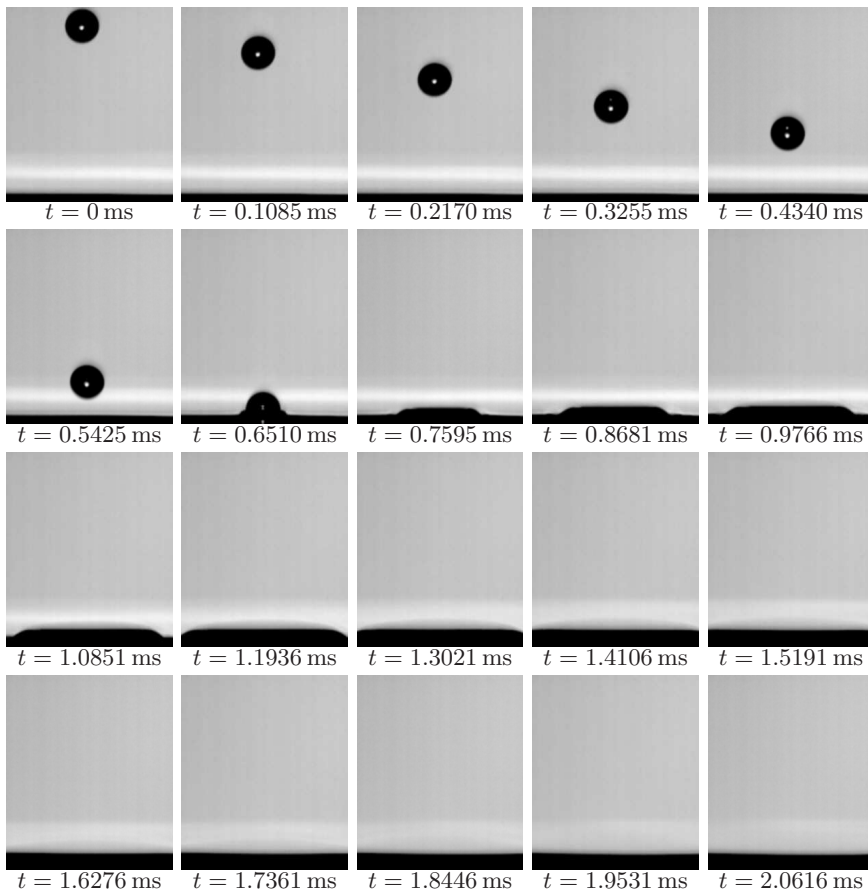
Figure 5.11: Coalescence type 2: High impact energy, obvious and strong wave. Methanol droplet: diameter $D = 0.30$ mm, vertical velocity $V_y = 2.2$ m/s, velocity $V = 2.2$ m/s.

circular, while the bottom part is deformed and the view is blocked by a expansion wave formed at the pool surface. From the third image in this row, the droplet merges into the pool, and the wave expands on the surface.

- Row 3 and 4: As the wave expands, the surface returns back to calmness.

5.3.2 Results from Coalescence

The fundamental parameters, diameter (D) and velocity (V), of coalescence from distilled water, technical ethanol, n-pentane, methanol and 1-propanol are shown in Figure 5.12(a), (b), (c), (d) and (e), respectively.

The information of the fundamental parameters from jetting for all fluids is shown in Table 5.2.

Table 5.2: Information of fundamental parameters from coalescence.

Fluid	D (mm)	$\frac{\Delta D}{D}(\pm\%)$	V (m/s)	$\frac{\Delta V}{V}(\pm\%)$	Measurements
Distilled water	0.06-0.67	2.75-3.01	0.1-8.1	2.65-52.05	1020
Technical ethanol	0.07-0.67	2.75-2.95	0.1-8.9	2.63-51.02	897
n-pentane	0.10-0.54	2.75-2.83	0.3-3.9	2.93-19.20	353
Methanol	0.17-0.42	2.75-2.78	1.8-4.6	2.83-3.99	365
1-propanol	0.14-0.49	2.75-2.79	1.3-8.9	2.63-4.92	855

It needs to be noted that the uncertainty ratio, $\frac{\omega_V}{V}$, reaches a high level for distilled water and technical ethanol, the maximum values corresponds to the lowest velocity around $0.1\,\text{m/s}$. A few number of data points are associated with high uncertainty ratios above 10%, and these data points are from the low-collision-energy coalescence. It does not affect much the overall measuring accuracy because the absolute uncertainty is very small (below $\approx 0.05\,\text{m/s}$). The reason for the high value of the uncertainty ratio is that the displacement for calculating the velocity reaches the resolution limit, and it has been explained in Section 4.3.3.
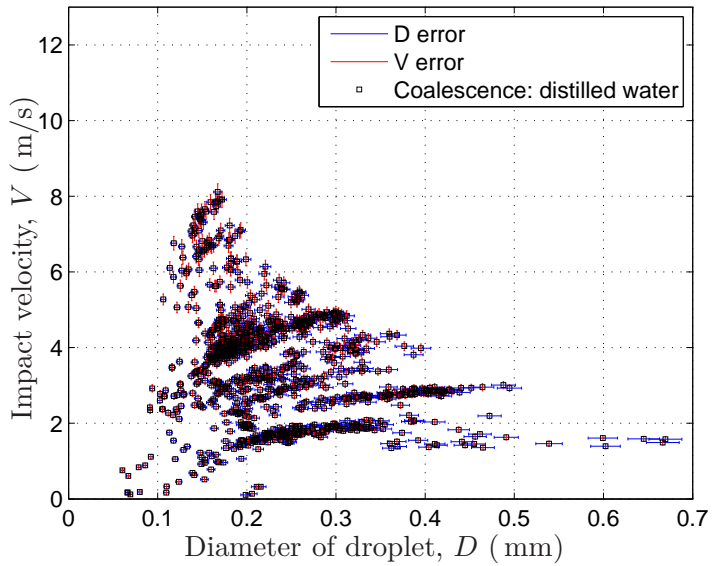
(a) Distilled water
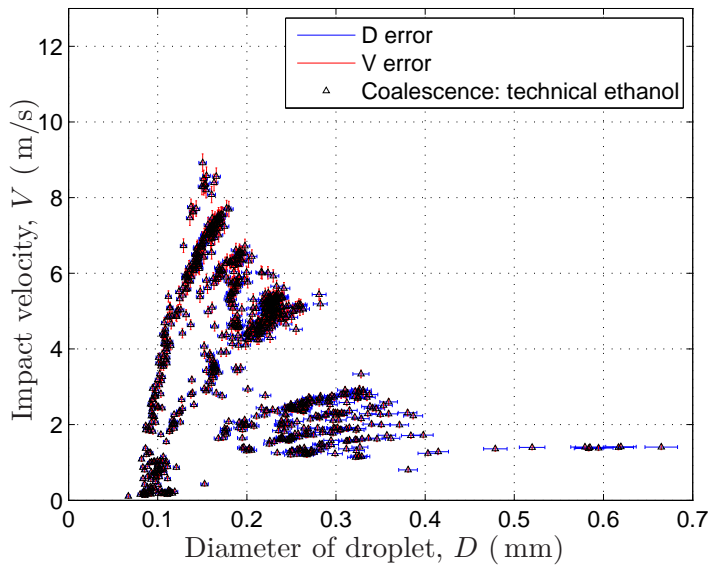
(b) Technical ethanol

Figure 5.12: Fundamental parameters of coalescence: velocity versus diameter.

(c) n-pentane

(d) Methanol

Figure 5.12: Fundamental parameters of coalescence: velocity versus diameter. (Continued)

(e) 1-propanol

Figure 5.12: Fundamental parameters of coalescence: velocity versus diameter. (Continued)

Impact Angle from Coalescence: All Fluids

The angles from all different experiment sets are shown in Figure 5.13. The impact angles in coalescence are quite vertical, and they are similar to the impact angles in jetting which are described in Section 5.2.2.
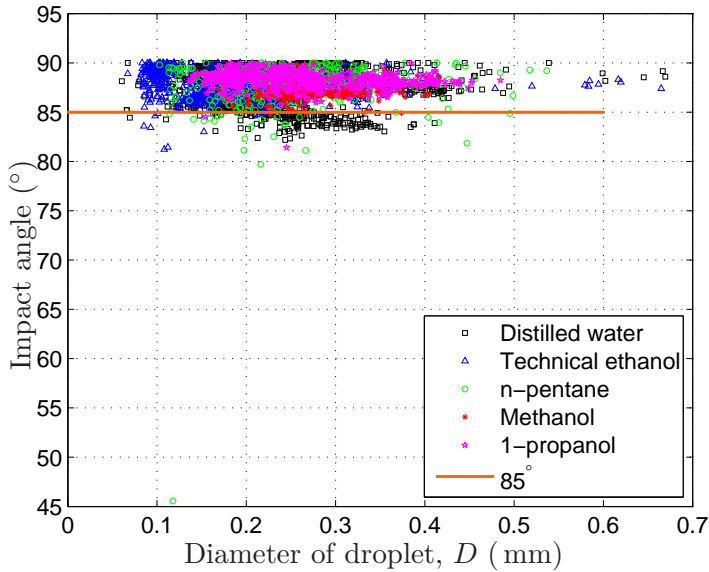
Figure 5.13: Impact angles in coalescence versus diameter (D).

5.4 Observations and Results of Bouncing

5.4.1 Observations from Bouncing

Bouncing occurs at an energy level between the two energy levels for co-alescence. The general observation in this regime is that a falling droplet does not merge into the deep pool but bounces off the pool surface. Theoret-ically, the droplet before and after bouncing is consistent in size. Bouncing, due to the low impact energy, does not disturb the pool surface much.

Figure 5.14 shows the sequential images in the bouncing regime. The characteristic steps in the sequential images are:

- Row 1: A droplet falls down vertically towards the surface of a liquid pool.

- Row 2: The droplet approaches the surface, and impacts with the surface on the second image in the row. The second image shows that the top part of the droplet remains spherical, while the bottom part is deformed. In the third image of this row, the droplet deforms to nearly the maximum level, which corresponds to the maximum ratio between the major and minor axes, and the droplet is flattened. A small disturbance can be seen around the flat droplet. In the fourth
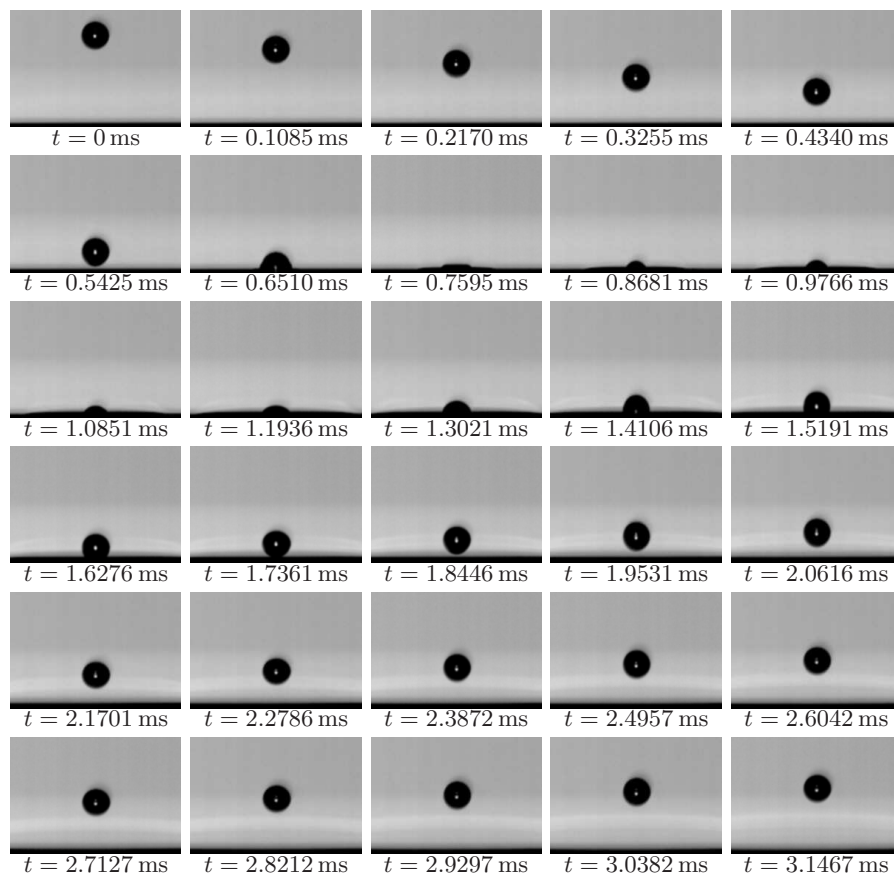
Figure 5.14: Bouncing: 1-propanol droplet: diameter $D = 0.24\,\text{mm}$, vertical velocity $V_y = 1.14\,\text{m/s}$, velocity $V = 1.14\,\text{m/s}$; bouncing diameter $D_b = 0.24\,\text{mm}$, vertical bouncing velocity $V_y = -0.29\,\text{m/s}$, velocity $V = -0.29\,\text{m/s}$.

and fifth images of this row, the droplet starts to bounce upwards, and the top part is firstly recovered into a spherical shape.

- Row 3: The droplet slowly bounces upwards, while it is still in contact with the pool surface.

- Row 4: The droplet gradually bounces off the surface, and in the third image in this row, it is finally detached from the surface.

- Row 5 and 6: The droplet travels upwards away the surface.

5.4.2 Results of Bouncing

The bouncing regime was observed in the experiment with three fluids, distilled water, technical ethanol and 1-propanol. The fundamental parameters, diameter (D) and velocity (V), of bouncing from distilled water, technical ethanol and 1-propanol are shown in Figure 5.15(a), (b) and (c), respectively.

Information of the fundamental parameters from jetting for all fluids is shown in Table 5.3.

Table 5.3: Information of fundamental parameters from bouncing.

Fluid	D (mm)	$\frac{\Delta D}{D}(\pm\%)$	V (m/s)	$\frac{\Delta V}{V}(\pm\%)$	Measurements
Distilled water	0.15-0.40	2.75-2.79	0.3-1.6	4.27-20.09	102
Technical ethanol	0.08-0.402	2.75-2.87	0.2-1.8	4.04-37.20	199
1-propanol	0.13-0.32	2.76-2.80	0.1-1.4	4.79-41.39	140
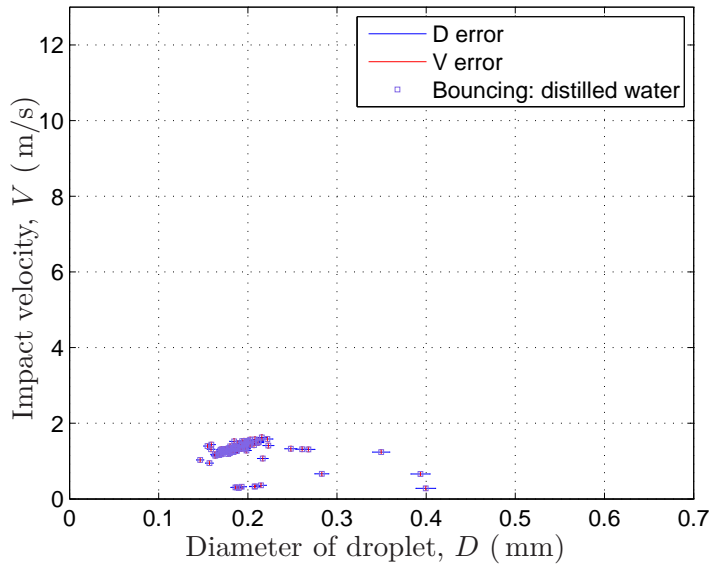
(a) Distilled water
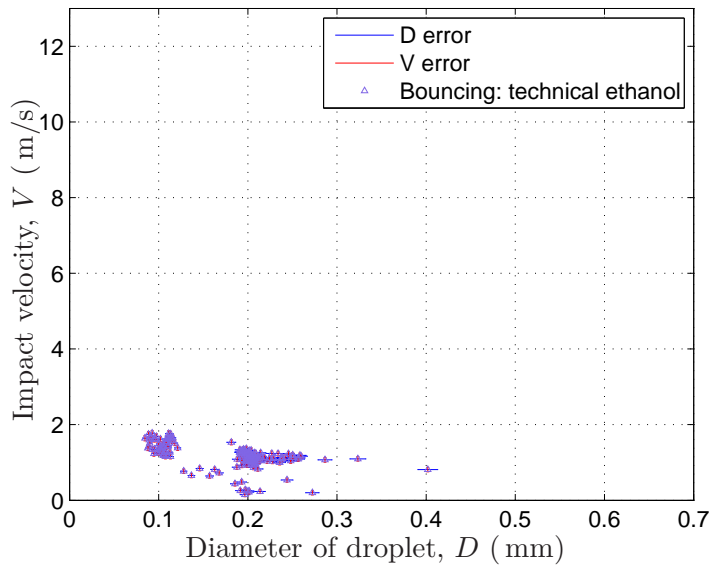
(b) Technical ethanol
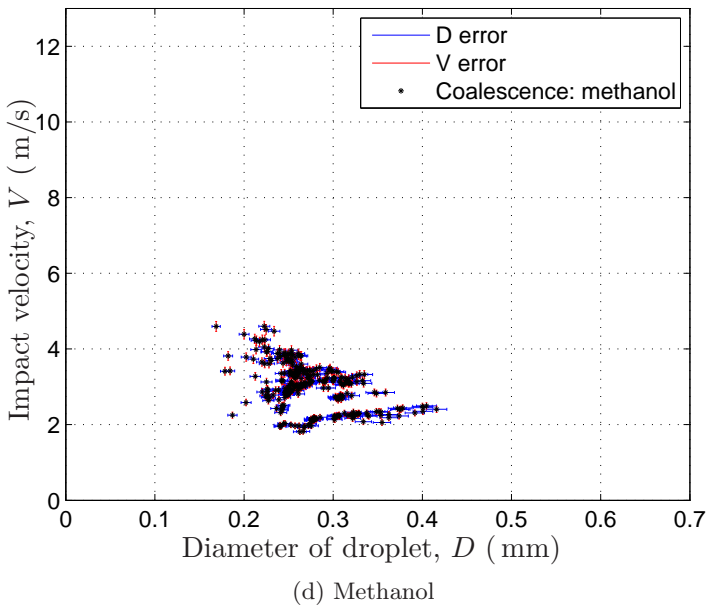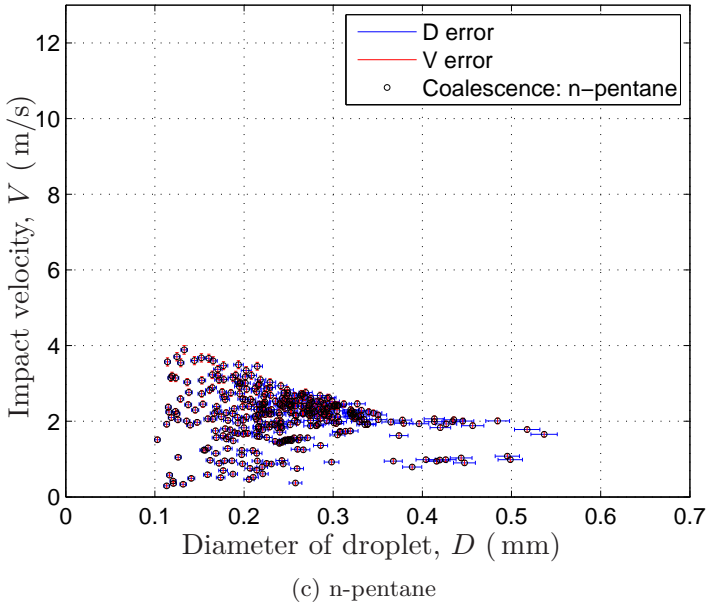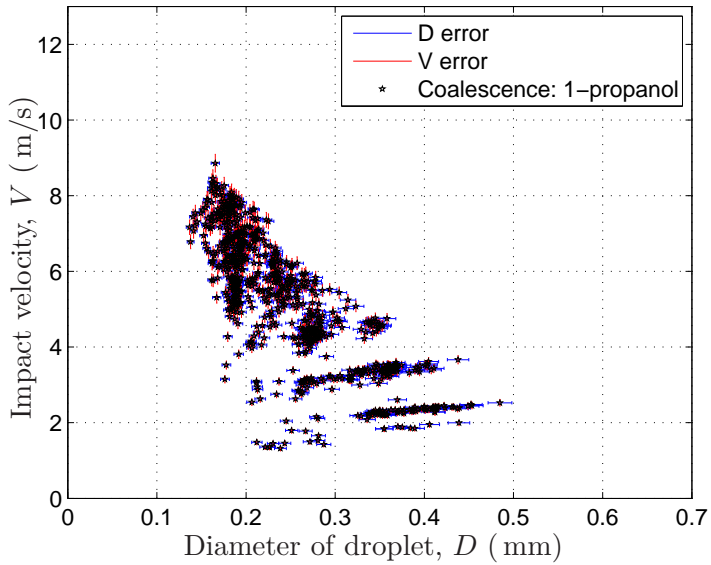
Figure 5.15: Fundamental parameters of bouncing: velocity versus diameter.
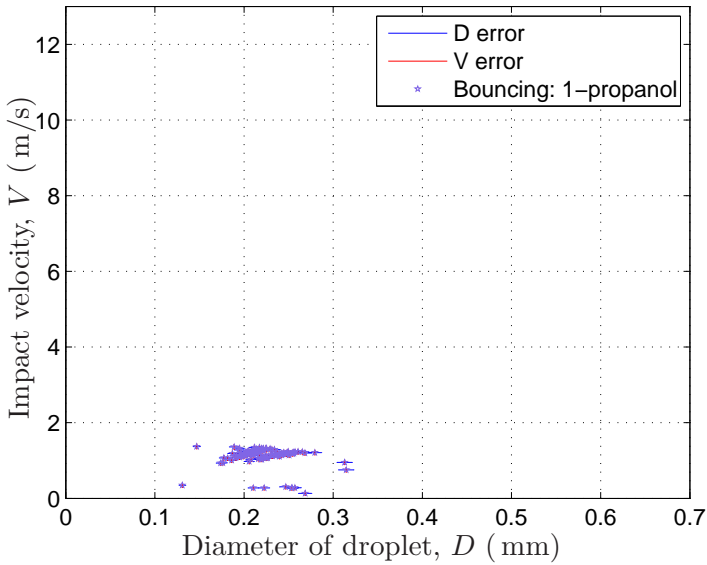
(c) 1-propanol

Figure 5.15: Fundamental parameters of bouncing: velocity versus diameter. (Continued)

Impact and Bouncing Angles from Bouncing: All Fluids

The impact angles from all different experiment sets are shown in Figure 5.16(a), and the bouncing angles are shown in Figure 5.16(b).

Figure 5.16(a) shows that most of the impact angles are above $85°$, and it indicates that the impacts are nearly vertical. Comparing with Figure 5.16(a), Figure 5.16(b) contains more data points below $85°$ with larger deviations from $90°$, and this indicates that the bouncing paths are affected by the factors such as asymmetrical 3-dimensional impacts and imperfect surface conditions. Nevertheless, the droplets with bouncing angles above $85°$ still constitute of most of the data points, and nearly all bouncing angles are above $80°$.
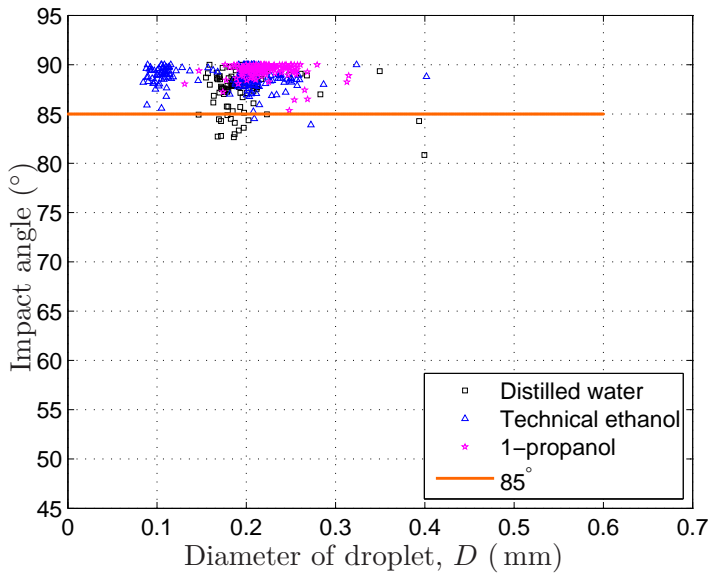
(a) Impact angle.
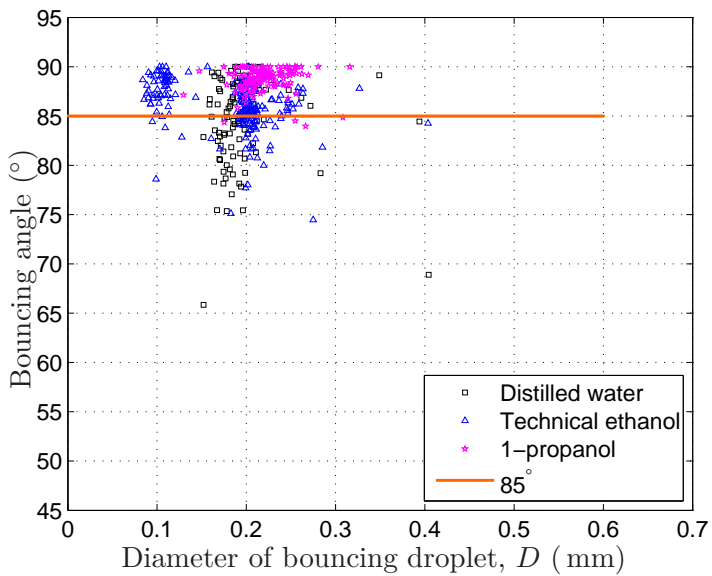
(b) Bouncing angle.

Figure 5.16: Impact and bouncing angles from bouncing.

5.5 Observations and Results of Partial Coalescence

5.5.1 Observations from Partial Coalescence

Partial coalescence is an intermediate regime between coalescence and bouncing. Since the energy level of bouncing is located between the energy levels of two types of coalescence, there exist two types of partial coalescence which are the transitional regimes of coalescence (low energy type)-bouncing and bouncing-coalescence (high energy type). Phenomenological differences are not obvious between them since both of the energy levels are quite low and close to the energy level of bouncing.

Partial coalescence is found only in experiments with distilled water, and it exists in a very narrow range of diameter and velocity. The reason why this transitional phenomenon is not found in the experiments with technical ethanol and 1-propanol, where both bouncing and coalescence are present, can be that the suitable range of diameter and velocity for the phenomenon is even more narrow than the ranges in the experiment with water.

Figure 5.17 shows the sequential images in the partial coalescence regime. The characteristic steps in the sequential images are:

- Row 1 and 2: A droplet falls onto the surface of a liquid pool.

- Row 3: The third image in this row shows that the droplet coalesces with the liquid pool, and a "neck" is formed between the top part of the droplet and the pool surface. The narrowing down of the neck is not captured due to the image interval. In the fourth image in this row, the neck is broken, and the top part of the droplet is detached. Due to the detachment, the bottom part of the droplet retracts downwards to the surface, and a small surface disturbance is caused as shown in the fourth image. The detached droplet travels downwards by the inertial and gravitational force, and the last image shows that it hits the pool surface.

- Row 4: The detached droplet can be considered as a new impinging droplet, and when the bouncing conditions are satisfied by the velocity and diameter of the detached droplet, it bounces off the surface as shown in the third image.

- Row 5 and 6: The reflected droplet travels upwards.
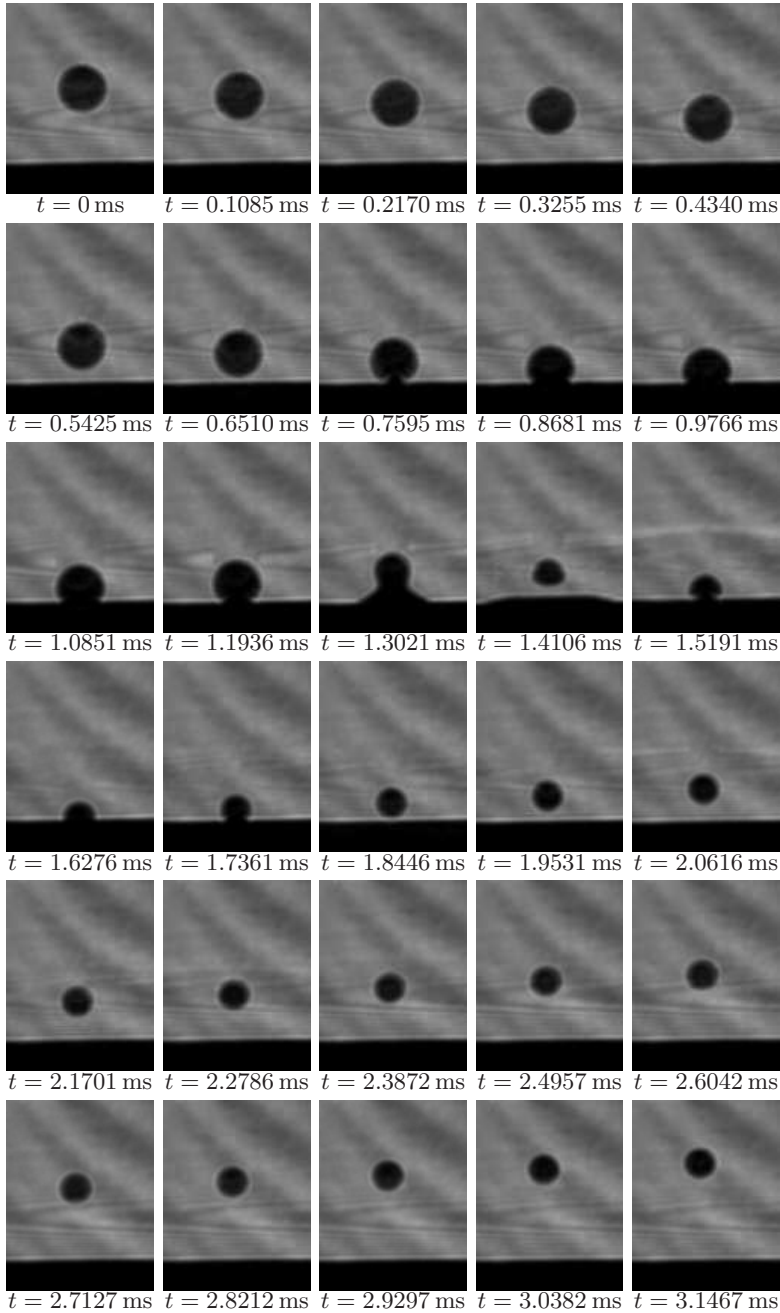
Figure 5.17: Partial coalescence: distilled water droplet: diameter $D = 0.18\,\text{mm}$, vertical velocity $V_y = 0.29\,\text{m/s}$, velocity $V = 0.29\,\text{m/s}$; bouncing diameter $D_b = 0.12\,\text{mm}$, vertical bouncing velocity $V_y = -0.26\,\text{m/s}$, velocity $V = -0.26\,\text{m/s}$.

5.5.2 Results from Partial Coalescence

Figure 5.18 shows the the fundamental parameters, diameter (D) and velocity (V), from partial coalescence in the experiment with distilled water.

The information of the fundamental parameters from partial coalescence for distilled water is shown in Table 5.4.

Impact and Bouncing Angles in Partial Coalescence: Distilled water

The impinging and bouncing angles of partial coalescence can be found in Figure 5.19(a) and Figure 5.19(b), and they are quite similar with Figure 5.16(a) and Figure 5.16(b) for the angles in bouncing because partial coalescence can be considered as the combination of coalescence and bouncing.
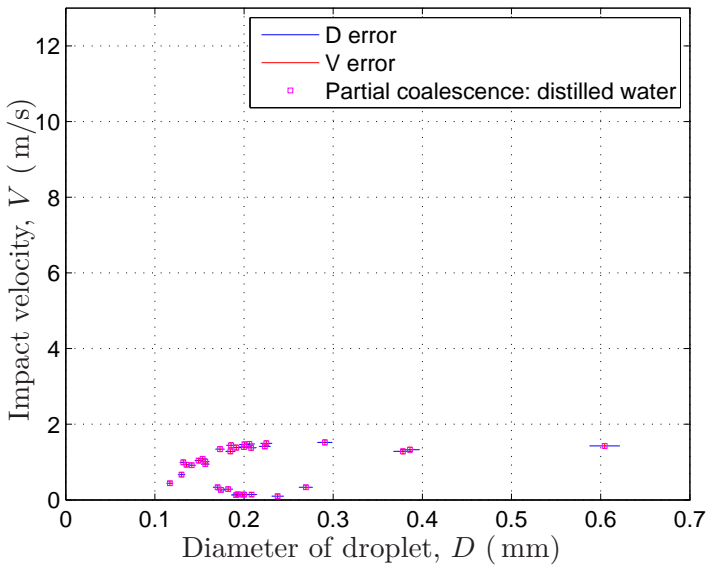
Figure 5.18: Partial coalescence of distilled water: velocity (V) versus diameter (D).

Table 5.4: Information of fundamental parameters from bouncing.

Fluid	D (mm)	$\frac{\Delta D}{D}(\pm\%)$	V (m/s)	$\frac{\Delta V}{V}(\pm\%)$	Measurements
Distilled water	0.12-0.60	2.75-2.81	0.01-1.5	4.46-55.71	33
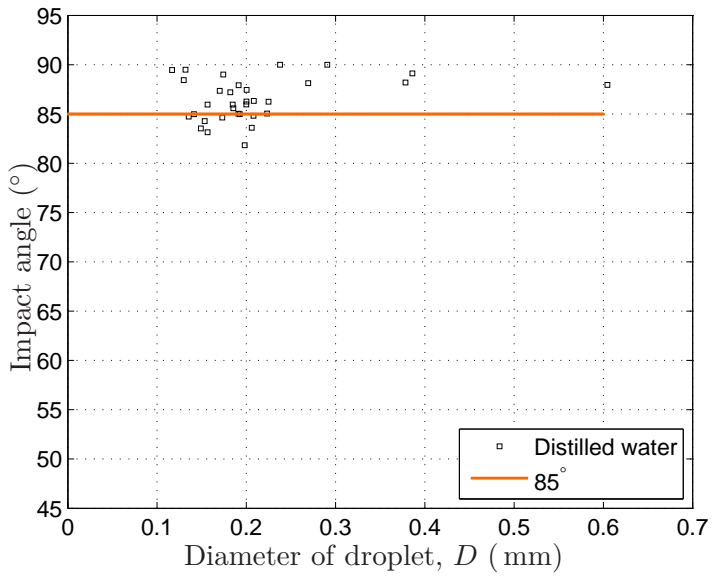
(a) Impact angle.
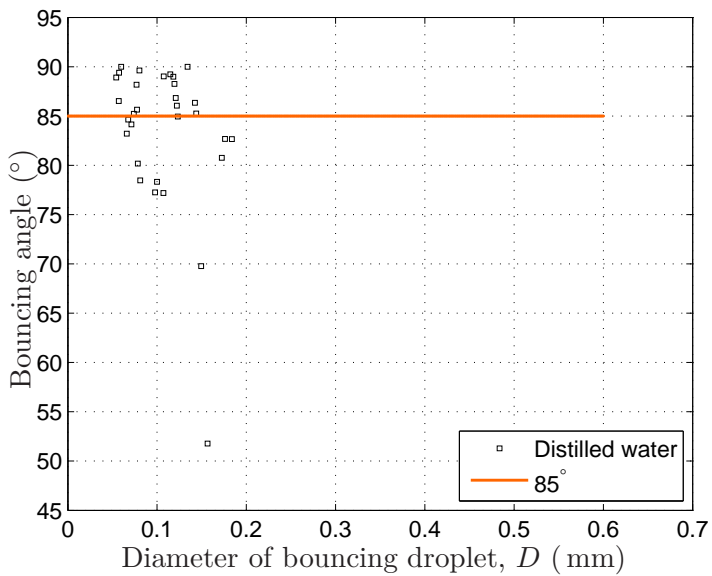
(b) Bouncing angle.

Figure 5.19: Impact and bouncing angles from partial coalescence.

5.6 Summary of the Chapter

This chapter first gives an overview of the distribution of different regimes, and the observations and data are presented according to the energy level from high to low.

- Jetting: 4 types of observations, corresponding to swelling wave, crown formation, crown breaking, central jet and secondary droplets, are described. The diameter and velocity from experiments with 5 fluids, distilled water, technical ethanol, n-pentane, methanol and 1-propanol, are presented. The relative uncertainties for diameter and velocity are low ($\approx 3\%$).

- Coalescence: 2 types of observations, corresponding to high-energy and low-energy collisions coalescence, are described. The diameter and velocity from experiments with 5 fluids, distilled water, technical ethanol, n-pentane, methanol and 1-propanol, are presented. The relative uncertainties can reach a high level (up to 50%) which corresponds to very low velocity ($\approx 0.1\,\mathrm{m/s}$).

- Bouncing: One type of observation is described. The diameter and velocity from experiments with 3 fluids, distilled water, technical ethanol and 1-propanol, are presented.

- Partial coalescence: One type of observation is described. The diameter and velocity from experiments with distilled water is presented.

The general diameter range is from 0.1 mm to 0.7 mm, and the general velocity range is up to $10\,\mathrm{m/s}$.

Chapter 6

Data Analysis and Discussion

6.1 Introduction

The main focus of this chapter is to characterize the thresholds between different regimes. The effects of the physical properties and droplet diameter on the thresholds are also discussed.

Two regression methods, which were used for determining the curve-fitted models, are introduced at the beginning of this chapter.

The first threshold is between coalescence and jetting. The threshold characterization of coalescence-jetting comprises two parts:

- To establish a mathematical model to describe the threshold.

- To determine the threshold level for the model.

Two models are suggested for characterizing the threshold between coalescence and jetting for five fluids, and the possibility for applying the models to other fluids is given. The first model is described by the Weber number (We) and the Ohnesorge number (Oh), and a correction term must be used to achieve good characterizations. The second model is described by the Froude number (Fr) and the Capillary number (Ca).

Based on the observation differences, the effects of kinetic parameters (diameter and velocity) and physical properties (viscosity, surface tension and density) on the formation of a crown are discussed.

The second threshold is between the regime of coalescence and the regime of bouncing. Strictly, there are two thresholds between coalescence and bouncing. The main focus is the transition from bouncing to high-energy collision coalescence, but an attempt to characterize the transition between low-energy collision coalescence to bouncing is also made. As the two thresholds are located at a very low energy level and they are sensitive to parameter changes such as diameter and velocity, it is found that the

thresholds can be well characterized by using the Weber number. A comparison between the threshold levels in this work and thresholds from the literature is also made.

Based on the characterized thresholds, the effects from the physical properties on the threshold level are discussed.

In order to study the energy loss in bouncing, the restitution coefficient is investigated, and the effects of the physical properties on the stable level of restitution coefficient are discussed.

6.2 Regression Methods

Two regimes can be separated by a threshold of a mathematical expression, and in order to find the most suitable threshold proper regression methods need to be applied. Two regression methods applied in the present work are described in this section.

Before introducing the two regression methods, two definitions regarding the data points, which are in regimes separated by a threshold line, must be clarified:

- Uncertain points: The data points of one regime found in a range where the majority of points are from another regime.

- Certain points: The data points of one regime found in a range where the majority of points are from the same regime.

Figure 6.1 shows an example which contains two regimes, Regime 1 and Regime 2, and a threshold is needed for dividing the two regimes. The threshold line represents the transition from one regime to another. The two regression methods based on different judgment rules are:

- Least points method: As shown in the figure, the least points method (blue solid line) divides the two regimes with the least uncertain points. The threshold line characterized by this method is able to separate the two regimes into two divisions with the least number of uncertain points, which are one red cross and four green circles.

- Least squares method: The least squares method (blue dashed line), generally, minimizes the sum of squares between the uncertain points and the threshold line. The threshold line, which is characterized by this method, gives the minimum sum of the squares of the distances, such as D_1-D_4, which are between the uncertain points and the threshold line. Compared with the least points methods, more uncertain points may be found by this method. This method stresses the
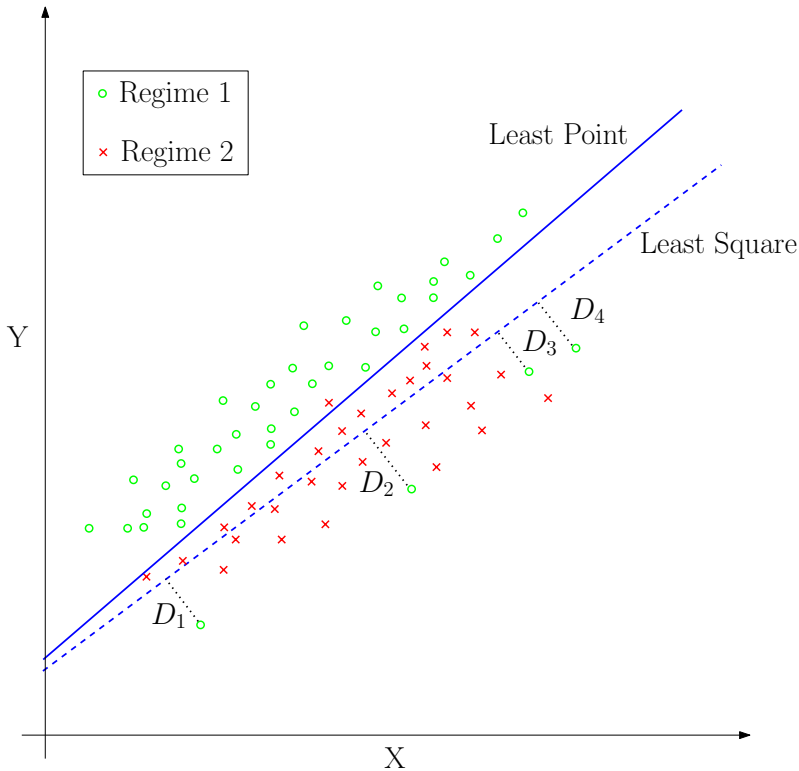
Figure 6.1: An example of data regression for finding the threshold between two regimes.

minimum sum of squares, and it keeps a certain balance with regard to the number of points since the minimum sum of squares is always reached with a few number of uncertain points. This method becomes problematic if there are uncertain points, which are located far from their dominant regime, and those uncertain points may be generated with large experimental uncertainties, such as D_1-D_4 shown in the figure. The large number of green circles deviating far from the real threshold drag the threshold to the dashed line and many uncertain points (red crosses) are included as the least squares method tends to minimize the distance squares to the green circles and neglects the many red crosses which are close to the threshold. However, if those points with large uncertainties are not present, the two methods should be nearly equivalent, and the least squares method is even superior to the least points method as it tends to reduce the possible uncertainties adjacent to the threshold.

In order to determine between two regression methods, the number of uncertain points from the two regression methods need to be compared. Without having points with large uncertainty, the numbers of uncertain points from two methods should be close. If the difference of the uncertain points from the two methods is less than 10 (approximately 1% of the total number), the two methods are considered nearly equivalent, and the results from the least squares method are used. Otherwise, it indicates that there are points with large uncertainties, and the results from the least points method are used to avoid the problem shown in Figure 6.1.

6.3 Coalescence-Jetting Threshold Characterization using the Weber Number (We) and the Ohnesorge Number (Oh)

6.3.1 Hypothesis of the Exponents for Expressing the Threshold

The transition from coalescence to jetting occurs at a high inertial energy level, and the inertia is dominant when compared other mechanisms such as gravity, viscosity and surface tension. Parameters indicating the inertia must be included in the mathematical model to characterize the threshold. As described in Section 2.3, the dimensionless parameters which include the inertia are the Weber number (We), the Reynolds number (Re), the Froude number (Fr). Other mechanisms such as viscosity and surface tension can be indicated by using the Ohnesorge number (Oh) or the Capillary number (Ca).

As described in Section 2.6.1, the most commonly used dimensionless parameters are the Weber number and the Ohnesorge number. The first model for characterizing the coalescence-jetting threshold is based on the relation between the Weber number and the Ohnesorge number.

6.3.2 Raw Data and Models in Literature

This section shows the raw data of the Weber number and the Ohnesorge number for five fluids (distilled water, technical ethanol, n-pentane, methanol and 1-propanol) in coalescence and jetting. The Weber number is plotted against the Ohnesorge number, and for the clearness of the plots, only part of the data points from different levels are shown with error bars.

In addition, the models characterizing the threshold between coalescence and jetting (Hsiao et al. 1988, Huang & Zhang 2008) are plotted in the figures by using dashed lines.

The raw data and literature models for distilled water, technical ethanol, n-pentane, methanol and 1-propanol are displayed in Figure 6.2(a), (b), (c),
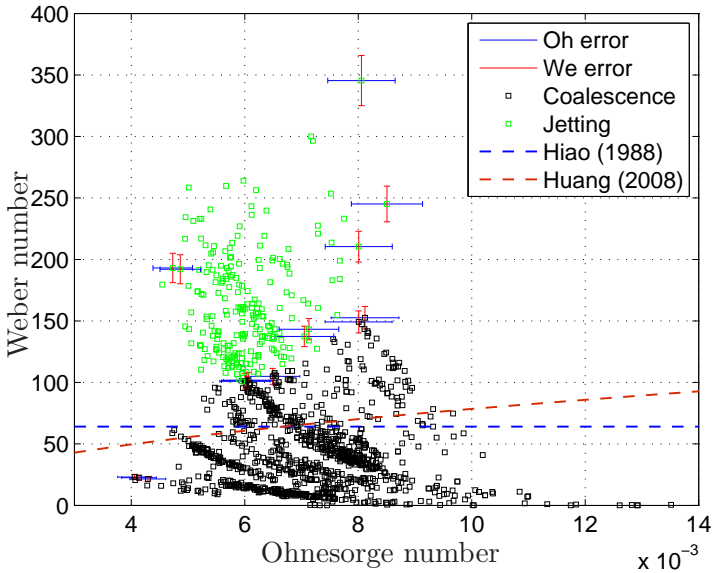
(a) Distilled water
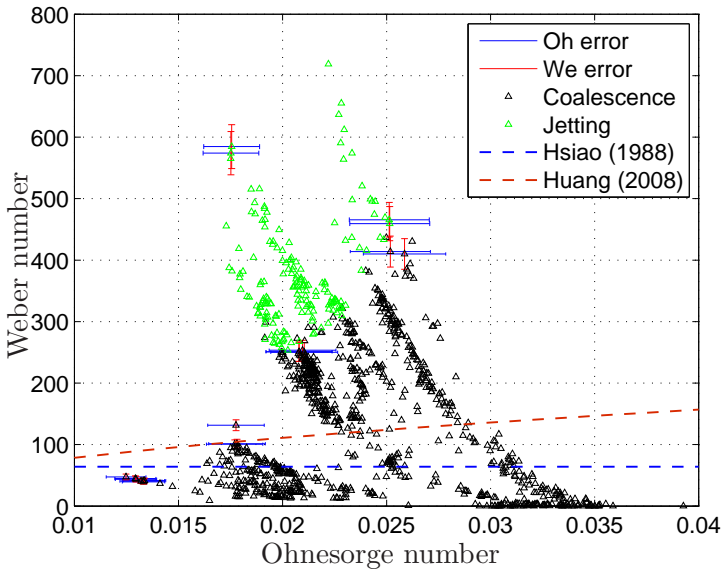
(b) Technical ethanol

Figure 6.2: Raw data: We- Oh in the cases of coalescence and jetting.

(d) and (e), respectively. The empirical models are described in Section 2.6.
The ranges and uncertainties of the Weber number and the Ohnesorge
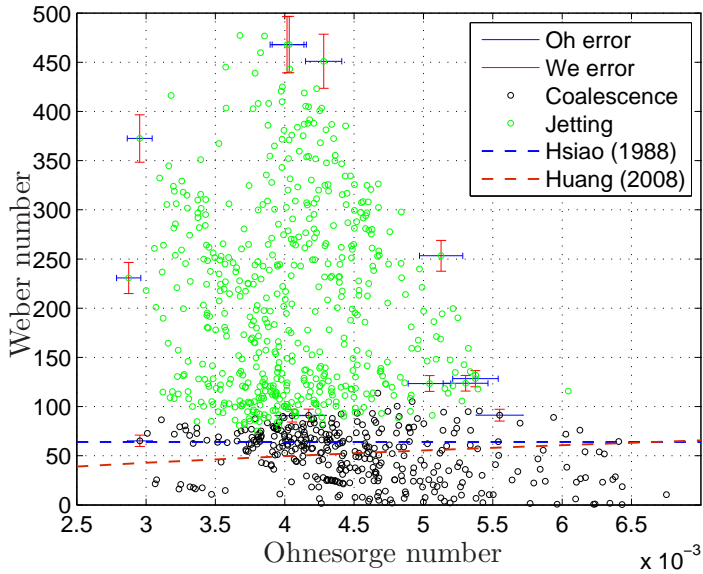
(c) n-pentane
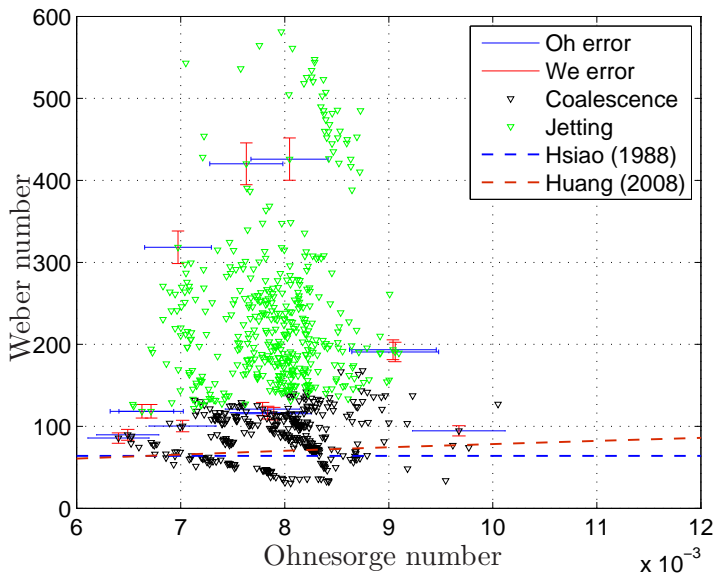
(d) Methanol

Figure 6.2: Raw data: We-Oh in the cases of coalescence and jetting. (Continued)

(e) 1-propanol
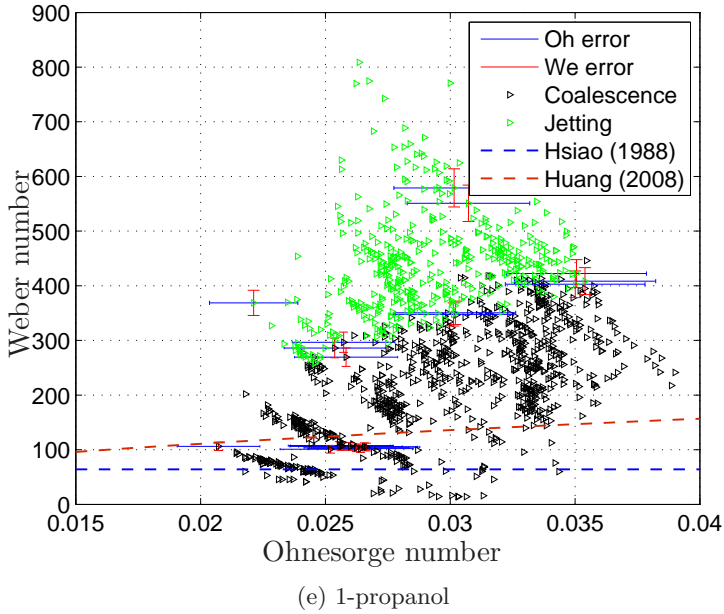
Figure 6.2: Raw data: We- Oh in the cases of coalescence and jetting. (Continued)

number are shown in Table 6.1. It is noted that the Weber number uncertainty, $\frac{\Delta\text{We}}{\text{We}}$, reaches a high level in coalescence, and as explained in Section 5.3.2, this level is associated with a very few number of data with extremely low velocities. Except this few number of data, most of the Weber number uncertainties, $\frac{\Delta\text{We}}{\text{We}}$, are around 6%-7%, and all of the Ohnesorge number uncertainties, $\frac{\Delta\text{Oh}}{\text{Oh}}$ are below 8%.

Discrepancies between the Literature Models and the Experimental Data

Figure 6.2(a)-(e) show that there are discrepancies between the experimental data and the models in the literature. The possible reasons for the discrepancies are listed as follows.

- Fluid discrepancy: Hsiao et al. (1988) used mercury, and Huang & Zhang (2008) focused on water and oil. In the present work, the experimental fluids cover distilled water, three different alcohols (methanol, the technical ethanol, and 1-propanol), and one hydrocarbon (n-pentane). The physical properties of the fluids in the present work vary distinctively from the others. For instance, the surface

Table 6.1: Raw data: We vs. Oh.

Fluid	Regime	We	$\frac{\Delta\,\text{We}}{\text{We}}$ ($\pm\%$)	Oh	$\frac{\Delta\,\text{Oh}}{\text{Oh}}$ ($\pm\%$)
Distilled water	Coalescence	0-153	6.0-104.1	0.004-0.015	7.4-7.4
Distilled water	Jetting	101-345	5.9-6.3	0.005-0.009	7.4-7.4
Technical ethanol	Coalescence	0-437	6.1-102.1	0.012-0.039	7.6-7.7
Technical ethanol	Jetting	254-719	6.0-6.3	0.017-0.025	7.6-7.6
n-pentane	Coalescence	0-114	6.5-38.5	0.003-0.007	3.0-3.1
n-pentane	Jetting	75-477	6.1-7.8	0.003-0.006	3.0-3.1
Methanol	Coalescence	31-168	6.3-8.5	0.006-0.010	4.6-4.6
Methanol	Jetting	118-581	6.0-7.0	0.007-0.009	4.6-4.6
1-propanol	Coalescence	14-446	6.0-10.3	0.020-0.039	8.0-8.0
1-propanol	Jetting	259-809	6.0-6.3	0.022-0.035	8.0-8.0

tension in the present work is much lower than for mercury, and the viscosity is much lower than for oil.

- Size discrepancy: The present work focuses on the diameter range approximately 0.1-0.7 mm. Hsiao et al. (1988) did not point out the diameter explicitly, and Huang & Zhang (2008) used a millimetric-level which was larger than 1 mm.

As the models in the literature do not fit well with the experimental data, a new model is needed.

Model Assumption for Coalescence-Jetting Threshold

Even though discrepancies are found between different models and the experimental data, the establishment of the empirical model for the experimental data benefits from the models in the literature because the formations of different models are found to be quite similar if the original models are converted into expressions by using the Weber number and the Ohnesorge number. The original models and derivations, from both droplet-pool and droplet-film interactions, are shown in Table 6.2.

Based on the derivations of different models, a threshold model for the

experimental data in the present work can be assumed to be in the form,

$$\text{We} \cdot \text{Oh}^{\hat{\alpha}} = \hat{\beta}, \tag{6.1}$$

where $\hat{\alpha}$ and $\hat{\beta}$ are constants. However, this relation, Eq. (6.1), is found not good enough to describe the sharp threshold changes for the data from the fluids with relatively high viscosities such as distilled water, technical ethanol and 1-propanol. Thus, a model with a correction term is presented as follows,

$$\text{We} \cdot \text{Oh}^{\hat{\alpha}+\frac{\hat{\gamma}}{D}} = \hat{\beta}, \tag{6.2}$$

where D is the diameter of a droplet and $\hat{\gamma}$ is a reference diameter. The correction term, $\frac{\hat{\gamma}}{D}$, is dominant and influential as the diameter gets smaller. The model with correction, Eq. (6.2), can well characterize the thresholds with few number of uncertain points. Even though the values of $\hat{\alpha}$ and $\hat{\beta}$ vary according to the regression methods and fluids, it is found that the threshold characterizations are reasonably good by using fixed values of $\hat{\alpha}$ and $\hat{\beta}$ for different fluids. The model is written as

$$\text{We} \cdot \text{Oh}^{-0.57+\frac{\hat{\gamma}}{D}} = 1705, \tag{6.3}$$

where $\hat{\alpha} = -0.57$ and $\hat{\beta} = 1705$ are used, and jetting occurs as the threshold value is above 1705.

6.3.3 Threshold Model 1 Characterization: Determination of the reference diameter

In the model, Eq. (6.3), $\hat{\gamma}$ is the only variable which needs to be characterized. By using the two regression methods, the values of $\hat{\gamma}$ for different fluids are determined and listed in Table 6.3. The table also shows the numbers of the uncertain points from two regression methods.

Table 6.2: Empirical models and derivations.

Literature source	Original model	Derivations
Mundo et al. (1995)	$57.7 = \text{Oh} \cdot \text{Re}^{1.25}$	$\text{We} = \frac{654}{\text{Oh}^{-0.4}}$
Cossali et al. (1997)	$2100 = \text{We} \cdot \text{Oh}^{-0.4}$	$\text{We} = \frac{2100}{\text{Oh}^{-0.4}}$
Vander Wal et al. (2006*b*)	$63 = \text{Oh} \cdot \text{Re}^{1.17}$	$\text{We} = \frac{1191}{\text{Oh}^{-0.3}}$
Huang & Zhang (2008)	$28 = \text{We}^{0.375} \cdot \text{Re}^{0.25}$	$\text{We} = \frac{784}{\text{Oh}^{-0.5}}$

Table 6.3: reference diameter in threshold model 1, Eq. (6.3).

Fluid	Regression	$\hat{\gamma}(10^{-6})$	Uncertain points	$\frac{\text{Uncertain}}{\text{Total}}$
Distilled water	Point	7	11	0.80%
Distilled water	Square	10	14	1.12%
Technical ethanol	Point	25	23	2.14%
Technical ethanol	Square	28	35	3.25%
n-pentane	Point	7	29	3.24%
n-pentane	Square	8	30	3.35%
Methanol	Point	11	17	2.12%
Methanol	Square	14	27	3.36%
1-propanol	Point	28	59	4.60%
1-propanol	Square	29	62	4.83%

The thresholds by using the model, Eq. (6.3), with the characterized term, $\hat{\gamma}$, listed in Table 6.3, are shown in Figure 6.3(a), (b), (c), (d) and (e), which correspond to distilled water, technical ethanol, n-pentane, methanol and 1-propanol, respectively. In the Figure, the dash-dotted curves, Threshold$_S$ and Threshold$_P$, are the thresholds characterized by the least squares and the least points methods, respectively.

As described in Section 6.2, the uncertain points which are located far from the threshold tend to drag the threshold curves by least squares method, and this leads to the deviation to the threshold curves by the least points methods. For determining the value of $\hat{\gamma}$, the numbers of uncertain points from two methods are compared. If the variation between the two methods are within 10 points, the results from the least squares method are chosen. Otherwise, the results from the least points method is chosen. The chosen values of $\hat{\gamma}$ are listed in Table 6.4.
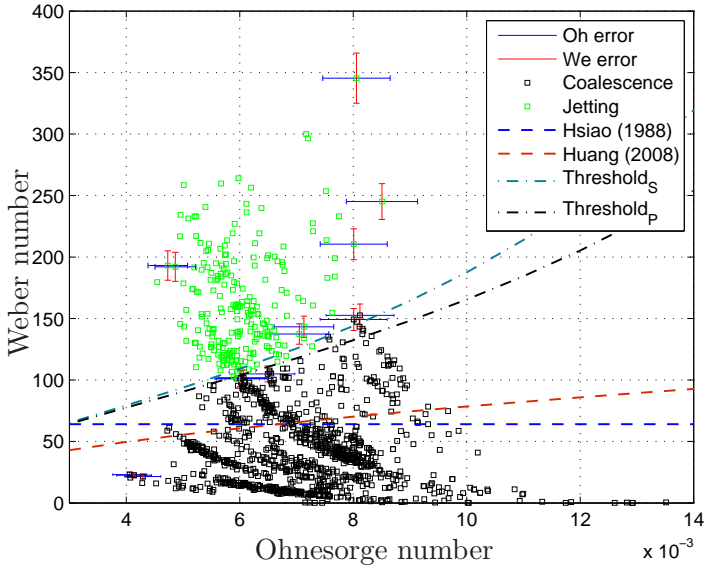
(a) Distilled water
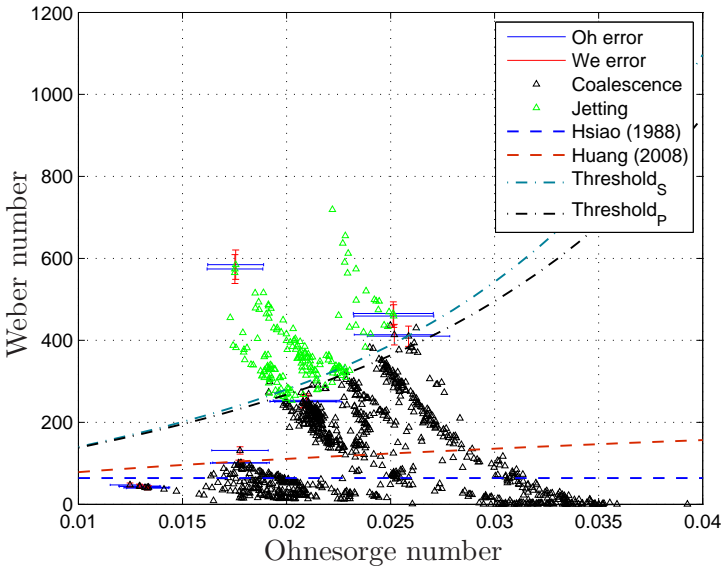
(b) Technical ethanol

Figure 6.3: Thresholds of coalescence-jetting characterized by the simplified threshold model 1 Eq. (6.3).
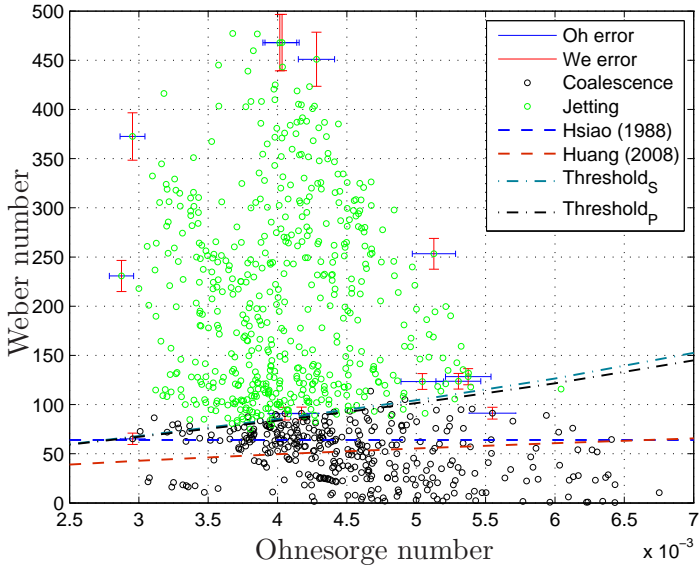
(c) n-pentane
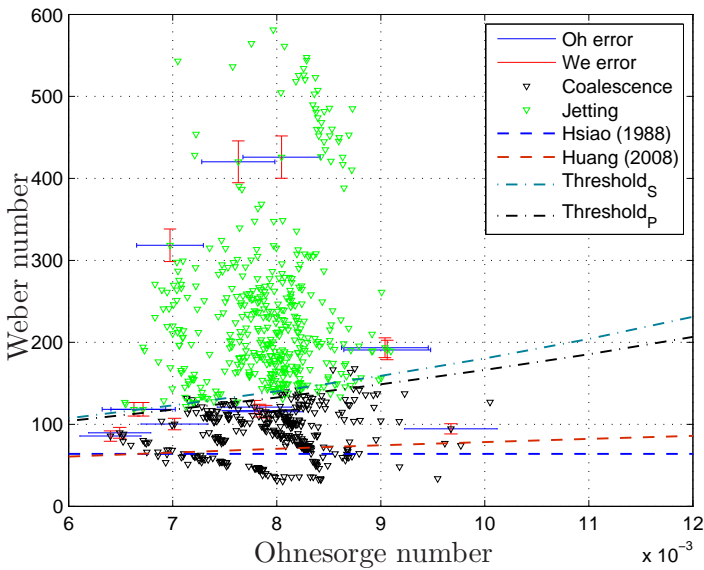
(d) Methanol

Figure 6.3: Thresholds of coalescence-jetting characterized by the simplified threshold model 1 Eq. (6.3). (Continued)
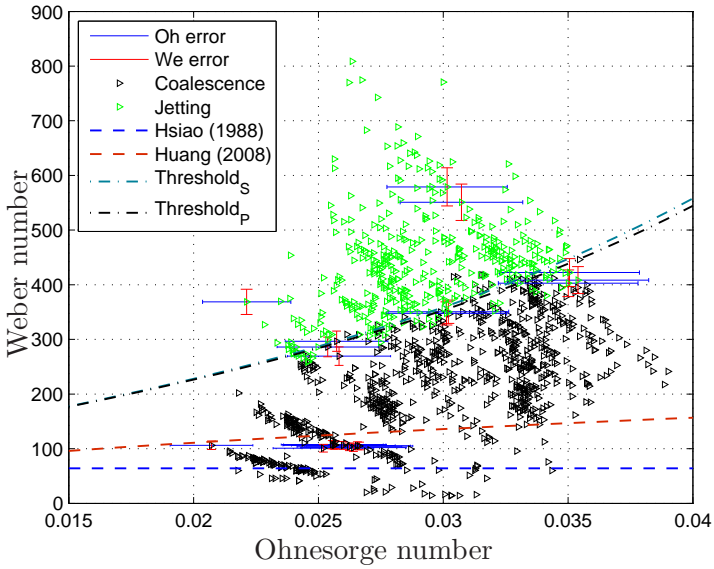
(e) 1-propanol

Figure 6.3: Thresholds of coalescence-jetting characterized by the simplified threshold model 1 Eq. (6.3). (Continued)

Table 6.4: Chosen values of $\hat{\gamma}$ in threshold model 1, Eq. (6.3).

Fluid	$\hat{\gamma}(10^{-6})$
Distilled water	10
Technical ethanol	25
n-pentane	8
Methanol	14
1-propanol	29

6.3.4 Comparison between Threshold Model 1 and Literature Data

The discrepancies between the threshold of the present work and the literature models are described in Section 6.3.2, and the two reasons for the discrepancies are assumed to be the difference in diameter and fluids. In this section, as threshold model 1 is characterized, an attempt is made to compare threshold model 1 with the literature data to investigate if threshold model 1 can characterize the threshold the literature data, which had diameter and velocity range differing from those of the present work.

Figure 6.3(a) shows that the curve of threshold model 1 intersects the line of Hsiao et al.'s (1988) model when $Oh \approx 0.003$, and it approaches the curve of Huang & Zhang's (2008) model as the Ohnesorge numbers decreases, i.e. the diameter increases. This indicates that threshold model 1 has the possibility to characterize the literature data, which is of larger diameter.

The diameter and velocity information is not explicitly given by Hsiao et al. (1988) and Huang & Zhang (2008), and as described, the fluids are different. Thus, these limitations make the direct comparison of threshold model 1 with the literature data difficult.

Rodriguez & Mesler (1985) did not present a mathematical model for the coalescence-jetting threshold, however, the threshold data of velocity and diameter was plotted in their figure. Rodriguez & Mesler's (1985) threshold data are of larger diameter (above 1 mm) than the data of the present work (0.1-0.7 mm), and the complementary threshold data can be used to test the applicability of threshold model 1. Another advantage of using their data is that their experimental fluid, water, coincides with one of the experimental fluids in the present work. The threshold diameter and velocity extracted from their figure are

$$
\begin{aligned}
D &= [1.2, 2.0, 2.5^1, 2.8]\,\text{mm} \\
V &= [2.05, 1.5, 1.2^1, 1.1]\,\text{m/s}.
\end{aligned}
\tag{6.4}
$$

Figure 6.4 includes the threshold data from Rodriguez & Mesler (1985). The good fit of threshold model 1 with the literature threshold data indicates that threshold model 1 is able to characterize the coalescence-jetting threshold with a wider range of droplet diameters than obtained from the experiments of the present work. Compared to the other two literature models (Hsiao et al. 1988, Huang & Zhang 2008), threshold model 1 shows

---

[1]From Thomson & Newall (1885) and extracted from the investigation of Rodriguez & Mesler (1985)
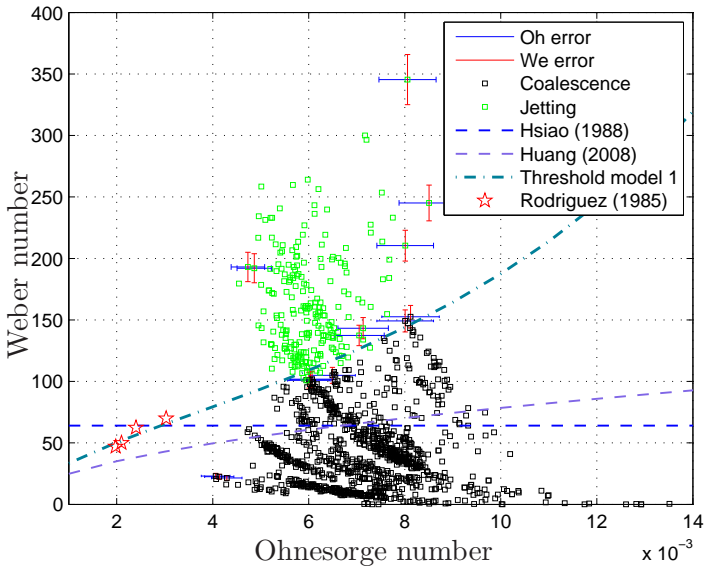
Figure 6.4: Comparison of threshold model 1 with the threshold data from Rodriguez & Mesler (1985) for distilled water.

better characterization of the threshold variation as the Ohnesorge number decreases, i.e. as the droplet diameter increases. In conclusion, threshold model 1 can well-characterize the coalescence-jetting threshold within the range of diameter and velocity in the present work, and the good fit with Rodriguez & Mesler (1985) indicates that this model has a good potential to characterize jetting at larger droplet diameters and lower velocities.

6.3.5 Deduction of Generalized Threshold Model 1 for An Uncharacterized Fluid

In the exponential model, Eq. (6.3), the reference diameter, $\hat{\gamma}$, varies according to fluids. For predicting the threshold for an uncharacterized fluid, this variable must be obtained through the experiment, and this section gives a way to calculate this variable.

The variation of $\hat{\gamma}$ between different fluids must be related with the experimental conditions which include:

- Experimental fluid.

- Ambient gas.

- Temperature and pressure.

- Impact angle.

Among those conditions, the following assumptions can be made:

- The impact angle variation can be neglected as all the angles were maintained well around $90°$.

- The variation of the ambient gas is for the experiments with n-pentane, where the gas is pure n-pentane vapor, and the ambient gas for the other fluids is air saturated with the vapors of experimental fluids. The ambient gas changes the friction and the buoyancy during the falling of a droplet, both of which are linked to the gas density which is much lower than the density of liquid. So, it is assumed that the effects from the ambient gas can be neglected.

- The variation of temperature and pressure is for the experiments with n-pentane, and the temperature and pressure basically change the physical properties of the liquids.

- The variation of the experimental fluids also changes the physical properties of the fluid.

For summarizing, the variation of the liquid properties is assumed to be the main cause for the variation of $\hat{\gamma}$.

$\hat{\gamma}$ can be assumed to be influenced primarily by the density (ρ), viscosity (μ) and surface tension (σ) of liquid. More specifically, the expression of $\hat{\gamma}$ for an uncharacterized fluid x can be written as

$$\frac{\hat{\gamma}_x}{\hat{\gamma}} = (\frac{\rho_x}{\rho})^{A_{\hat{\gamma}}} \cdot (\frac{\mu_x}{\mu})^{B_{\hat{\gamma}}} \cdot (\frac{\sigma_x}{\sigma})^{C_{\hat{\gamma}}}, \tag{6.5}$$

where the variables with the subscript, x, denotes the quantities from the uncharacterized fluid, and $A_{\hat{\gamma}}$, $B_{\hat{\gamma}}$ and $C_{\hat{\gamma}}$ are the exponents for density, viscosity and surface tension, respectively. The reference liquid properties, ρ, μ and σ, are the properties of 1-propanol.

By the trial and error method, the following solution is found:

$$\frac{\hat{\gamma}_x}{\hat{\gamma}} = (\frac{\rho_x}{\rho})^{1.82} \cdot (\frac{\mu_x}{\mu})^{0.6} \cdot (\frac{\sigma_x}{\sigma})^{-0.96}. \tag{6.6}$$

The trial ranges for the exponents, A, B and C, are $[-8, 8]$, $[-2, 2]$ and $[-2, 2]$, correspondingly, and the step sizes are set to 0.02. The trial and error method gives a number of solutions with good margins to the trial ranges, and the solutions make reasonable predictions of the reference diameter. The best solution is chosen from those solutions according to the

Table 6.5: Comparison of the values from the least squares method and the calculation method using Eq. (6.6) with model 1.

Fluid	$\hat{\gamma}(10^{-6})$	Uncertain points	$\frac{\text{Uncertain}}{\text{Total}}$
Distilled water (S)	10	14	1.12%
Distilled water (C)	9.1	12	0.96%
Technical ethanol (S)	25	35	3.25%
Technical ethanol (C)	24.5	25	2.32%
n-pentane (S)	8	30	3.35%
n-pentane (C)	7.3	28	3.13%
Methanol (S)	14	27	3.36%
Methanol (C)	13.7	22	2.74%
1-propanol (S)	29	62	4.83%
1-propanol (S)	29	62	4.83%

rule that the best solution gives the minimum root sum square (RSS) of the uncertain points numbers for all fluids.

By using the calculation method, the characterizations of coalescence-jetting threshold were made, and these characterizations were compared with the characterizations using the experimental-fitting method (least squares). The comparison is shown in Table 6.5. The values of $\hat{\gamma}$, uncertain points and $\frac{\text{Uncertain}}{\text{Total}}$ from the experimental-fitting method and the calculation method (Eq. (6.6)) are listed in the table. "(S)" and "(C)" denote the least squares method and the calculation method, respectively. Compared to the experimental-fitting method, the calculation method gives less uncertain points but higher sum of square, and it indicates that by the calculation method, the characterization is reasonable as the number of uncertain points is between the two experimental-fitting methods, i.e. more than least points and less than least squares.

6.4 Coalescence-Jetting Threshold Characterization Using the Froude Number (Fr) and the Capillary Number (Ca)

The exponential model, Eq. (6.3), can characterize the threshold between coalescence and jetting well. However, the reference diameter, $\hat{\gamma}$, for fitting the shape threshold change for high viscosity fluids must be used. In this section, a new linear model using the Froude number and the Capillary number is proposed, and this model can characterize the thresholds well with comparison to the exponential model.

6.4.1 Hypothesis of the Components for Expressing the Threshold

Instead of using the Weber number to evaluate the effects from the inertia, the Froude number is used in the new model. The Froude number, Eq. (2.5), also includes the effect of the gravity, which is not present in the dimensionless parameters in the exponential model, Eq. (6.3).

As described in Chapter 2, theoretically, a complicated physical process can be described by using a complete set of dimensionless parameters which include all the effects in the process. Besides the Froude number, another dimensionless parameter, which includes the viscosity and surface tension is needed. The Capillary number, Eq. (2.6), covering both effects is used in the new model.

6.4.2 Raw Data: the Froude Number and the Capillary Number

This section shows the raw data of the Froude number and the Capillary number for five fluids in coalescence and jetting. The Froude number is plotted against the Capillary number, and for the clearness of the plots, only part of the data points from different levels are shown with error bars.

The raw data from distilled water, technical ethanol, n-pentane, methanol and 1-propanol are displayed in Figure 6.5(a), (b), (c), (d) and (e), respectively.

The ranges and uncertainties of the Froude number and the Capillary number are shown in Table 6.6.

As the Capillary number also includes the velocity term, the Capillary number uncertainty, $\frac{\Delta \mathrm{Ca}}{\mathrm{Ca}}$, goes to a high level at low velocities. Comparing between Table 6.6 with Table 6.1, it can be found that the Capillary number uncertainties, $\frac{\Delta \mathrm{Ca}}{\mathrm{Ca}}$, are of the similar level of the Ohnesorge number uncertainties, $\frac{\Delta \mathrm{Oh}}{\mathrm{Oh}}$, while the Froude number uncertainties, $\frac{\Delta \mathrm{Fr}}{\mathrm{Fr}}$ are smaller than the Weber number uncertainties, $\frac{\Delta \mathrm{We}}{\mathrm{We}}$. The reason for less uncertainty in

Table 6.6: Raw data: Fr vs. Ca.

Fluid	Regime	Fr	$\frac{\Delta \text{Fr}}{\text{Fr}}$ ($\pm\%$)	Ca	$\frac{\Delta \text{Ca}}{\text{Ca}}$ ($\pm\%$)
Distilled water	Coalescence	2-202	3.0-52.1	0.001-0.100	7.7-52.6
Distilled water	Jetting	68-297	2.9-3.2	0.055-0.150	7.7-7.8
Technical ethanol	Coalescence	4-232	3.0-51.0	0.007-0.544	8.0-51.6
Technical ethanol	Jetting	97-222	3.0-3.1	0.315-0.595	7.9-8.0
n-pentane	Coalescence	7-108	3.2-19.3	0.004-0.056	4.0-19.4
n-pentane	Jetting	34-136	3.0-3.9	0.031-0.091	3.8-4.5
Methanol	Coalescence	35-113	3.1-4.2	0.045-0.113	5.2-5.9
Methanol	Jetting	47-167	3.0-3.5	0.072-0.194	5.1-5.4
1-propanol	Coalescence	27-220	3.0-5.1	0.11-0.75	8.3-9.3
1-propanol	Jetting	77-224	3.0-3.1	0.40-0.83	8.3-8.3

the Froude number is that the Froude number, Eq. (2.5), does not include the physical properties, and this is also an advantage of using the Froude number as one parameter in the coalescence-jetting model.
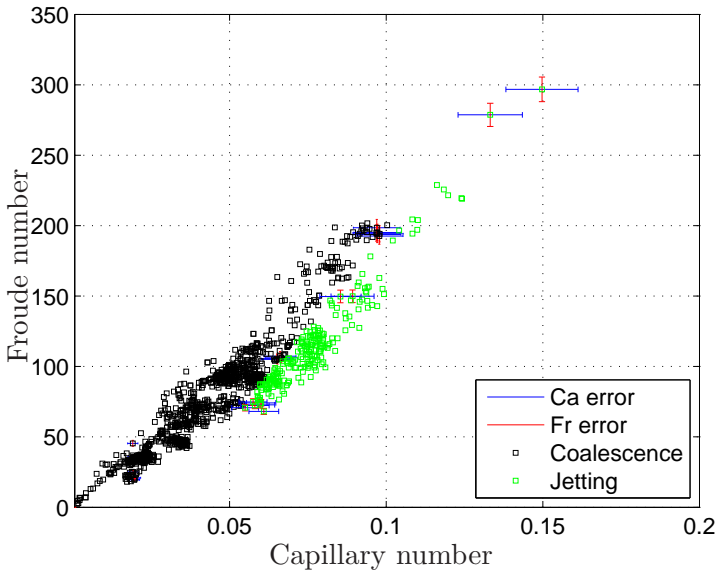
(a) Distilled water
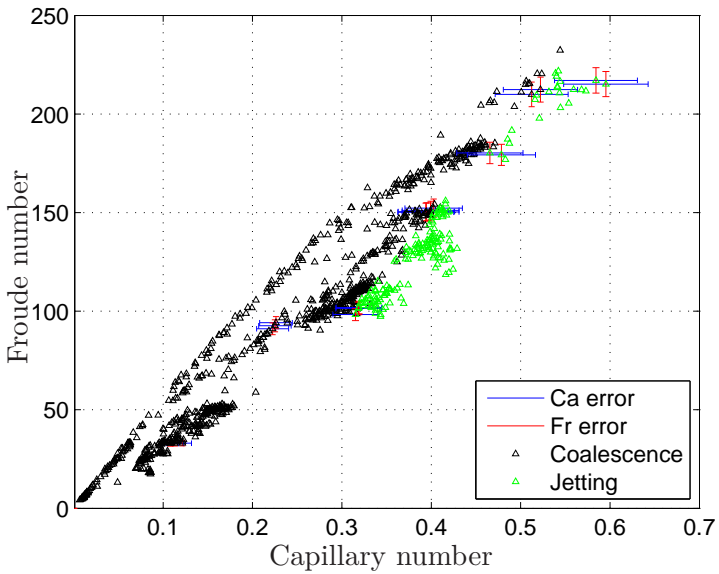
(b) Technical ethanol

Figure 6.5: Raw data: Fr- Ca in the cases of coalescence and jetting.
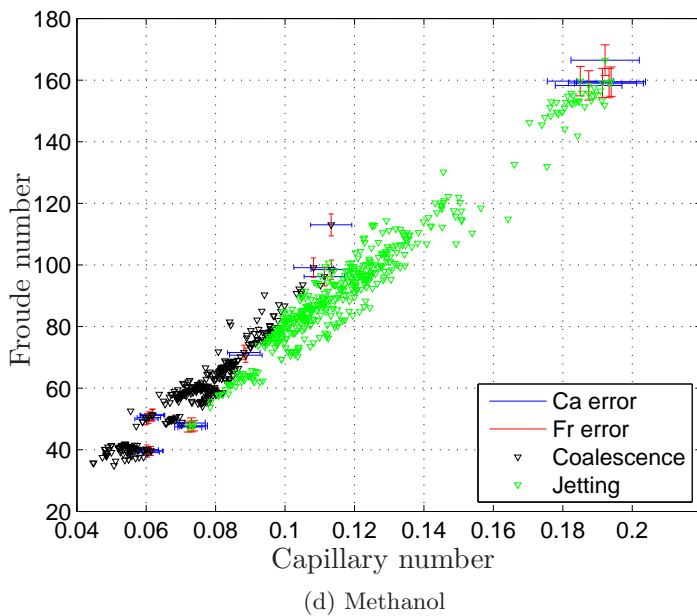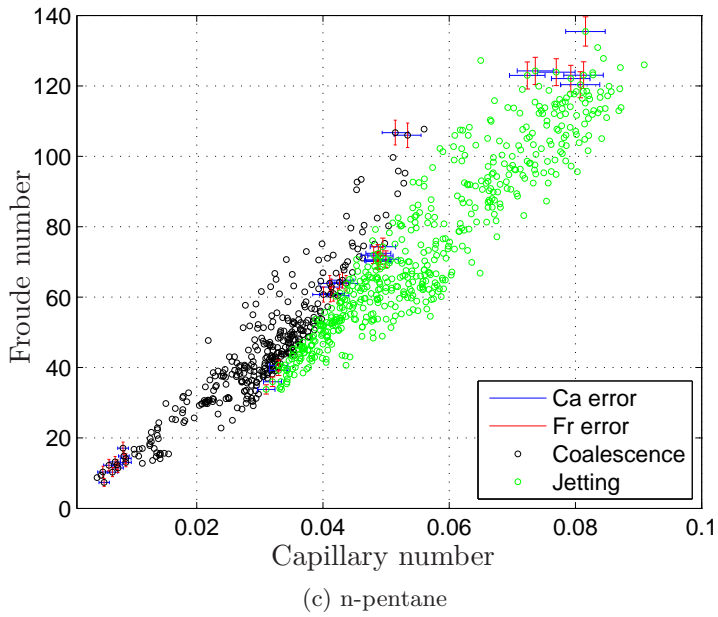
(c) n-pentane

(d) Methanol

Figure 6.5: Raw data: Fr- Ca in the cases of coalescence and jetting. (Continued)

(e) 1-propanol
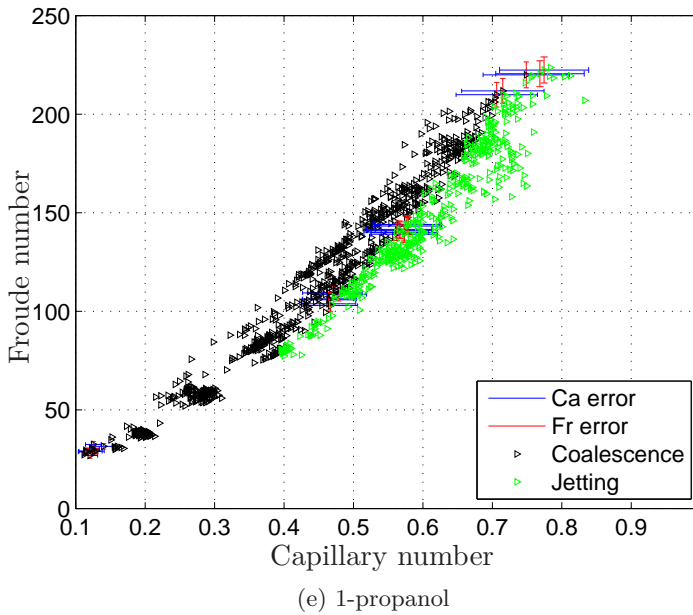
Figure 6.5: Raw data: Fr- Ca in the cases of coalescence and jetting. (Continued)

6.4.3 Threshold Model Assumption

It can be seen in Figure 6.5(a)-(e) that there is a clear distinction between the two regimes, and this is important for finding a mathematical expression to separate the two regimes.

As shown in the figures, the two regimes can be reasonably divided by a linear relation between the Froude number and the Capillary number, and the linear model is written as

$$\mathrm{Fr}_{\mathrm{critical}} = \alpha \cdot \mathrm{Ca} + \beta, \tag{6.7}$$

where $\mathrm{Fr}_{\mathrm{critical}}$ is the critical value of Froude number at which the regimes transit from one to another, and α and β denote the slope and the intercept on y-axis of the line. For a given Capillary number, jetting occurs as the Froude number is below $\mathrm{Fr}_{\mathrm{critical}}$.

Two regression methods described in Section 6.2 are used to determine the most suitable α and β.

Table 6.7: Comparison of the slopes and the intercepts of threshold model 2, Eq. (6.7), obtained by using two regression methods.

Fluid	Regression	α	β	Uncertain points	$\frac{\text{Uncertain}}{\text{Total}}$
Distilled water	Point	2679	−73	1	0.08%
Distilled water	Square	2668	−72	3	0.24%
Technical ethanol	Point	529	−64	12	1.11%
Technical ethanol	Square	544	−71	21	1.95%
n-pentane	Point	2405	−41	27	3.02%
n-pentane	Square	2594	−48	30	3.35%
Methanol	Point	1349	−51	20	2.49%
Methanol	Square	1301	−47	25	3.11%
1-propanol	Point	402	−85	71	5.53%
1-propanol	Square	395	−80	79	6.16%

6.4.4 Threshold Model 2 for Coalescence-Jetting: Determination of the Slope and the Intercept

In threshold model 2, Eq. (6.7), the slope (α) and the intercept (β), need to be found.

By using the regression methods, the slope and the intercept in the linear threshold model can be found. The thresholds and data points from different experiment sets with distilled water, technical ethanol, n-pentane, methanol and 1-propanol are shown in Figure 6.6(a), (b), (c), (d) and (e) respectively.

In the figure, the legends Threshold$_S$ and Threshold$_P$ denote the thresholds characterized by using the least squares method and the least points method, respectively. By qualitatively comparing between the two thresholds for each fluid, it can be seen that the variation between them is relatively low.

The statistical information from the comparison of the two thresholds is presented in Table 6.7. The step size for the calculation of α and β is set to 1. The table shows the values of α and β, which are calculated by the two regression methods, and the relative uncertainties of α and β from one regression method to another are listed under $\Delta\alpha$ and $\Delta\beta$. The number of the uncertain points and its ratio to the total number of points are also listed in the table.
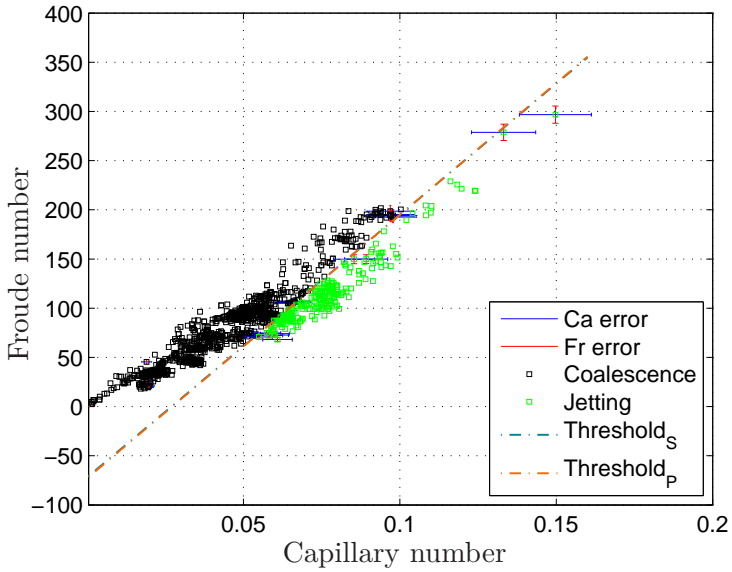
(a) Distilled water
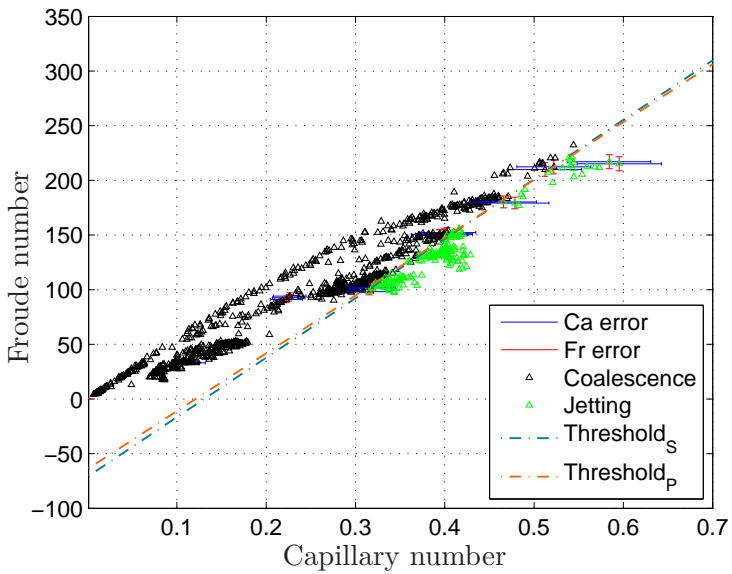
(b) Technical ethanol

Figure 6.6: Threshold 2 of coalescence-jetting characterized by using two regression methods.

(c) n-pentane

(d) Methanol

Figure 6.6: Threshold 2 of coalescence-jetting characterized by using two regression methods. (Continued)

(e) 1-propanol
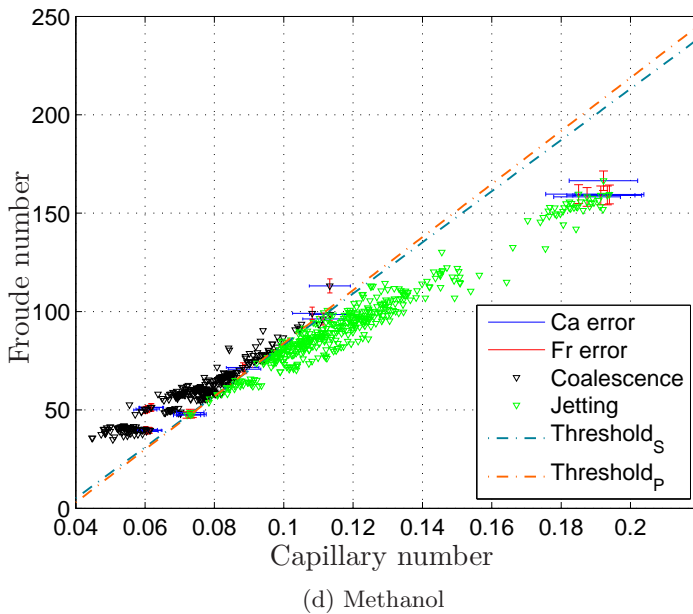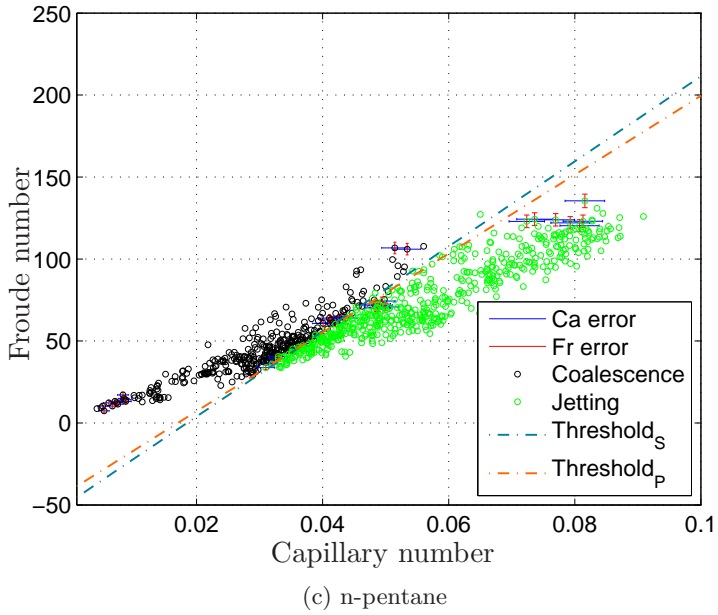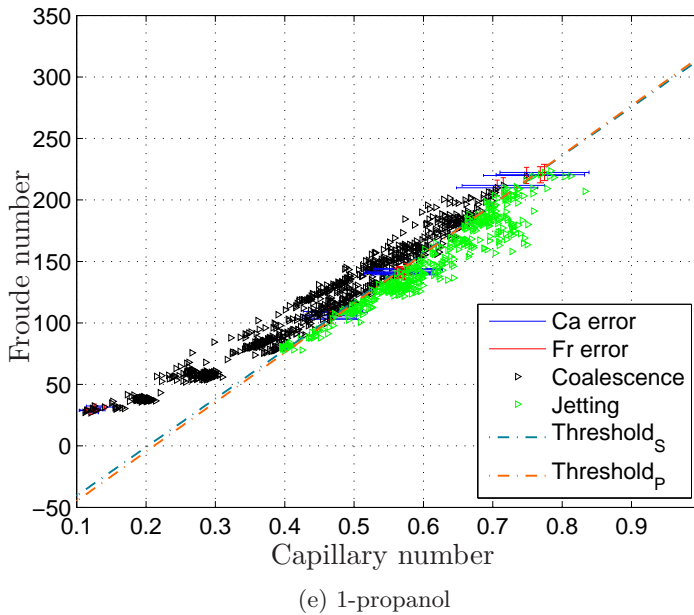
Figure 6.6: Threshold 2 of coalescence-jetting characterized by using two regression methods. (Continued)

The ratios of the number of uncertain points to the total number points indicate the quality of the thresholds, and low ratio corresponds to few number of uncertain points i.e. good quality. Among all cases, the ratios are maintained at low level, and the highest ratio is 6.16% corresponding to the case of 1-propanol. The low ratios show that both regression methods give satisfactory threshold characterizations.

A comparison between the percentage of uncertain points, $\frac{\text{Uncertain}}{\text{Total}}$, shows that the lowest uncertainty is from distilled water, and the highest uncertainty is from 1-propanol. The reason for this uncertainty differences depends on the ratio of jetting points to coalescence points, and the jetting points are with higher uncertainties than the coalescence points. The experiment with distilled water produces the second least number of jetting data points (230) and the most number of coalescence data points (1020), which give the lowest ratio of jetting points to coalescence points.

For determining the slopes and the intercepts, the same criterion as described in Section 6.3.3, can be used. The comparison between the results of the least squares and the least points shows that the differences between the numbers of the uncertain points for all fluids are within 10, and thus the results from the least squares method are chosen. The chosen results

Table 6.8: The chosen slopes and intercepts for threshold model 2, Eq. (6.7).

Fluid	α	β
Distilled water	2668	-72
Technical ethanol	544	-71
n-pentane	2594	-48
Methanol	1301	-47
1-propanol	395	-80

are listed in Table 6.8.

6.4.5 Comparison between the Threshold Model 2 and Literature Data

Similarly to Section 6.3.4, the coalescence-jetting threshold data from Rodriguez & Mesler (1985) for distilled water can be used for comparison with threshold model 2. Figure 6.7 includes the threshold data from Rodriguez & Mesler (1985).

The figure shows that the threshold data from Rodriguez & Mesler (1985) deviates from threshold model 2. This deviation indicates that, even though threshold model 2 can characterize the coalescence-jetting threshold well with relatively high Capillary number (within the Capillary number range of jetting), it has certain limitations for a lower range of the Capillary number, i.e. a lower level of velocity. Due to the small droplet size of the present work, jetting could not be generated with this low level of velocity. In conclusion, threshold model 2 can well characterize the jetting-coalescence threshold within certain ranges of diameter and velocity of the present work, however, the linear relation of threshold model 2 is not good enough for jetting with larger diameter and lower velocity.
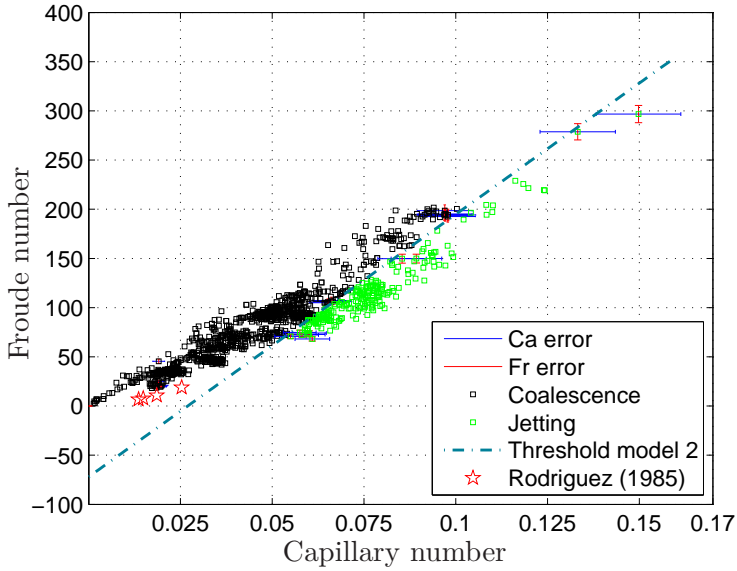
Figure 6.7: Comparison of threshold model 2 with the threshold data from Rodriguez & Mesler (1985) for distilled water.

6.4.6 Deduction of Generalized Threshold Model 2 for An Uncharacterized Fluid

In the linear model, Eq. (6.7), the slope and the intercept, α and β, vary according to fluids. Similarly to Section 6.3.5, this section proposes a way to calculate these variables, and the liquid properties are assumed to be the dominant factors for determining the variables.

The threshold models for all the experimental cases are obtained by inserting the values of α and β from the least squares method to Eq. (6.7). Even though the form of the models are the same, the expressions for different fluids vary. An attempt is made to use the characterized cases to predict the model for an uncharacterized fluid. The attempt gives a possible way to characterize the values of α and β of an uncharacterized fluid with the information from the known fluids.

α and β can be assumed to be the products of the density (ρ), viscosity (μ) and surface tension (σ). More specifically,

$$\frac{\alpha_x}{\alpha} = (\frac{\rho_x}{\rho})^{A_\alpha} \cdot (\frac{\mu_x}{\mu})^{B_\alpha} \cdot (\frac{\sigma_x}{\sigma})^{C_\alpha}, \tag{6.8}$$

$$\frac{\beta_x}{\beta} = (\frac{\rho_x}{\rho})^{A_\beta} \cdot (\frac{\mu_x}{\mu})^{B_\beta} \cdot (\frac{\sigma_x}{\sigma})^{C_\beta}, \tag{6.9}$$

where A, B and C are the exponents for density, viscosity and surface tension, respectively.

By the trial and error method, the following solution is found:

$$
\begin{aligned}
\frac{\alpha_x}{\alpha} &= (\frac{\rho_x}{\rho})^{-1.02} \cdot (\frac{\mu_x}{\mu})^{-0.99} \cdot (\frac{\sigma_x}{\sigma})^{1.20} \\
\frac{\beta_x}{\beta} &= (\frac{\rho_x}{\rho})^{-2.91} \cdot (\frac{\mu_x}{\mu})^{0.36} \cdot (\frac{\sigma_x}{\sigma})^{0.74}
\end{aligned}
\tag{6.10}
$$

The trial ranges for the exponents, A, B and C, were $[-8, 8]$, $[-2, 2]$ and $[-2, 2]$, correspondingly, and the step sizes were set to 0.02. The trial and error method gave a number of solutions with good margins to the trial ranges, and the solutions made reasonable predictions of the slope and the intercept. The best solution is chosen from those solutions according to the rule that the best solution gives the minimum root sum square (RSS) of the uncertain points numbers for all fluids.

Table 6.9 shows a comparison of the values of α, β, uncertain points and $\frac{\text{Uncertain}}{\text{Total}}$ from the least squares method and the calculation method using Eq. (6.10). "(S)" and "(C)" denote the least squares method and the calculation method, respectively. The values from the calculation gives less number of uncertain points but higher sum of square, and this also indicates that by the calculation way, the characterization is reasonable as

Table 6.9: Comparison of the values from the least squares method and the calculation method using Eq. (6.10) with model 2.

Fluid	α	β	Uncertain points	$\frac{\text{Uncertain}}{\text{Total}}$
Distilled water (S)	2668	-72	1	0.08%
Distilled water (C)	2681.6	-72.9	1	0.08%
Technical ethanol (S)	544	-71	21	1.95%
Technical ethanol (C)	536.9	-66.7	14	1.30%
n-pentane (S)	2594	-48	30	3.35%
n-pentane (C)	2701.1	-52.8	30	3.35%
Methanol (S)	1301	-47	25	3.11%
Methanol (C)	1345.4	-50.8	21	2.62%
1-propanol (S)	395	-80	71	5.53%
1-propanol (S)	395	-80	71	5.53%

the number of uncertain points is between the numbers by the least squares method and the least points method.

6.5 Comparison between the Two Coalescence-Jetting Threshold Models

6.5.1 The Applicability of the Models

By comparing between Table 6.3 and Table 6.7, it can be seen that the two models give comparably few numbers of uncertain points for different fluids. This indicates that the two models are similarly fit for characterizing the coalescence-jetting threshold within the range of diameter and velocity in the present work.

For the diameter and velocity range out of the present work (jetting with much larger droplet diameter and lower velocity), the comparisons of the models with the threshold data from the literature (Rodriguez & Mesler 1985) are made and discussed in Section 6.3.4 and Section 6.4.5, and it is shown that the exponential model (threshold model 1) fits better with the literature threshold data than the linear model (threshold model 2). This means that the exponential model may have a better potential to characterize the coalescence-jetting threshold with wider diameter and velocity ranges. Study of coalescence-jetting transition with larger droplet diameter (above 1 mm) with lower velocity is needed to further confirm the applicability of the exponential model and to propose a more suitable relation of Fr and Ca, for instance, exponential, polynomial etc. other than the linear model.

6.5.2 Possible Restrictions for the Threshold Models for Coalescence-Jetting and the Deductions

The characterization of the exponential model 1, Eq. (6.3) with the deduction term, Eq. (6.6), and the linear model 2, Eq. (6.7) with the deduction term, Eq. (6.10), are based on the experimental data which may be limited in the following aspects:

- Physical properties of fluids: the model and the deduction may be only applicable within certain property ranges which is covered by the experimental fluids.

    - Density range (kg/m^3): 600 - 1000.
    - Viscosity range ($mPa \cdot s$): 0.5 - 2.
    - Surface tension range (mN/m): 13 - 72.

Table 6.10: Diameter and velocity ranges of different fluids in coalescence-jetting threshold characterization.

Fluid	Diameter range (mm)	Velocity range (m/s)
Distilled water	0.06 - 0.7	0.1 - 12
Technical ethanol	0.07 - 0.7	0.1 - 10
n-pentane	0.1 - 0.6	0.3 - 6.5
Methanol	0.17 - 0.42	1.8 - 8
1-propanol	0.1 - 0.5	1.3 - 10

- Droplet size and velocity: Section 6.3.4 shows that the exponential model has the potential to be applied in a wider range (larger diameter and low velocity jetting) than the data ranges in the present work, while this is not completely confirmed by the fluids other than distilled water. The applicability of threshold model 2 is limited as the droplet size increases. The model applicability may be limited within the size and velocity ranges where both data from jetting and coalescence present, while the figures show that points out of the common ranges are also decently characterized. The general size and velocity range for different fluids are listed in Table 6.10. The table shows that even though the data ranges vary from case to case, the model is generally applicable in the micron-level diameter range from 0.1 mm to 0.7 mm.

6.6 Effects of Kinetic Parameters and Physical Properties on the Formation and Breaking of Crown

Different regimes or phenomena are favored by different processes. For instance, aerobic aqua-biological process likes the breaking of the crown because more splashed droplets into the air will enhance the oxygen transfer, while in LNG heat exchangers, more splashed droplets into the gas phase will lead to the reduction of heat transfer due to less liquid in contact with the tubes. The former sections propose quantitatively when the transition from coalescence to jetting occurs, and this section gives a qualitative analysis about the effects of different parameters on the crown formation and breaking.

The discussion of the effects from the physical properties are based on the observed differences with varying kinetic parameters.
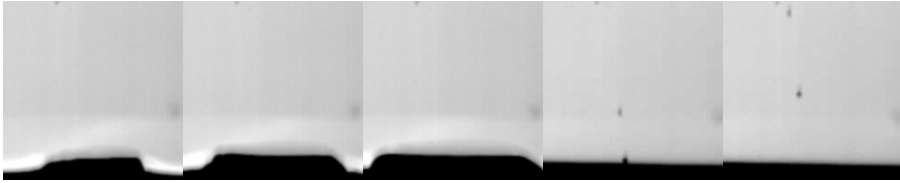
(a) Swell.wav.-1. (b) Swell.wav.-2. (c) Swell.wav.-3. (d) C.j. drop-1. (e) C.j. drop-2.

Figure 6.8: Swelling wave and secondary droplets from central jet of Methanol: $D = 0.25$ mm, $V = 4.0$ m/s.

(a) Crown-1. (b) Crown-2. (c) Crown-3. (d) Cen. jet-1. (e) Cen. jet-2.

Figure 6.9: Breaking of crown and central jet of Methanol: $D = 0.26$ mm, $V = 7.3$ m/s.

Effects of Kinetic Parameters

For a given fluid, for instance, methanol, when the kinetic parameters, diameter and velocity increase from a low level to a high level, observation differences can be found. Figure 6.8 shows the observations of methanol at a relatively low level of kinetic parameters compared to Figure 6.9 of methanol. The sequential images show that at this level only a swelling wave and secondary droplet from the central jet is formed, while crown formation and central jet is not observed. Figure 6.9 shows that as diameter and velocity increase to the high level, the crown is formed, and a instable pattern is formed at the rim of the crown. This instability finally leads to the breaking of the crown. An obvious central jet is also observed in Figure 6.9.

The observations agree with the coalescence-jetting characterizations that, for a given fluid, jetting occurs at higher inertial energy, i.e. higher level of diameter and velocity.

(a) Crown-1.   (b) Crown-2.   (c) Crown-3.   (d) C.j. drop.   (e) Cen. jet.
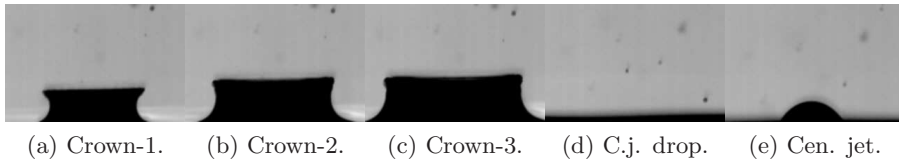
Figure 6.10: Non-broken crown and central jet of 1-propanol: $D = 0.28$ mm, $V = 8.8$ m/s.

Effects of Physical Properties

Figure 6.10 shows the observations of 1-propanol at even higher level of the kinetic parameters compared to Figure 6.9 of methanol. In the Figure of 1-propanol, the crown does not break, and the instability at the rim does not appear as the rim is very smooth. The central jet is lower than in Figure 6.9. The observation differences indicate that even though the kinetic parameters increase, instead of being more "turbulent", the impact of 1-propanol shows more stable characteristics. By comparing the physical properties between 1-propanol and methanol, it is found that their densities and surface tensions are nearly the same ($\rho \approx 800 \, \text{kg/m}^3$ and $\sigma \approx 22 \, \text{mN/m}$), while 1-propanol has much higher viscosity ($\mu = 1.968 \, \text{mPa} \cdot \text{s}$) than methanol ($\mu = 0.544 \, \text{mPa} \cdot \text{s}$). Thus, it can be concluded that higher viscosity reduces the perturbations needed for breaking a crown. The reason is that the viscosity dissipates the perturbations, and therefore a fluid with higher viscosity demands more kinetic energy to overcome the dissipation and leads to jetting.

In order to investigate the effect of the surface tension, Figure 6.11 of technical ethanol and Figure 6.12 of distilled water are compared. Figure 6.12 shows that the impact of a distilled water droplet with larger diameter and higher velocity (i.e. higher kinetic energy, because the density of distilled water is also higher than technical ethanol) does not form a crown but a swelling wave. Figure 6.11 shows that the impact of a technical ethanol droplet with lower kinetic energy forms a crown. As shown in Figure 6.11(a), the rim is not completely smooth, and it indicates that an instability forms at the rim. However, the instability is not strong enough to lead to breaking of the crown.

The effect from the density cannot be easily compared from the observation because:

- The density variations between the fluids are not as large as the variations in the viscosity and the surface tension.

- When the density variation is relatively obvious (distilled water and n-

pentane), their viscosities and surface tensions are not similar. Thus, the effects from density cannot be directly seen.

6.7 Bouncing-Coalescence Threshold Characterization Using the Weber number (We)

6.7.1 Hypothesis of the Components for Expressing the Threshold

It can be seen from the literature review in Chapter 2 that the transition between bouncing and coalescence depends on the inertial energy, which may be interpreted through the forms of the critical falling-height, the impact velocity, the kinetic energy and the Weber number. The viscosity and surface tension play roles in the transition. The Weber number is used to account for the effects from the surface tension. Compared to the surface tension, the viscosity effect is not investigated often, and only the gas viscosity is considered by Bach et al. (2004).

The assumption is that the transition between bouncing and coalescence is dependent on the competing effects of inertial and surface energy. Compared to the surface energy which tends to minimize the surface area of a system, the level of the inertial energy must be proper, which means high
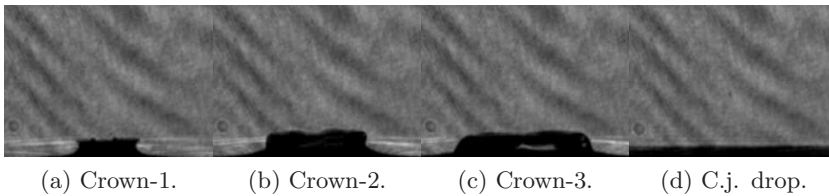

(a) Crown-1.   (b) Crown-2.   (c) Crown-3.   (d) C.j. drop.

Figure 6.11: Non-broken crown and secondary droplet from central jet of ethanol: $D = 0.17$ mm, $V = 8.9$ m/s.

(a) Swell.wav.-1.   (b) Swell.wav.-2.   (c) Swell.wav.-3.   (d) C.j. drop.
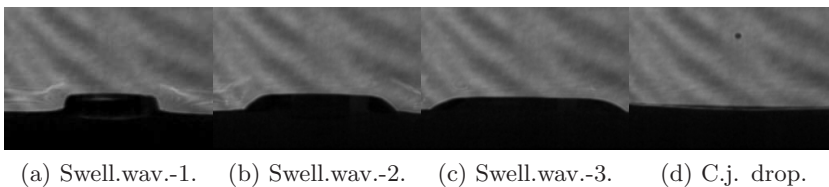
Figure 6.12: Swelling wave and secondary droplet from central jet of distilled water: $D = 0.21$ mm, $V = 8.9$ m/s.

enough or low enough, to break the drop-film interface. The Weber number, Eq. (2.3), which relates the inertial energy to the surface tension, can be used to find the proper limit for the transition. The Ohnesorge number, Eq. (2.2), which relates the viscosity to the surface tension, can be used to investigate the effect from the liquid viscosity.

6.7.2 Raw Data and the Models in the Literature

In the experiment, many coalescing droplets have high Weber number up to We $\approx$ 300, while the bouncing droplets have much lower Weber numbers. To show more specific information around the transition region, only a part of the data which is relatively close to the threshold is plotted in the following figures.

Figure 6.13(a), (b) and (c) show the plots of the Weber number versus the Ohnesorge number in coalescence and bouncing. Figure 6.13(a) also contains data points from partial coalescence. One B-C threshold model (Huang & Zhang 2008), Eq. (2.17), is plotted in the figures.

As can be seen from Figure 6.13(a) and Figure 6.13(b), for distilled water and technical ethanol, the data points of coalescence generally distribute on two sides of the data points of bouncing, and this agrees with Pan & Law (2007) that there are two transitions between coalescence and bouncing, which are from bouncing to coalescence (B-C) and from coalescence to bouncing (C-B) as the kinetic energy increases. For 1-propanol, only the B-C threshold was found in Figure 6.13(c).

The figures show that the B-C thresholds are not obviously dependent on the Ohnesorge number within the experimental data range. Thus, within the experimental data range, the B-C thresholds can be characterized using constant Weber numbers for the three fluids, and the threshold can be expressed as

$$\mathrm{We}_{\mathrm{critical}} = C_{\mathrm{bc}} \tag{6.11}$$

where C_{bc} is a constant denoting the critical Weber number where the transition happens.

For the C-B thresholds, there are two regions, for distilled water with Oh < 0.008 and the technical ethanol with Oh < 0.029, bouncing is the dominant regime, while there are quite a few coalescence data points. Out of this region, the dependency of the critical Weber number to the Ohnesorge number is not obvious. Thus, the C-B thresholds in this region can be written as follows.

$$\mathrm{We}_{\mathrm{critical}} = C_{\mathrm{cb}} \tag{6.12}$$

(a) Distilled water

(b) Technical ethanol

(c) 1-propanol

Figure 6.13: Raw data: the Weber number and the Ohnesorge number in coalescence and bouncing. (Continued)

6.7.3 Characterization of the B-C and C-B Thresholds Using the Critical Weber Number

The thresholds were characterized using the constant Weber numbers as shown by Eq. (6.11) and Eq. (6.12), and the two regression methods, the least points and the least squares, were used to determine the thresholds.

The B-C thresholds for distilled water, technical ethanol and 1-propanol are characterized within the ranges of We > 5, We > 9 and We > 11, respectively. The C-B thresholds for distilled water, technical ethanol are characterized within the ranges of We < 3 and Oh > 0.008 and We < 6 and Oh > 0.029, respectively. The step size for the trials of the critical Weber numbers is 0.001.

The critical Weber numbers for the the B-C and C-B thresholds are listed in Table 6.11. The number of uncertain points are also given in the table.

Figure 6.14(a), (b) and (c) show the plots of the Weber number versus the Ohnesorge number in coalescence and bouncing. Figure 6.14(a) also contains data points from partial coalescence. One B-C threshold model from literature (Huang & Zhang 2008), Eq. (2.17), is plotted in the figures.

The two methods give very close critical Weber numbers for a certain fluid. For choosing the critical Weber numbers, the deviations of the number of the uncertain points from the two methods are compared as described in Section 6.2. The chosen critical Weber number for the B-C and C-B thresholds are listed in Table 6.12.

6.7.4 Effects of the Physical Properties on the B-C Threshold

The following discussion is based on the characterized B-C thresholds.

- Viscosity: By comparing the thresholds shown in Table 6.12, it can

Table 6.11: The critical Weber numbers for the B-C and C-B thresholds.

Fluid	Regression	$We_{critical}$	Uncertain points	$\frac{Uncertain}{Total}$
B-C Threshold				
Distilled water	Point	6.656	7	0.624%
Distilled water	Square	6.329	25	2.23%
C-B Threshold				
Distilled water	Point	2.836	0	0%
Distilled water	Square	2.836	0	0%
B-C Threshold				
Technical ethanol	Point	12.858	14	1.28%
Technical ethanol	Square	12.409	24	2.19%
C-B Threshold				
Technical ethanol	Point	5.851	0	0%
Technical ethanol	Square	5.851	0	0%
B-C Threshold				
1-propanol	Point	13.777	1	0.10%
1-propanol	Square	14.035	2	0.20%

Table 6.12: Decided critical Weber number for the B-C and C-B thresholds.

Fluid	B-C Threshold ($We_{critical}$)	C-B Threshold ($We_{critical}$)
Distilled water	6.7	2.8
Technical ethanol	12.4	5.9
1-propanol	14.0	
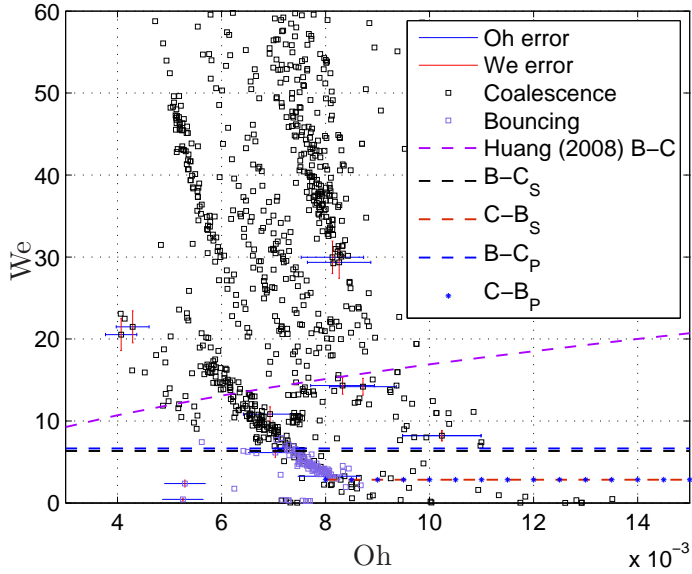
(a) Distilled water
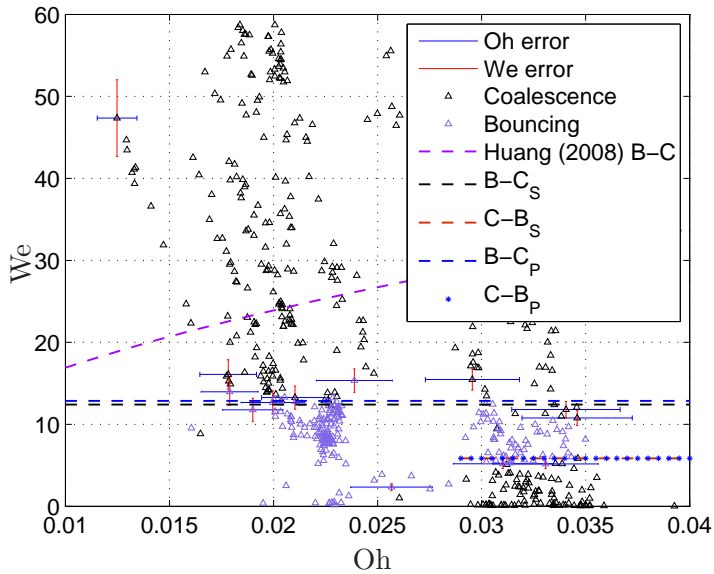
(b) Technical ethanol

Figure 6.14: Characterization of the B-C and C-B thresholds using the critical Weber number.
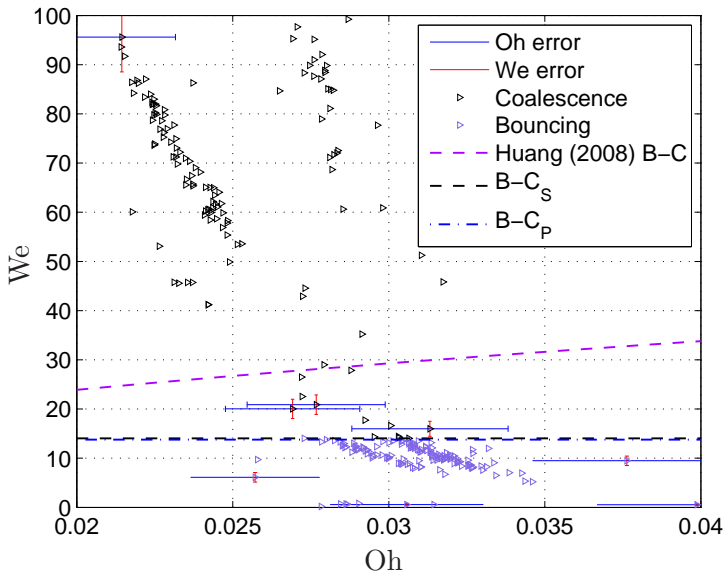
(c) 1-propanol

Figure 6.14: Characterization of the B-C and C-B thresholds using the critical Weber number. (Continued)

be found that technical ethanol and 1-propanol with nearly the same density ($\approx 800\,\text{kg/m}^3$) and surface tension ($22\,\text{mN/m}$) show different B-C thresholds, and the main reason for the threshold variation can be the viscosity difference between technical ethanol and 1-propanol. 1-propanol has a higher viscosity ($1.968\,\text{mPa} \cdot \text{s}$) than technical ethanol ($1.367\,\text{mPa} \cdot \text{s}$), and the higher viscosity leads to higher critical Weber number, which corresponds to more kinetic energy. Thus, it can be readily concluded that a fluid with higher viscosity demands more kinetic energy to reach the B-C threshold. The explanation can be that higher viscosity dissipates more kinetic energy, and therefore elevates the kinetic energy needed for coalescence.

- Density and surface tension: The effects of density and surface tension on the B-C threshold is difficult to predict as the lower B-C threshold of distilled water may be mainly due to the lower viscosity ($0.890\,\text{mPa} \cdot \text{s}$). However, the fact that distilled water with much higher surface tension still gives lower critical Weber number indicates that the viscosity is the dominant factor for the critical Weber number.

The B-C threshold was found for 3 fluids, while for the other two fluids, n-pentane and methanol, bouncing data was not obtained. If the viscosity is assumed to be the dominant factor, for the two fluids, n-pentane and methanol, with lower viscosities, bouncing should occur at lower level of the Weber number. According to the expression of the Weber number, Eq. (2.3), for low surface tension fluids such as methanol and n-pentane, reaching such a low level of Weber numbers requires low kinetic energy, i.e. small diameter and low velocity. Restrictions of the experimental setup may have limited the generation of droplets at this low level. Hence, this might be the reason that bouncing is not observed in experiment with n-pentane and methanol.

6.7.5 Possible Restrictions in the B-C and C-B Threshold Characterizations

The validation of the critical Weber numbers for the B-C threshold and C-B threshold may be restricted by the limited experimental data range. According to the experimental data range, the characterization of the B-C and C-B thresholds are possibly limited within the following range:

- Physical properties of fluids: the model and the deduction may be only applicable within certain property ranges which is covered by the experimental fluids.
  - Density range (kg/m^3): 800 - 1000.
  - Viscosity range ($mPa \cdot s$): 0.9 - 2.
  - Surface tension range (mN/m): 22 - 72.

- Droplet size is approximately from 0.1 to 0.3 mm.

6.7.6 The Restitution Coefficient for Bouncing Droplets

The restitution coefficient (ϵ), Eq. (2.10), was investigated versus the Weber number to show the variation with the impact parameters. The restitution coefficient for different fluids are plotted against the Weber number in Figure 6.15.

As can be seen from the figure, the restitution coefficient was relatively high when the impinging Weber number was low, and this means that the inertial energy is well preserved in the form of surface energy related to deformation during the impact. As the Weber number increases, the restitution coefficient drops rapidly to a certain stable level, at which, in general, the restitution coefficient varies within a narrow range.

The dramatical decrease in restitution coefficient is a non-ideal character in the bouncing phenomenon, and according to Richard & Quere (2000), the
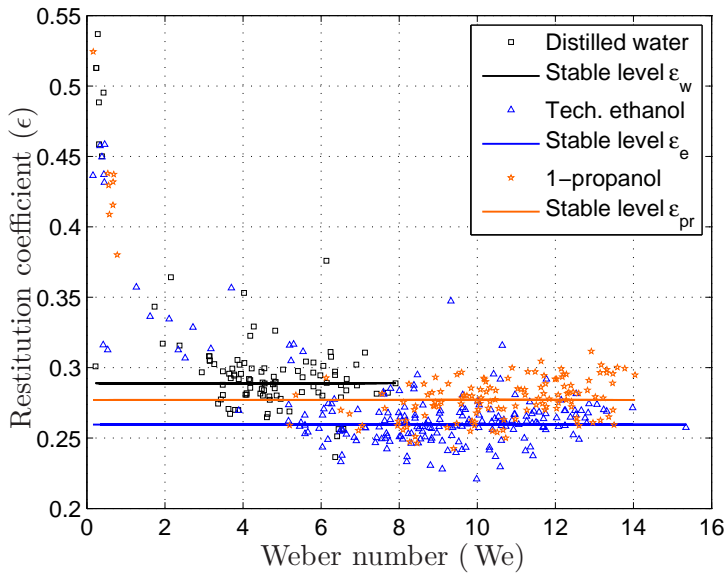
Figure 6.15: The restitution coefficients for the impact of a droplet with a deep liquid pool versus the Weber number.

Table 6.13: Stable level of the restitution coefficient.

Fluid	Stable restitution coefficient
Distilled water	0.29
Technical ethanol	0.26
1-propanol	0.28

dissipation processes are more obvious as the kinetic energy increases. At high Weber numbers, a larger portion of the kinetic energy is transformed into the energy forms related to surface waves and droplet oscillation, and finally dissipates (Bach et al. 2004).

The figure shows that the stable levels of the restitution coefficients are different for different fluids. It can be seen from Figure 6.15 that at the stable level, the variation of the restitution coefficient is within 0.05. So, it is defined that the stable level of the restitution coefficient is within the range of 0.025 below and above the median value of the restitution coefficients.

If the root mean square value of the restitution coefficient within this range is used to represent the level, the stable level of the restitution coefficient for each fluid is listed in Table 6.13.

The restitution coefficients are in the range between 0.2 and 0.3, and this agrees well with the range founded by Jayaratne & Mason (1964) and Bach et al. (2004). The assumption is that in the bouncing phenomenon, the energy loss to the wave formation and droplet oscillation may be quite similar for different cases, and thus the general stable level is in the range between 0.2 and 0.3. However, the variation between the stable level for different fluids indicate that the physical properties affect the energy loss, and the effects from the physical properties will be discussed in Section 6.7.7.

The figure also shows that different restitution coefficients can be found for the same Weber number, especially in the stable region. The reason can be that the droplets with the same Weber number can have different sizes and impinging velocities. The differences in size and velocity can lead to different portions of the loss in kinetic energy, and thus the restitution coefficients for the same Weber number can be different. Another possible explanation, could be variation of the impacting conditions in which a slight change of angle or small wave can affect the result.

6.7.7 Effects of the Physical Properties on the Stable Level of Restitution Coefficient

The general stable levels of restitution coefficients are quite similar between 0.2-0.3, while more specifically, they vary for different fluids. The following discussion on the effects from the physical properties are based on the stable level of restitution coefficients obtained in Table 6.13.

- Viscosity: The effect from viscosity can be readily seen by comparing the stable levels of the restitution coefficients of technical ethanol and 1-propanol as they have quite similar densities and surface tensions. 1-propanol with higher viscosity than technical ethanol gives higher restitution coefficient. Thus a fluid with higher viscosity tends to give a higher stable level of restitution coefficient. The explanation may be that a fluid with higher viscosity is not as "turbulent" as fluids with lower viscosities during the impacts, and thus it has less energy loss associated with wave formation and droplet oscillations. More kinetic energy is therefore preserved as deformation energy, which turns into the kinetic energy of bouncing droplets.

- Surface tension: Distilled water has lower viscosity than technical ethanol and 1-propanol, and if the effects of density and surface tension are not taken into account, a lower stable level of restitution coefficient for distilled water than the two alcohols can be expected.

However, distilled water gives higher stable level of restitution coefficient, and it indicates that the effects from density and surface tension are also significant. Compared with the surface tension, the density of distilled water is considered to be close and can be neglected, and thus the high surface tension of distilled water is the main reason for giving a higher restitution coefficient. So, a fluid with a higher surface tension tends to give a higher stable level of restitution coefficient. The explanation may be that a fluid with a high surface tension has better elasticity during the impacts, and it makes the reflection of droplets more efficient with less energy loss.

- Density: The effects from the density is difficult to predict as the densities of all the fluids are relatively close.

6.8 Summary of the Chapter

This chapter focuses on the analysis and discussion of the results:

- Two regression methods, the least squares and the least points, are introduced, and according to the later characterizations, both methods give very satisfactory results for identifying the threshold between regimes.

- The threshold between coalescence and jetting are analyzed for five fluids, and two models, the exponential model 1, Eq. (6.3), using We and Oh and the linear model 2, Eq. (6.7), using Fr and Ca are proposed. Both models can well characterize the threshold of coalescence-jetting with few uncertain points. In the exponential model, the reference diameter, γ, is the only variable which needs to be determined, and in the linear model, two variables, α and β, must be characterized. The variables in both models are determined by using regression methods for the five experimental fluids. Both models can well characterize the coalescence-jetting threshold within the diameter and velocity ranges in the present work, while the comparisons between the models and a few literature threshold data show that the exponential model may have a better potential for characterizing the diameter and velocity ranges of literature data. Further experiments focusing on jetting with larger droplet diameter and low velocity are needed to confirm the exponential model and to propose a better model using Fr and Ca.

- Application of the models can be extended to characterize the thresholds of coalescence-jetting for other uncharacterized fluids by using

Eq. (6.6) and Eq. (6.10) for calculating the model constants in the two models. Compared to the model constants from the experimental data fitting, the constants by the calculation methods give very good characterizations which give less uncertain points than the least squares methods.

- Based on the observed behavior, the effects of physical properties on crown formation and breaking is discussed, and in summary, higher viscosity and higher surface tension tend to reduce the perturbations for crown formation and breaking.

- The threshold between coalescence and bouncing is analyzed, and the critical Weber numbers for the B-C thresholds of three fluids, distilled water, technical ethanol and 1-propanol, are characterized with few uncertain points. The C-B thresholds are found for distilled water with Oh > 0.008 and for technical ethanol with Oh > 0.029, while below these Ohnesorge numbers bouncing is the dominant regime.

- Based on the B-C thresholds, the effects from the physical properties are discussed. In summary, higher viscosity tends to give higher critical Weber number for the B-C threshold.

- The restitution coefficients for three fluids are analyzed. The general stable levels of the restitution coefficient agree well with literature, and the effects of the physical properties on the specific levels are discussed. In summary, higher viscosity and higher surface tension tend to preserve more kinetic energy during the impacts, and give a higher level of restitution coefficient.

Chapter 7

Conclusions and Recommendations

7.1 Conclusions

The present investigations on droplets impinging vertically on a deep liquid pool comprised five fluids. Three main different phenomena, jetting, coalescence and bouncing were studied.These are the main conclusions:

- The experimental method used in the present work has several characteristics:
  - The test cell is designed and constructed in a proper way for carrying out the drop-pool impacts, and it is flexible for modifications.
  - The impact phenomena were generated with a better isolation to the neighboring impacts than the methods in the literature.
  - The generated droplets had relatively wide ranges of diameter in the micron-level from $0.1\,\mathrm{mm}$–$0.7\,\mathrm{mm}$ and velocity from $0.1\,\mathrm{m/s}$–$10\,\mathrm{m/s}$.
  - The collimated white light LED can give better image quality with more uniform background than the He-Ne laser. The homogeneous background is critical for reducing the uncertainties during the image-processing.
  - The image-processing routines have been made. The routines are efficient and accurate compared to the default manual measurements using the camera software.
  - Many safety measures were carried out for securing the experimental environment.

- The uncertainty analysis showed that the relative uncertainty for diameter and velocity measurements are generally below 5%, and the relative uncertainties for the dimensionless numbers (Re, Oh, We, Fr and Ca) are generally below 10%. However, through the analysis, it is

concluded that the uncertainties can be further reduced with the conditions of more suitable standard measurement (gauge), more suitable light source, better focus, more stable temperature conditions, fluids with more confirmed properties and less deformed droplets. The comparison of the uncertainties of dimensionless parameters shows that compared to other dimensionless parameters, the Froude number has a lower uncertainty which is an advantage in the threshold characterization.

- The understanding of the phenomena has been improved through the observations compared to the initial stage of the project:

  - Jetting: Four observations are described. For a given fluid, as the kinetic energy of an impinging droplet increases, the impact wave changes from a swelling wave to an unbroken crown and finally to a broken crown with splashed droplets from the rim of the crown, and the central jet changes from non-obvious (small or unseen) to obvious.

  - Coalescence: Two observations are described. The low-energy collision coalescence causes a subtle surface wave, while the high-energy collision causes a clear and strong surface wave.

  - Bouncing: It occurs when the kinetic energy of an impact droplet is between the kinetic energy levels of two types of coalescence. The observations show that the droplets do not merge into the pool but bounce off with a reduced velocity compared to the impinging velocity.

- The coalescence-jetting thresholds for the five experimental fluids were well characterized by an exponential model and a linear model within the diameter and velocity ranges in the present work. The formulation of the two models are as follows.

  - The characterizations using the Weber number and the Ohnesorge number show that the widely-used form of the model, Eq. (6.1), with constant exponents on the Ohnesorge number cannot fit the sharp threshold variations for fluids with relatively high viscosities such as distilled water, technical ethanol and 1-propanol, and thus the exponential model, Eq. (6.3), with a correction term is proposed.

  - The linear model, Eq. (6.7), using the Froude number and the capillary number is also proposed.

The advantages and limitations of the two models are:

- Advantages: Regarding the research focus, the micron-level droplet impacts, both models give very good characterizations with few uncertain points within the diameter and velocity ranges of the present study.
- Limitations: The comparisons between the models and the literature threshold data (Rodriguez & Mesler 1985) show that the exponential model exhibits better fits for millimetric-level droplet impacts than the linear model.

Thus, it can be concluded that the two models are similarly competence for the micron-level droplet impacts, and the exponential model is recommended for characterizing the coalescence-jetting of millimetric-level droplet impacts.

For predicting the thresholds for a given fluid, generalized calculation methods, Eq. (6.6) and Eq. (6.10), for the parameters in both models are suggested. The characterizations using calculation methods are quite comparable with the curve-fitted characterizations, however, the calculation methods need to be further validated by more fluids.

- There are two thresholds between bouncing and coalescence, B-C and C-B thresholds. The B-C threshold can be characterized by using critical Weber numbers. The C-B threshold is found with the Ohnesorge number above a certain level, and it can also be characterized using the critical Weber number.

- The restitution coefficient for three fluids, distilled water, technical ethanol and 1-propanol is investigated. The stable level of the restitution coefficient is between 0.2-0.3 which agrees well with the literature.

- The characterizations and analysis may be limited within the property ranges: density ($\mathrm{kg/m^3}$) 600-1000, viscosity ($\mathrm{mPa \cdot s}$) 0.5-2, surface tension ($\mathrm{mN/m}$) 13-72, and the kinetic parameter ranges: diameter (mm) 0.1-0.7 and velocity ($\mathrm{m/s}$) 0.1-10.

- The effects of the physical properties on the crown formation and breaking, the B-C threshold and the restitution coefficient are discussed.

  - Viscosity: High viscosity reduces the perturbations for the crown formation and breaking, giving higher critical Weber number for B-C threshold and higher restitution coefficient. The explanation is that the viscosity dissipates the turbulence in the flow.

 – Surface tension: High surface tension inhibits the formation of the crown due to the area-minimizing drag force, and gives higher restitution coefficient due to better elasticity.
 – Density: The effect from density is more difficult to predict due to the relatively close densities for the experimental fluids.

7.2 Recommendations

Based on the conclusions, the following recommendations is given.

• The exponential model using We and Oh is promising for both micron-level and millimetric-level droplet impacts, however, it needs to be confirmed further using fluids other than distilled water. The linear model using Fr and Ca needs to be improved to fit wider ranges of diameter and velocity. Thus, the further research should supply information of coalescence-jetting transition with larger droplet diameter (millimetric level) and low velocity than that in the present study. For generating droplets with larger diameter and low velocity, a dropper method, which generates/detaches droplets from a nozzle tip by utilizing the gravity is recommended. Small-sizes hypodermic needles or tiny manufactured glass tubes combining with a precise syringe pump can be applied.

• Investigations can be further carried out to characterize the 4 types of observations in jetting. The evolution processes such as the formation of crown and central jet, the breaking of crown and central jet can be studied to have more understanding of the conditions at which droplets will be entrained in the gas flow as this is important for gas-liquid separation equipment.

• Even more fluids are suggested to be used in the future experiment to validate and correct the calculation methods for the parameters in the two coalescence-jetting models, and this is also required for determining a model for the thresholds between bouncing and coalescence. When choosing the fluids, it is ideal to fix two physical properties of two fluids and vary another, because it is easier to investigate effects from the varying property. As the effects of the viscosity are more clearly seen from the present study, it would be preferable to solely vary either the density or the surface tension in a later study. The sole variation of density or surface tension can possibly be reached by using chemical mixtures.

- With the consideration for simulating the LNG heat exchanger environment better, vertical impact on a stagnation pool is a very idealized situation. Further studies require more complex impact situations such as impacts with a thin film covered surface which can have different roughnesses and impacts with a flowing liquid film with tilted angles.

- It would be very helpful to couple the experiments with the numerical modeling to further improve the understanding in this field.

Bibliography

Abramoff, M. D., Magelhaes, P. J. & Ram, S. J. (2004), 'Image processing with imagej', *Biophotonics international* **11**(7), 36–42.

Al-Azzawi, A. (2006), *Light and optics*, CRC Press.

Austrheim, T. (2006), Experimental characterization of high-Pressure natural Gas scrubbers, PhD thesis, University of Bergen.

Aziz, S. D. & Chandra, S. (2000), 'Impact, recoil and splashing of molten metal droplets', *International journal of heat and mass transfer* **43**(16), 2841–2857.

Bach, G. A., Koch, D. L. & Gopinath, A. (2004), 'Coalescence and bouncing of small aerosol droplets', *Journal of fluid mechanics* **518**, 157–185.

Bartolo, D., Bouamrirene, F., E. Verneuil, A. B., Silberzan, P. & Moulinet, S. (2006), 'Bouncing or sticky droplet: impalement transitions on superhydrophobic micropatterned surface', *Europhysics letters* **74**(2), 299–305.

Bennenson, W., Harris, J. W., Stocker, H. & Lutz, H. (2006), *Handbook of physics*, Springer-Verlag New York, LLC.

Buckingham, E. (1914), 'On physically similar systems; illustrations of the use of dimensional equations', *Physics review* **4**, 345–376.

Cai, Y. K. (1989), 'Phenomena of a liquid drop falling to a liquid surface', *Experiments in fluids* **7**, 388–394.

Carey, B. S., Scriven, L. E. & Davis, H. T. (1980), 'Semiempirical theory of surface tension of binary systems', *AIChE journal* **26**(5), 705–711.

Cossali, G. E., Brunello, G., Coghe, A. & Marengo, M. (1999), 'Impact of a single drop on a liquid film: experimental analysis and comparison with empirical models', *Italian congress of thermofluid dynamics UIT* **40**, 53–59.

Cossali, G. E., Coghe, A. & Marengo, M. (1997), 'The impact of a single drop on a wetted solid surface', *Experiments in fluids* **22**, 463–472.

Dorao, C. A., Fernandino, M., Patruno, L. E., Dupuy, P. M., Jakobsen, H. A. & Svendsen, H. F. (2009), 'Macroscopic description of droplet-film interaction for gas-liquid systems', *Applied mathematical modelling* **33**(8), 3309–3318.

Edmund Optics™ Ltd. (2009), 'Infinity k2/sc long distance video microscope', `http://www.edmundoptics.com/onlinecatalog/displayproduct.cfm?productID=1477`.

Engel, O. G. (1967), 'Initial pressure, initial flow velocity, and the time dependence of crater depth in fluid impacts', *Journal of applied physics* **38**(10), 3935–3940.

Fröba, A. P., Pellegrino, L. & Leipertz, A. (2004), 'Viscosity and surface tension of saturated n-pentane', *International journal of thermodynamics* **25**(5), 1323–1337.

García-Tabarés, L., Abramian, P., Calero, J., Toral, F., Ijspeert, A. & Pérez, J. C. (2002), Dimensional metrology of cylinders based on digital image processing: application to lhc corrector magnets, *in* 'Proceedings of EPAC', Paris, France, pp. 2394–2396.

Hetland, J. & Gochitashvili, T. (2004), *Security of natural gas supply through transit countries*, Springer Netherlands.

Hobbs, P. V. & Osheroff, T. (1967), 'Splashing of drops on shallow liquids', *Science* **158**(3805), 1184–1186.

Hsiao, M. Y., Litcher, S. & Quintero, L. G. (1988), 'The critical weber number for vortex and jet formation for drops impact on a liquid pool', *Physics of fluids* **31**(12), 3560–3562.

Huang, Q. Y. & Zhang, H. (2008), 'A study of different fluid droplets impacting on a liquid film', *Petroleum science* **5**, 62–66.

Jayaratne, O. W. & Mason, B. J. (1964), 'Coalescence and bouncing of water drops at an air/water interface', *Proceedings of the royal society of London* **280**(1383), 545–565.

Johnsen, C. G. (2007), Experiemental and numerical investigation of droplet phenomena, PhD thesis, Norwegian Univesity of Science and Technology.

Johnson, R. W. (1998), *The handbook of fluid dynamics*, Springer.

Lex, T., Ohlig, K., Fredheim, A. O. & Jenssen, C. B. (2007), Ready for floating lng - qualification of spiral wound heat exchangers, *in* 'Proceedings 15th International Conferences on Liquefied Natural Gas', Barcelona, Spain, pp. PO–27.1–PO–27.14.

Lide, D. R. (2009), *CRC Handbook of Chemistry and Physics*, 89th edn, CRC Press/Taylor and Francis, Boca Raton, FL.

Lord Rayleigh, F. R. S. (1878), 'On the instability of jets', *Proceedings of the London mathematical society* **10**, 4–13.

Lord Rayleigh, F. R. S. (1879), 'On the capillary of jets', *Proceedings of the royal society of London* **29**, 71–97.

Macklin, W. C. & Metaxas, G. J. (1976), 'Splashing of drops on liquid layers', *Journal of applied physics* **47**(9), 3963–3970.

Manzello, S. L. & Yang, J. C. (2002), 'An experimental study of a water droplet impinging on a liquid surface', *Experiments in fluids* **32**, 580–589.

Mundo, C., Sommerfeld, M. & Tropea, C. (1995), 'Droplet-wall collisions: experimental studies of the deformation and breakup process', *International journal of multiphase flow* **21**(2), 151–173.

Pan, K. L. & Law, C. K. (2007), 'Dynamics of droplet-film collision', *Journal of fluid mechanics* **587**.

Pasandideh-Fard, M., Aziz, S. D., Chandra, S. & Mostaghimi, J. (2001), 'Cooling effectiveness of a water drop impinging on a hot surface', *International journal of heat and fluid flow* **22**(2), 201–210.

Rein, M. (1993), 'Phenomena of liquid drop impact on solid and liquid surface', *Fluid dynamic research* **12**, 61–93.

Richard, D. & Quere, D. (2000), 'Bouncing water drops', *Europhysics letters* **50**(6), 769–775.

Rioboo, R., Bauthier, C., Conti, J., Voue, M. & Coninck, J. D. (2003), 'Experimental investigation of splash and crown formation during single drop impact on wetted surfaces', *Experiments in fluids* **35**(2003), 648–652.

Rodriguez, F. & Mesler, R. (1985), 'Some drops don't splash', *Journal of colloid and interface science* **106**(2), 347–352.

Schotland, R. M. (1960), 'Experimental results relating to the coalescence of water drops with water surfaces', *Discussion of the Faraday society* **30**, 72–77.

Sevault, A. (2008), Experimental investigation of droplets impacting onto a liquid surface, Master's thesis, ENSMA/SINTEF Energy Research.

Shin, J. & McMahon, T. A. (1990), 'The turning of a splash', *Physics of fluids* **2**(8), 1312–1317.

Shukla, D., singh, S., Parveen, S., Gupta, M. & Shukla, J. P. (2008), 'Thermophysical properties of binary mixtures of methanol with chlorobenzene and bromobenzene from 293k to 313k', *International journal of thermophysics* **29**, 1376–1384.

Sivakumar, D. & Tropea, C. (2002), 'Splashing impact of a spray onto a liquid film', *Physics of fluids* **14**(12), 85–88.

Stow, C. D. & Hadfield, M. G. (1981), 'An experimental investigation of fluid flow resulting from the impact of a water drop with and unyielding dry surface', *Proceedings of the royal society of London* **A**(373), 419–441.

Tanaka, Y., Matsuda, Y., Fujiwara, H., Kubota, H. & Makita, T. (1987), 'Viscosity of (alcohol + water) mixtures under high pressure', *International journal of thermophysics* **8**(2), 147–163.

Thomson, J. J. & Newall, H. F. (1885), 'On the formation of vortex rings by drops falling into liquids', *Proceedings of the royal society of London* **39**.

Thoroddsen, S. T. (2000), 'The coalescence cascade of a drop', *Physics of fluids* **12**(6), 1265–1267.

Vander Wal, R. L., Gordon, W., Berger, M. & Mozes, S. D. (2006*a*), 'Droplet splashing upon films of the same fluid of various depth', *Experiments in fluids* **40**, 33–52.

Vander Wal, R. L., Gordon, W., Berger, M. & Mozes, S. D. (2006*b*), 'The splash/non-splash boundary upon a dry surface and thin liquid film', *Experiments in fluids* **40**, 53–59.

Vaquez, G., Alvarez, E. & Navaza, J. M. (1995), 'Surface tension of alcohol + water from 20 to 50°c', *Journal of chemical and engineering data* **40**, 611–614.

Wang, A. B. & Chen, C. C. (2000), 'Splashing impact of a single drop onto very thin liquid films', *Physics of fluids* **12**, 2155–2158.

Wheeler, A. J. & Ganji, A. R. (2004), *Introduction to engineering experimentation*, second edn, Pearson Education, Inc.

Worthington, A. M. (1876), 'On the forms assumed by drops of liquids falling vertically on a horizontal plate', *Proceedings of the royal society of London* **25**.

Yarin, A. L. & Weiss, D. A. (1995), 'Impact of drops on solid surfaces: self-similar cappillary waves, and splashing as a new type of kinematic discontinuity', *Journal of fluid mechanics* **283**, 141–173.

Yung, D., Lorenz, J. J. & Ganic, E. N. (1980), 'Vapor/liquid interaction and entrainment in falling film evaporators', *Journal of heat transfer* **102**.

Zhbankova, S. L. & Kolpakov, A. V. (1990), 'Collision of water drops with a plane water surface', *Fluid dynamics* **25**(3), 470–473.